

Measuring interactions in fluids with small-cantilever AFM

Measuring interactions in fluids with small-cantilever AFM

Proefschrift

Ter verkrijging van
de graad van Doctor aan de Universiteit Leiden,
op gezag van de Rector Magnificus prof. mr. P.F. van der Heijden,
volgens besluit van het College voor Promoties
te verdedigen op dinsdag 11 december 2007
klokke 16.00 uur

door
Allard Jules Katan
geboren the Rhenen
in 1977

Promotiecommissie

- Promotor: Prof. dr. J.W.M. Frenken
- Co-promotor: Dr. ir. T.H. Oosterkamp
- Referent: Prof. dr. S.P. Jarvis,
University College Dublin, Ierland
- Overige leden: Dr. P.D. Ashby,
Lawrence Berkeley National Laboratory, Berkeley, Verenigde
Staten
- Prof. Dr. F. Mugele,
Universiteit Twente, Enschede
- Prof. dr. P.G. Bolhuis,
Universiteit van Amsterdam, Amsterdam
- Dr. S.J.T. van Noort
- Prof. Dr J.M. van Ruitenbeek

ISBN/EAN 978-90-9022574-6

an electronic version of this thesis can be found at <https://openaccess.leidenuniv.nl>

The work described in this thesis was performed at the Kamerlingh Onnes Laboratory, Universiteit Leiden, Niels Bohrweg 2, 2333 CA, Leiden. This work is part of the research program of the 'Stichting voor Fundamenteel Onderzoek der Materie (FOM)', which is financially supported by 'Nederlandse Organisatie voor Wetenschappelijk onderzoek (NWO)'.

Voor Corien

Contents

1	Introduction and outline	1
1.1	Hydrophobic forces	1
1.2	Atomic Force Microscopy	3
1.3	Outline of this thesis	5
2	General considerations about noise and bandwidth in Atomic Force Microscopy and Spectroscopy	7
2.1	Introduction	7
2.2	Thermal limits in cantilever-based technologies	7
2.3	Choosing the right cantilever to optimize signal-to-noise ratio	13
3	Design and performance evaluation of a versatile miniature cantilever optical deflection detection system	19
3.1	Cantilever fabrication	19
3.2	Optical detection system	25
4	Design and performance evaluation of a miniature cantilever AFM scanner	37
4.1	Scanner and coarse approach	37
4.2	Control and feedback electronics	40
4.3	Scanner characterization	45
5	Force versus distance measurements in dynamic AFM: the case of non-constant amplitude	51
5.1	Introduction	51
5.2	The harmonic oscillator as a model for an AFM cantilever	51
5.3	Force inversion	55
5.4	A new force inversion method for AM-AFM	59
6	Exploring the limits of amplitude modulation force spectroscopy with numerical experiments	65
6.1	Phase offsets and finite measurement range	65
6.2	Limits of the harmonic approximation	66
6.3	Noise effects	76
6.4	Conclusions	81

7 Measuring hydrophobic interactions with three-dimensional nanometer resolution	83
7.2 Introduction	83
7.3 Experimental methods	86
7.4 Results	89
7.5 Discussion	99
7.6 Conclusion	101
References	103
Samenvatting voor de leek	115
List of publications	119
Curriculum vitae	121
Acknowledgements	123

List of figures

Figure 1.1	Generic schematic of an Atomic Force Microscope	2
Figure 2.1	Calculated thermal motion amplitudes for several cantilevers	11
Figure 2.2	Force noise versus position noise in water at room temperature for several cantilevers	11
Figure 2.3	Hydrodynamic resistance as a function of frequency for cantilevers of different width in air and in water	12
Figure 2.4	Effect of cantilever stiffness on image quality and applied force for soft and hard samples	14
Figure 3.1	Illustration of corner clearance	20
Figure 3.2	Deformation of cantilever remains during coarse milling	21
Figure 3.3	Steps in the FIB cantilever production process and finished product	22
Figure 3.4	Steps in the lithographic cantilever production process and finished cantilevers	23
Figure 3.5	Optical path in a single lens optical beam deflection system	26
Figure 3.6	Photodiode amplifier with noise sources	29
Figure 3.7	Signal and signal-to-shot-noise ratio as a function of incoming beam width (relative to lens radius) for different eccentricity	30
Figure 3.8	Optical beam deflection detection setup	33
Figure 3.9	Experimentally measured thermal spectra of several miniature cantilevers	35
Figure 4.1	Scanner and coarse approach design	38
Figure 4.2	Tip holder	39
Figure 4.3	Schematic representation and time diagram of the peak detection amplitude converter	41
Figure 4.4	Schematic and time diagram of 3D feedback	42
Figure 4.5	Scanner resonances measured optically and electrically	46
Figure 4.6	High speed scanning in air on a DNA sample	47
Figure 4.7	High speed scan with 1.2 mm/s vertical tip speed	48
Figure 4.8	Molecular resolution scan in liquid, contact mode	49
Figure 5.1	Response curves in FM-AFM	54
Figure 5.2	Response curves in AM-AFM	55
Figure 5.3	Effective frequency shifts and amplitude variations in AM-AFM	61
Figure 5.4	Reconstructed force profiles for a high quality factor	64
Figure 5.5	Reconstructed damping for a high quality factor	64
Figure 5.6	Reconstructed force for a low quality factor	64

Figure 5.7	Reconstructed damping for a low quality factor	64
Figure 6.1	Amplitude versus chip position in a simulated DFS experiment	71
Figure 6.2	Force as a function of closest approach distance on a stiff sample	71
Figure 6.3	Amplitude as a function of closest approach distance on a stiff sample	71
Figure 6.5	Amplitude as a function of closest approach distance as measured from time traces	72
Figure 6.6	Force as a function of the true closest approach distance	73
Figure 6.4	Simulated time traces of cantilevers	73
Figure 6.7	Effect of damping gradient on amplitude/phase versus distance profiles	74
Figure 6.8	Effect of damping gradient on reconstructed force and damping profiles	75
Figure 6.9	Time trace of a cantilever moving in a potential with a large damping gradient	76
Figure 6.10	Simulated experimental results including thermal noise compared to noiseless simulations	78
Figure 6.11	Force noise amplification plotted versus amplitude	79
Figure 6.12	Effect of noise on calculated damping profiles	80
Figure 6.13	Noise scaling in the damping coefficient	81
Figure 7.1	Schematic side view of the sample	85
Figure 7.2	Nanotube tip used in the measurement	86
Figure 7.3	Nanobubbles on a mixed SAM with large domains	89
Figure 7.4	Topography of a SAM sample with small domains in air and water	90
Figure 7.5	Single measurement of amplitude and phase with calculated force and dissipation	91
Figure 7.6	Topograph reconstructed from amplitude-distance measurements	93
Figure 7.7	Averaged forces and damping coefficients	94
Figure 7.8	Forces in the context of the tip-sample distance	96
Figure 7.9	Cross section of the topography related to tip radius	97
Figure 7.10	Exponential fit to the force measured on a hydrophobic domain	98

1 Introduction and outline

1.1 Hydrophobic forces

In many processes in nature and technology, hydration forces are believed to play an important role [1]. Examples include self-assembly of micelles, vesicles, and membranes [2], folding of proteins [3], properties of zeolites and clays, stabilization of colloidal solutions, lubrication, and microfluidic transport. Hydration forces are the forces between particles or surfaces in aqueous solution that exist because of their specific interaction with the water molecules. Generally, hydration forces are separated in two classes: repulsive hydrophilic or structural forces, and attractive hydrophobic forces.

The currently most widely accepted theory of the hydrophobic effect is the Lum-Chandler-Weeks theory [4]. In this theory, there are two causes for the hydrophobic effect: reorganization of the hydrogen bond network of water surrounding a hydrophobic entity, and breaking of hydrogen bonds. The two constituents of the hydrophobic force play a role at different length scales. Around hydrophobic entities close to the size of a water molecule - such as small alkanes - water can reform its hydrogen bond network without breaking any bonds. This leads to a decrease in entropy, and thus an increase in the free energy of the system. When the hydrophobic entity is large, it becomes geometrically impossible to reshape the bond network, and hydrogen bonds must be broken. This increase in enthalpy also increases the free energy. The critical radius, beyond which the enthalpic contribution outweighs the entropic one is around 1 nm, depending on the temperature. In this picture, the hydrophobic force emerges from the fact that the extra free energy per unit volume of hydrophobic entity decreases with the total volume as soon as its size is larger than the critical radius. In other words: hydrophobic entities larger than 1 nm will tend to minimize the surface area in contact with water by clustering together. Confirmation of this theory is found in the solvation behavior of small alkanes. However, to our knowledge accurate predictions for the dependence of the hydrophobic force on separation between hydrophobic surfaces are not available.

In the past three decades, numerous experiments have been conducted to determine the distance dependence of hydration forces by direct force measurements with the Surface Forces Apparatus (SFA) or Atomic Force Microscope (AFM). The hydrophilic repulsive force is generally considered to be short, decaying exponentially with typical lengths of 0.2-1.4 nm [1,5,6]. In contrast, the

experimental body of work on the range of the hydrophobic force does not converge so easily, and numbers ranging from a few nm to hundreds of nm have been proposed [7-9]. Recent overviews by Christenson [10] and Meyer [11] summarize direct measurements of the hydrophobic force and some of the artifacts that have led to the overestimation of its range. Even when these artifacts are circumvented, the hydrophobic force is still proposed to be the dominant interaction between hydrophobic surfaces up to distances of 10 nm.

Many surfaces where the hydrophobic force plays a key role, in particular proteins and biological membranes, are heterogeneous on length scales between 1 and 10 nm, having both hydrophilic and hydrophobic units. Although some theory has been developed to understand the solvation of amphiphiles [12], a theory that can deal with the complexity of proteins and membranes still appears to be far away.

Surprisingly, the influence of heterogeneity on hydration forces has not been investigated experimentally. Although the microscopic theory of the hydrophobic effect has made significant advances in recent years [13], to our knowledge only one - very recent - numerical investigation of hydration forces between nanoscale patterned surfaces is reported in the literature [14].

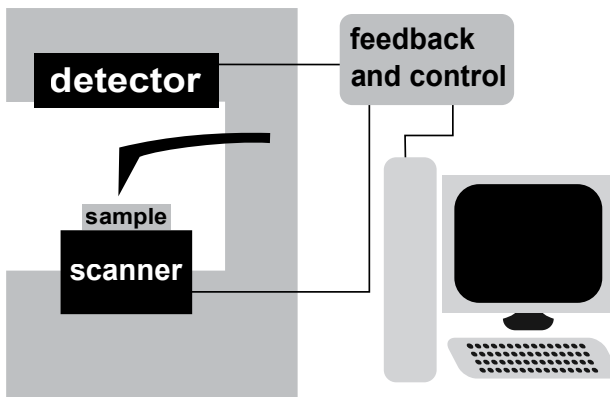


Figure 1.1 Generic schematic of an Atomic Force Microscope

A sharp tip is mounted on a cantilever beam or other flexible spring. The force acting on the tip is measured by detecting the deflection of the spring from its equilibrium position. The tip is scanned over the sample (or vice versa), and by doing feedback on the vertical position of the sample to keep the force constant, a topographic image can be formed. The apparatus cannot only be used for imaging, but the dependence of the force on separation can be measured as well. This is done by switching the feedback off and approaching and retracting the tip, while measuring the deflection.

1.2 Atomic Force Microscopy

The Atomic Force Microscope was invented by Binnig, Quate and Gerber in 1986 [15], when they combined features of the stylus profilometer and the scanning tunneling microscope (STM). The basic components and working principle are explained in figure 1.1. The name is somewhat confusing, since the instrument is used in many applications that do not involve interactions between single atoms, or applications that do not involve imaging. Although the more consistent name *Scanning* Force Microscope is used as well, AFM has become the household name of the instrument.

The sharp tip and high force sensitivity of the AFM allow the measurement of small forces with sub-nanometer resolution. Since forces are present in almost any system, the use of AFM has spread from its original application of high resolution surface imaging in solid state physics [16] to areas as diverse as cell biology [17], nutrition [18] and andrology [19]. A search on the ISI web of knowledge for articles with 'force microscopy' as the topic gives over 41000 results as of October 2007. The commercial availability of AFM systems has certainly aided the spread of the technique beyond the realm of physics laboratories. Another important reason AFM is so popular is the fact that it can easily be used in a great variety of environments, from ultrahigh vacuum to physiological buffer solutions, with minimal demands on the sample preparation.

1.2.1 Force measurements

The measurement of force versus displacement curves (often referred to as force-distance curves or force curves) has evolved from being a method used solely for the purpose of finding optimal parameters for imaging to an independent field of research. A very complete overview of this field is found in the review by Butt *et al* [5]. The possibility of measuring single molecule unbinding or unfolding events [20,21] has made AFM a new tool in the characterization of biochemical interactions. It has become possible to probe the energy landscape of protein-protein interactions by studying the dependence of unbinding force on loading rate [22]. This technique is usually called dynamic force spectroscopy, a name that is also used for a very different technique: the measurement of interactions by monitoring amplitude, phase or frequency shift of an oscillation applied to the cantilever. In this thesis the name "Dynamic Force Spectroscopy" or DFS will be used for the latter. The measurement of unbinding forces as a function of loading rate shall be referred to as "Kinetic Force Microscopy".

Two other techniques exist for directly measuring forces on the molecular scale: the Surface Forces Apparatus (SFA) [23] and optical tweezers [24,25]. These techniques have some complementary properties to AFM. Though not a single-molecule technique, the SFA can measure absolute distances between interacting molecular layers with sub-nanometer resolution. This

is not possible with AFM, where tip-sample separation must always be inferred from the force profile. The samples in the SFA are mounted on two crossed cylinders with a radius of a few centimeters. Due to its averaging over many molecular interactions, the SFA can measure much lower forces (normalized by the radius of curvature of the interacting surfaces) than AFM. An intermediate technique is colloidal probe AFM [26], where the sharp AFM tip is replaced by a μm -sized colloid. Optical tweezers can measure forces far below 1 pN due to the use of very soft springs and small colloids as the force transducer. Furthermore, they are not limited to interfaces, and can be used to measure forces *inside* cells and between molecules in bulk liquid.

The main advantage of AFM over both these techniques is the ability to acquire both high resolution topographic and force information in the course of a single measurement. This allows selection of individual molecules [27], or even atoms [28] to be studied. The AFM can also measure stronger adhesion forces than optical tweezers, which are limited by the low stiffness and short linear range of the optical trap to forces below 10 pN. AFM can therefore measure strong specific interactions and increase the dynamic range of Kinetic Force Spectroscopy measurements.

1.2.2 Technological advances in AFM

Since its invention, the AFM has seen many technological advancements. Probably the most important of these was the replacement of the scanning tunneling microscope (STM) for detection of the cantilever deflection by the optical lever technique [29,30]. Although atomic resolution [31], and even live cell imaging [32] could be obtained with STM detection in liquid, the ease of use of the optical lever and its high sensitivity (see paragraph 3.2.1 of this thesis) have greatly sped up the workflow of AFM measurements.

An important advancement for imaging soft polymers and biological systems was the invention of the tapping mode, or intermittent contact mode of imaging [33]. This mode, where the cantilever is excited close to its resonance frequency and the tip comes into repulsive contact (taps) during every oscillation, allows high-resolution imaging in gases and liquids with reduced lateral forces [34,35]. Although dynamic modes of operation had been used from the beginning, efforts had been focused at non-contact operation, where only the long-range interactions with the surface are probed. The problems associated with the weak distance dependence of these interactions and with instabilities due to capillary condensation were solved by using the tapping mode. Another important advantage of tapping mode is that it is much less sensitive to drifts in the detection system. High-resolution imaging in vacuum was greatly advanced by the introduction of frequency-modulation AFM [36]. The recent application of frequency modulation to measurements in liquids [37-39] shows great promises. Apart from the two modes mentioned above, a great variety of methods for imaging and the application and measurement of forces with the AFM has been developed in the past two decades.

The original handmade cantilevers of the AFM were replaced by significantly smaller batch-microfabricated cantilevers [40], which could soon after be equipped with integrated tips [41]. These cantilevers had dimensions between 100 and 200 μm in length and around 20 μm in width. Present day cantilevers have very similar dimensions. Binnig and co-workers already proposed in the original AFM paper [15] that lowering the mass of the cantilever would improve the measurements, because low-mass cantilevers have smaller spring constants for the same resonance frequency. Moreover, when operating in gases and liquids, the damping decreases with size (see chapter 2 of this thesis and references therein). These observations led in 1996 to the development of cantilevers an order of magnitude smaller [42] than those of Albrecht. To image with high speeds in tapping mode in liquids, such cantilevers are a prerequisite, as was shown by work of the Hansma group in the late 1990's [43-45]. To fully make use of the high-speed potential of small cantilevers, the entire feedback loop of the AFM must be fast. That it is possible to obtain real-time (>10 frames/s) images with feedback using tapping mode in liquid was demonstrated first by Ando and his group at the Kanazawa University [46]. Since then, the two aforementioned groups have improved greatly on their developments [47-55]. Low-noise force measurements with small cantilevers were also demonstrated [56,57]. Unfortunately, the great potential that these cantilevers have is only available to those that invest the effort into developing the cantilevers and the instrument themselves, since no commercial small cantilever AFM is available at present.

1.3 Outline of this thesis

This thesis describes the development of a number of tools that help to advance the sensitivity of measurements in fluids with Atomic Force Microscopy towards the fundamental limits, and the application of these tools to the measurement of hydrophobic forces.

Chapter 2 describes the implications of the fluctuation-dissipation theorem for the sensitivity of AFM measurements. A framework is developed to quantitatively evaluate the noise force acting on an AFM cantilever, and the implications of this noise force are investigated for different types of AFM measurements. It is found that the noise force due to thermal fluctuations in fluids decreases with the size of the cantilever. Some implications of both the fundamental and the instrument noise on experimental sensitivity are discussed.

In chapter 3 two methods are presented for producing miniature cantilevers ten times smaller than currently available types. The limits of the most common method of detecting cantilever motion are explored, and it is found that even in an ideal situation, laser shot noise limits the

sensitivity. A set-up is presented that can detect the forces acting on miniature cantilevers with shot-noise and thermal fluctuation limited sensitivity.

Chapter 4 describes the design of a scanner and electronic modules that together with the detection system developed in chapter 3 and a set of LPM CAMERA control electronics, make up an AFM system for imaging and force-volume measurements. The performance of this AFM system during normal and high-speed scanning is evaluated.

In chapter 5 a new method for extracting quantitative data from Amplitude Modulation dynamic force-distance measurements is developed. The method is based on the harmonic oscillator model of vibrating AFM cantilevers, and is capable of extracting both the conservative and dissipative part of the tip-sample interaction from a measurement of oscillation amplitude and phase as a function of distance.

In chapter 6 the validity of the force extraction method developed in chapter 5 is tested for a number of experimental situations by simulating these experiments with a numerical model. It is shown that the reconstruction of force and damping profiles from amplitude and phase versus distance curves can be accurate even when the basic assumptions for the validity of the harmonic oscillator model are not valid. The influence of cantilever properties and experimental parameters on the validity of the model and on the noise in the extracted force and damping are investigated.

Chapter 7 brings together all the elements of the previous chapters to present a measurement of hydrophobic forces experienced by a carbon nanotube tip when it is in proximity to a surface with nanoscopically small domains of hydrophilic and hydrophobic molecules.

2 General considerations about noise and bandwidth in Atomic Force Microscopy and Spectroscopy

2.1 Introduction

This chapter focuses on the fundamental and practical resolution limits of scanning force microscopy. The three most important quantities whose resolution is limited are force, position and time. The limits that can be achieved for these three quantities will be shown to be highly interdependent. The choice of cantilever properties is most important in deciding which limits apply. Furthermore, they depend strongly on the nature of the system under study.

2.2 Thermal limits in cantilever-based technologies

In general, the method by which forces are measured in cantilever-based technology, is the measurement of the displacement of the cantilever from an equilibrium position. For a cantilever of homogeneous cross-section this displacement is governed by the beam deflection function:

$$EI(\ell)\frac{\partial^4 z(\ell,t)}{\partial \ell^4} + \rho_L \frac{\partial^2 z(\ell,t)}{\partial t^2} = F_L(\ell,t)$$

Where z is the displacement, ℓ is the position along the cantilever E and I are the Young's modulus and moment of inertia of the cantilever, ρ_L is the mass per unit length and F_L is the force per unit length acting on the cantilever. In AFM technology, the forces of interest act upon the tip, which is usually located close to the unclamped end. A cantilever of length L that has small, constant forces applied to the end ($\ell = L$), the cantilever behaves as a Hookian spring with force constant $k_c = 3EI/L^3$. The force constant is also known as the spring constant or stiffness.

In scanning force microscopy and spectroscopy, forces are measured as a function of the tip position in the direction perpendicular to a surface. Both the force and the position are subject to thermal fluctuations, which poses limits to the achievable resolution.

2.2.1 Thermal forces acting on a free cantilever: the noise

Even when the tip is free, and no driving forces are applied to it, there is still a force acting on the cantilever. The fluctuation-dissipation theorem, as formulated by Callen and Welton in 1951 [58], states that any linear dissipative system in thermal equilibrium with a bath will feel a fluctuating force with magnitude:

$$\langle F_{th}^2 \rangle = \frac{2}{\pi} \int k_B T R(\omega) d\omega \quad (2.2)$$

Here, k_B is the Boltzmann constant, T is the temperature, and $R(\omega)$ is the - in principle frequency-dependent - proportionality constant in the linear relation between the dissipated power and the square of the magnitude of a perturbation in a (generalized) position coordinate. In the case of a cantilever $R(\omega)$ is the proportionality constant in the relation which couples the velocity of the cantilever to the damping force it experiences, $F_d = R\dot{z}$. Apart from this, equipartition demands that the potential energy in each mode of oscillation of the cantilever is equal to the thermal energy:

$$\frac{1}{2} k_c \langle z^2 \rangle = \frac{1}{2} k_B T \quad (2.3)$$

Equation (2.2) sets a fundamental limit to the forces that can be measured with cantilever technology. It also points towards the strategy that is to be used to keep this limit as small as possible:

1. Reduce the measurement bandwidth
2. Reduce the temperature
3. Reduce the damping

The different parts of this threefold strategy can be applied separately, or in combination. Reducing the measurement bandwidth is a very general way of increasing the resolution. But this cannot always be done. For example, reducing bandwidth is not an option when dynamic processes are to be measured, or a limited timeframe is available for measurement. Generally, it can be said that the system under study and the boundary conditions of the measurement determine the minimum bandwidth.

The second option is often a very effective one, since lowering the temperature not only reduces the thermal force, but also decreases electronic noise and thermal drift effects. A recent example of the success of this strategy is shown by Hembacher *et al*, obtaining subatomic resolution images [59] and high-resolution dynamic force-distance curves [60] on graphite surfaces. However, for many systems, like biological systems or the study of liquids, lowering the temperature is not an option.

From the previous discussion it is clear that the most accurate criterion for determining the thermal force limit in a mechanical force measurement system operating at temperature T and in a bandwidth $B = \omega_1 - \omega_2$ is the thermally corrected average force noise spectral density:

$$F_{th}(\omega_1, \omega_2) = \sqrt{\frac{\pi}{2k_b TB} \int_{\omega_1}^{\omega_2} R(\omega) d\omega} \quad (2.4)$$

We see that this spectral density depends only on the damping. There are two contributions to the resistance of a cantilever: internal dissipation and dissipation due to the surrounding fluid (liquid or gas). The internal dissipation is the dominant factor at low gas pressures ($\ll 1$ mbar), but at atmospheric pressure or in liquids, the fluid damping dominates.

2.2.2 Influence of size on the noise level

Gittes and Schmidt [61] first realized the influence of the damping coefficient on force resolution, and presented a formula similar to equation (2.4) that describes the signal-to-noise ratio for optical tweezers or AFM experiments. It is immediately clear that apart from the fluid properties, the size of the cantilever is the most important factor in determining the amount of damping. Miniaturized cantilevers have already been shown to outperform standard cantilevers in terms of imaging bandwidth [43,44,46-49,53] and force noise [42,56,57]. However, to our knowledge the optimal geometry was not investigated in detail before. Contrary to optical tweezers' beads, the dimensions of the cantilever strongly influence the stiffness, and cantilevers are often underdamped, so resonance effects play a role. To accurately describe the fluid damping, we need a model that describes the motion and resistance of a cantilever in fluid. For rectangular cantilevers with uniform cross section of width W and thickness H , and $L \gg W \gg H$, this model was provided by Sader in a ground-breaking paper in 1998 [62]. The results of this were experimentally verified to hold for typical rectangular AFM cantilevers [63], and later generalized for other geometries [64]. The exact formulation is rather complicated and mathematical, and will not be repeated here, but the essence can be formulated in the following way:

Due to the presence of hydrodynamic forces, the mass term ρ_L in equation (2.1) has to be replaced by a term that includes the added mass of the fluid that moves along with the cantilever, and a damping term to account for viscous drag has to be added. The inertia and viscous damping of the fluid depend on the shape of the flow and the frequency, and are described accurately by the hydrodynamic function $\Gamma(Re)$. This is a complex function, which depends on the geometry and frequency through the Reynolds number Re . In a fluid with density ρ_f and viscosity η , the Reynolds number relevant for the flow regime of interest is given by $Re = \rho_f \omega W^2 / 4\eta$. The real part of the hydrodynamic function is related to the added inertial mass, while the imaginary part describes the damping. The hydrodynamic function can be calculated analytically for an infinite

length cylinder, and is empirically corrected for a beam by multiplying it with the ratio of two polynomials in Re .

Using the correct Green's function, the impulse response of the cantilever in the fluid can be calculated, and it can be decomposed into its different modes. The functional shape and impulse response of each mode can be used to calculate the expectation value of the potential energy as a function of excitation amplitude, which is used to normalize the force through the scaling imposed by equation (2.3). Note that this means that the thermal forces driving each mode are in principle different. If the spectral behavior of the force noise is assumed to be white, the spectral density of the thermal motion of the cantilever can be calculated.

In order to compare the noise properties of different cantilevers to each other, a routine was written in MatLab (The MathWorks, Inc) that implements the full viscous Sader model to calculate cantilever thermal spectra in viscous fluids. Cantilever dimensions and material constants serve as inputs, as do the material constants of the fluid. Three versions of the program were made, allowing the user to choose the level of detail: only parametric information (resonance frequency and quality factor and force noise level of the first mode), the entire spectrum of the first mode evaluated at the free end of the cantilever, or the spectral density of multiple modes as a function of frequency and position along the cantilever. Calculated thermal spectra of the first flexural mode for several cantilevers in water at room temperature are shown in figure 2.1.

From the thermal spectrum, we can extract the noise force spectral density by multiplying the DC motion spectral density by the spring constant. Force noise of all the cantilevers is plotted in figure 2.2 versus the position noise, which is taken to be the maximum value of the position spectral density curve. The spring constant and cantilever size are both important factors in de-

Table 2.1 Properties of cantilevers used to generate figures 2.1 and 2.2

Cantilever	spring constant (N/m)	length (μm)	width (μm)
Contact Mode, standard	0.08	180	40
Frequency Modulation, standard	2.1	250	30
Tapping Mode, standard	35	125	40
BioLever	0.02	60	25
Contact Mode, miniature	0.08	20	2
Frequency Modulation, miniature	2.5	20	2
Tapping Mode,miniature	36	20	2
Gold nanowire	1.9	1	0.1

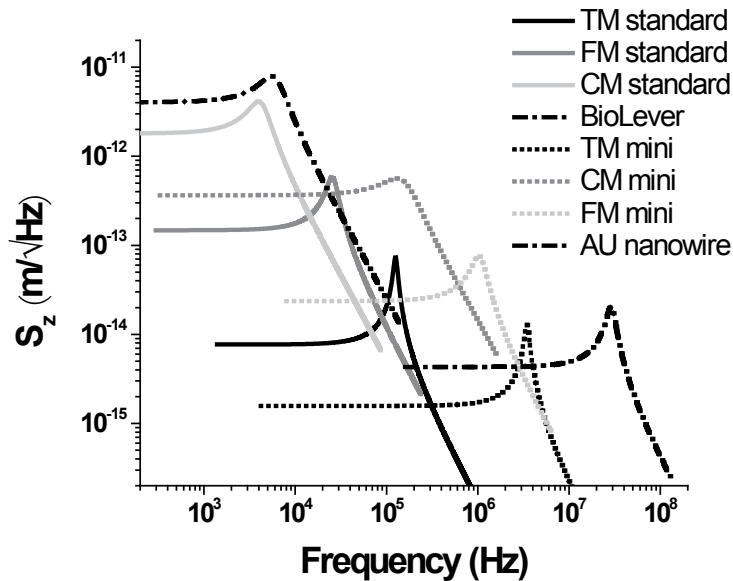


Figure 2.1 Calculated thermal motion amplitudes for several cantilevers

Thermal motion spectral densities in water at room temperature of a selection of commercially available cantilevers compared to their miniature counterparts, and a gold nanowire cantilever.

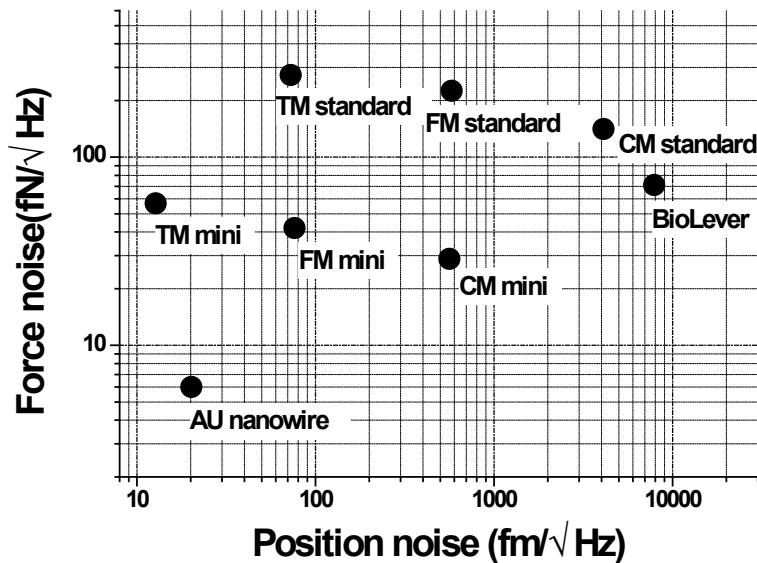


Figure 2.2 Force noise versus position noise in water at room temperature for several cantilevers

Both in terms of position and force noise, miniaturized cantilevers outperform their larger sized counterparts by an order of magnitude. For this graph, position noise spectral density is evaluated at the maximum of the transfer function.

termining the position noise, while for the *force* noise the cantilever size is the major determinant, with the spring constant only having a minor influence.

From equation (2.4) it was already clear that the force noise depends on the damping. Naively one might have guessed that the damping would be due to an equivalent of Stokes drag, with a frequency-independent damping that scales linearly with the geometric mean of the cantilever dimensions: $R = C * \eta \sqrt{LW}$, with C a constant. This would have led to a difference in force noise between the contact mode cantilever and the gold nanowire of a factor 268. Disappointingly, the real difference is only a factor 23.

The explanation for this is that the damping depends not only on the dimensions of the cantilever, but also on the oscillation frequency, with the damping increasing for higher frequencies. This is not surprising when one realizes that the Reynolds number (Re) in water evaluated for typical cantilevers at their resonance frequencies is between 1 and 50, and the Stokes equation for the drag force can only be used for $Re \ll 1$. In fact, the hydrodynamic resistance for an oscillating cantilever is given by $R(\omega) = \pi \rho_f \omega \alpha_L L W^2 \text{Im}(\Gamma(\omega))$, where α_L is a constant that corrects for the mode shape, with a value of 0.24 for the first flexural mode of a beam. The increase of damping with frequency is not very strong: it is almost constant at low frequencies, and increases as $\omega^{1/2}$

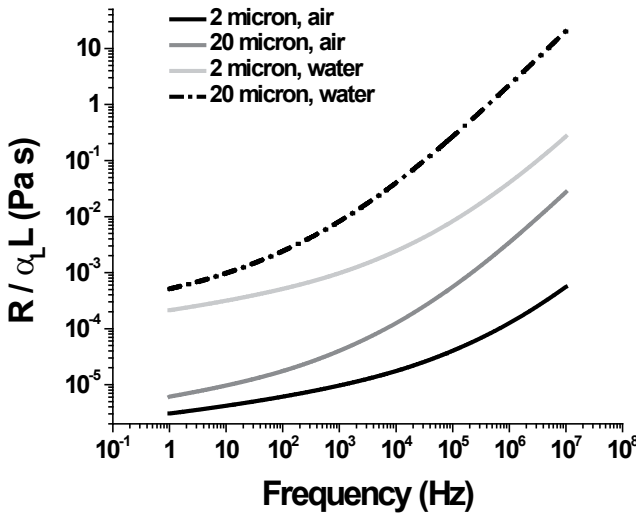


Figure 2.3 Hydrodynamic resistance as a function of frequency for cantilevers of different width in air and in water

Hydrodynamic resistance per unit of cantilever effective length plotted against frequency for air (solid lines) and water (dash-dotted lines). Resistance curves are plotted for cantilevers that are 2 μm wide (black lines) and 20 μm wide (grey lines). The sharper increase in resistance happens at lower frequencies for wide cantilevers.

at high frequencies. The narrower the cantilever, or the lower the kinematic viscosity of the medium, the higher the transition frequency. This is illustrated in figure 2.3. Despite the increase of the damping with frequency, decreasing the dimensions still substantially decreases the force noise for cantilevers with comparable spring constants. Especially decreasing the width is effective, since this lowers the resistance without increasing the resonance frequency.

It should be noted that the increase of damping with frequency implies that the force noise is not white noise. A more exact method of calculating the thermal motion spectrum is therefore to calculate the transfer function of the cantilever in the fluid, multiply this with the force noise spectrum, and then to normalize the resultant motion spectrum through the equipartition law. Paul *et al* [65], using the hydrodynamic function for a cylinder, found that this correction has the most pronounced effect for very thin cantilevers.

2.3 Choosing the right cantilever to optimize signal-to-noise ratio

Now that we can calculate the noise spectral density of cantilevers, it becomes possible to select the cantilever that gives the best signal-to-noise ratio for a specific type of measurement. To do this we first need careful consideration of the selection criteria. We consider here three types of AFM measurements, which each have specific demands:

1. Imaging on hard samples
2. Imaging on soft samples
3. Force versus distance measurements

In AFM imaging, the topography of a sample is obtained by measuring which separation between the cantilever-holder and the sample gives a constant applied force as the sample is scanned. A feedback system keeps the force constant. In force versus distance measurements [5], the relative position of cantilever and sample is varied only in the direction perpendicular to the sample, and the response of the cantilever is measured. The word “force” should be interpreted in a generalized way in the following paragraphs, since many different quantities derived from a measurement of the cantilever position can be used for feedback. These include the static bending of the cantilever (in contact mode AFM), oscillation amplitude (in intermittent contact mode AFM), and cantilever effective resonance frequency (in frequency modulation AFM).

The demands and resulting choices for the optimum cantilever for each of the situations enumerated above are discussed in the paragraphs below. Specific attention will be given to the benefits

of using miniature cantilevers in each case. A benefit that applies to all cases is that the usable bandwidth of smaller cantilevers is larger.

2.3.1 Imaging on hard samples

In an ideal situation, the applied force during AFM imaging has no influence on the sample's topography. We define a sample as "hard" when the contact stiffness k_{is} is much larger than the cantilever stiffness k_c . Note that it is the combined stiffness of both tip and sample that determines the contact stiffness. If the sample is very stiff, but the tip is not, the analysis given below on imaging soft samples applies.

Scanning on a hard sample implies that the value of the constant force or amplitude reduction has no significant effect on the measured topography. This means that only the minimization of position noise can improve the image quality and therefore this is what determines the optimal cantilever. High spring constants are therefore preferred for imaging on hard samples. Position noise cannot be minimized indefinitely by choosing a stiffer cantilever, since position detection is limited in its accuracy (see Chapter 3), and the electronics of the scanning system and feedback introduce noise as well. To make sure that the cantilever's thermal motion does not increase the

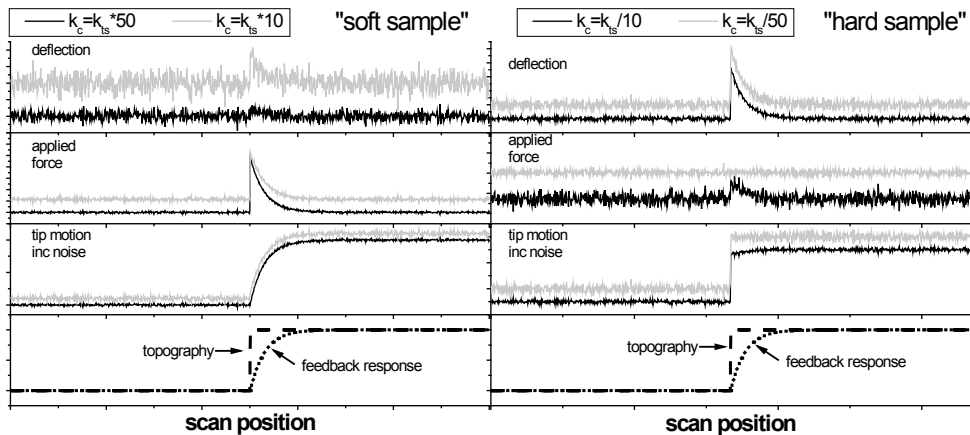


Figure 2.4 Effect of cantilever stiffness on image quality and applied force for soft and hard samples

These graphs were calculated on the basis of the topography and feedback response shown in the bottom graphs and assuming a white noise spectrum for the cantilever motion. On a soft sample (left), the cantilever hardly deflects, and the applied force is governed by the sample stiffness and cantilever deflection. A stiffer cantilever (black lines) applies less Brownian motion induced force and gives less imaging noise, but accurate feedback is more challenging since the deflection is so small. On a hard sample, the tip follows the topography independent of feedback action. The applied force, whether due to Brownian motion or feedback error, is more for a stiffer cantilever, but image noise is less. The noise shown is noise in the entire cantilever bandwidth. Instrument noise and feedback reaction to cantilever position noise were not taken into account, and the cantilever's reaction time was assumed to be negligible.

noise of the entire system, a cantilever should be chosen with Brownian motion spectral density slightly below the instrument noise spectral density. When the cantilever quality factor is high, dynamic operation around resonance requires stiffer cantilevers for instrument noise limited measurements.

An additional advantage of measuring on hard samples is that feedback error can be corrected without extensive knowledge of the sample's mechanical properties. As long as the feedback parameter (deflection or amplitude) is in a range where it is linear around the setpoint, and the proportionality constant is known, the recorded error signal can be used to correct the measured topography.

Using smaller cantilevers can aid in lowering the spring constant at which the noise is no longer limited by cantilever thermal motion. This in turn widens the range of samples that can be qualified as "hard" and limits tip wear.

One caveat has to be mentioned when applying the noise analysis of paragraph 2.2.1 to contact mode imaging on hard samples. When the contact stiffness is large, the mechanics of a clamped-free cantilever beam no longer applies. The cantilever will behave more like a clamped-pinned beam, which has a higher spring constant and hence lower thermal motion amplitude. The mode shape is also very different, with (almost) zero amplitude at the tip and maximum amplitude at half the cantilever length. Since most detection setups in AFM measure bending of the cantilever rather than position of the tip, thermal vibration will still be detected as noise in the position of the tip. Nevertheless, qualitatively the scaling of the noise with cantilever size and spring constant is similar.

2.3.2 Imaging on soft samples

For the following paragraph, we will define a soft sample as a sample on which the contact stiffness k_{ts} is considerably lower than the cantilever stiffness. This implies that the applied force has influence on the sample topography. Sometimes the sample can even be damaged by applying a too high imaging force. While on hard samples only the position noise has to be minimized, on soft samples both the position noise and the applied force need to be kept at a minimum, which leads to conflicting demands.

The force that the tip applies to the sample can be divided into three parts: the setpoint force, the error force and the noise force. To closely approximate the topography in the unperturbed state, the setpoint force should be kept to a minimum. In principle the force noise spectral density and feedback bandwidth determine the minimum force that can be detected. But a finite region

around the setpoint is needed where the force is monotonic in the position to ensure stable feedback during imaging. Though special adaptive methods can be used to make it possible to ensure stable feedback even for a very narrow region that is monotonic [52], this requirement favors the use of compliant cantilevers.

Error in the imaging feedback will cause an error in the applied force, which in turn leads to an error in the topography that depends on the local mechanical properties of the sample. Part of this error may be caused by electronic noise sources in the feedback loop, but some amount of error is always present in any feedback system. Unless the local indentation-versus-applied-force profile of the entire scanned area is known, this error cannot be corrected.

The peak value of inherent feedback error depends on the ratio of the temporal bandwidth of topography changes (i.e. the product of tip speed and maximum local slope of the sample) and the closed-loop feedback bandwidth. Keeping feedback error small is more challenging with stiff cantilevers on soft samples, since the cantilever's response to changes in topography is smaller, which leads to a higher relative importance of electronic noise sources in the feedback loop. Even more so when the sample contains both hard and soft regions, as the feedback gain must be adjusted to the stronger response on the hard regions to avoid instability.

On soft samples, the fluctuations in the position of the cantilever will be transferred to the sample, leading to fluctuations in the applied force. If the cantilever is much stiffer than the sample, it is the position noise (integrated over the entire cantilever bandwidth), not the force noise that determines the applied force due to Brownian motion. Imaging feedback will increase the force applied to the sample due to Brownian motion of the cantilever, as it will try to compensate for the noise force by applying a force to the sample. Therefore, using a cantilever that has a lower position noise (integrated over the feedback bandwidth) lowers the applied noise force. When there is a choice between two cantilevers with $k_{1s} \ll k_1 < k_2$ – contrary to many users' intuition – the applied noise force due to Brownian motion on soft samples is minimized by choosing the stiffer cantilever.

Using smaller cantilevers can be very beneficial when imaging on soft samples. The low position noise spectral density that can be achieved even for relatively compliant cantilevers decreases both the applied noise force due to Brownian motion and the image noise. The latter is often dominated by instrument noise when stiff cantilevers are used, but with compliant cantilevers there is still a lot to gain by decreasing the cantilever's Brownian motion in the feedback bandwidth. The differences between imaging on hard and soft samples are illustrated in figure 2.4.

2.3.3 Force versus distance measurements

For force versus distance measurements the distinction between hard and soft samples is not so easily made, because often the interaction stiffness varies over the region of the measurement. Three competing demands for an optimal force measurement can be distinguished:

1. Minimization of noise in the measured force
2. Minimization of error in the tip-sample separation
3. Minimization of noise in the applied force

The relative importance of each of these demands depends on the objective of the measurement.

The noise in the measured force in a bandwidth $B = \omega_1 - \omega_2$ can be expressed as

$$\delta F_n = \int_{\omega_1}^{\omega_2} S_F(\omega) \sqrt{1 + \left(\frac{S_{zd}(\omega)}{S_z(\omega)} \right)^2} d\omega \quad (2.5)$$

S_F is the force noise spectral density of the cantilever, S_z is the Brownian motion spectral density of the free cantilever (the quantity S_F/S_z is the cantilever's transfer function), and S_{zd} is the detection noise spectral density. Minimizing the force noise is achieved by using a cantilever with a low force noise spectral density, i.e. a small cantilever. However, when the Brownian motion in the measurement bandwidth is smaller than the detection noise, the force noise increases. The detection noise term is approximately proportional to the spring constant. In the frequency range around the resonance frequency of the cantilever the force noise due to detection noise is minimized. If the detection noise term is negligible compared to the thermal noise, the force measurement noise is nearly independent of the spring constant.

The error in the tip-sample separation is only the error due to instrumental noise, since the Brownian motion is not noise in the strict sense of the word, but a real fluctuation in the position of the tip. Nevertheless, these position fluctuations can introduce an error in the force-distance measurement other than the force noise. The measured force at any single point in a force-distance profile is an average over the tip's motion amplitude around its mean position. If the force is not linear in this region, the measured force will not correspond to the actual force. Note that it is not the measured fluctuation (which depends on the measurement bandwidth) but the integrated fluctuation that determines this smearing of the force profile. In force-distance measurements the force can be non-linear even over very short distances. Examples of this are measurements of single molecule unbinding and unfolding [20,21,66], or liquid ordering [67,68]. If the force gradient of the measured potential is steeper than the cantilever spring constant, the root mean square thermal motion will be suppressed by a factor $k_c / (k_c + \langle k_{ts} \rangle)$, which also diminishes the error due to averaging.

If the tip-sample interaction potential contains regions with an attractive force gradient that exceeds the cantilever stiffness an instability in the cantilever position may occur, a phenomenon commonly known as snap-in or jump-in. The information about the force profile in the region that the tip jumps over is lost. Both the smearing out of the potential due to thermal motion and the loss of information through snap-in can be resolved by measuring the cantilever's position with a time resolution better than the response time of the cantilever [69-72]. Snap-in can also be prevented by using a dynamic force measurement technique with sufficient amplitude.

In many applications of force measurements, the force applied by the tip to the sample is an important parameter. For example, in Kinetic Force Spectroscopy, the goal is to measure the maximum force applied by the tip to a bond before the bond breaks. The noise in the force applied to a sample during a force-distance measurement is different from the noise in the measured force. The noise in the cantilever position detection is not of influence, nor is the measurement bandwidth:

$$\delta F_A = \frac{k_{ts}k_c}{k_c + k_{ts}} \sqrt{\delta z_c^2 + \delta z_i^2} \quad (2.6)$$

The applied force is influenced by mechanical noise in the cantilever - the Brownian motion of the cantilever - or in the instrument, the term δz_i originating from electronic noise on the piezo transducer and vibrations in the tip-sample mechanical loop. The quantity δz_c in the formula is the root mean square thermal motion of the free cantilever. Equation (2.6) expresses the noise in the amount of force that can be applied to the sample in a controlled way. The actual uncertainty of the noise applied to the sample can be reduced by measurement of the tip position. Force applied to the sample in the measurement bandwidth is detected through the detection of cantilever deflection if the Brownian motion spectral density of the cantilever *coupled to the sample* is above the noise floor. It is the undetected part of the cantilever motion, outside the detection bandwidth, that leads to an uncertainty in the applied force. Using small cantilevers, with a large bandwidth, can therefore increase the uncertainty in the applied force. A proven strategy to reduce the influence of applied force noise is to couple the cantilever to the sample through a flexible linker with a spring constant considerably lower than that of the cantilever. This was shown to reduce the uncertainty in the lifetime of single-molecule bonds as determined by Kinetic Force Spectroscopy [73].

Summarizing, the noise in force measurements is nearly independent of spring constant and can be greatly reduced by using small cantilevers, unless the instrument noise is the limiting factor. Using cantilevers with higher spring constants reduces snap-in and increases positional accuracy in a force-distance measurement, but the applied force uncertainty may be larger and the relative importance of instrument noise increases.

3 Design and performance evaluation of a versatile miniature cantilever optical deflection detection system

In the previous chapter, the use of small cantilevers was proposed as a means to improve time, force and position resolution of atomic force microscopy. This chapter describes some practical demands on miniature cantilevers, as well as two methods to fabricate devices that fulfill these demands. A deflection detection system was developed to detect the motion of these cantilevers. The theoretical limit for the sensitivity of such an optical beam deflection detection system is derived. It is shown that for several different cantilevers this system's sensitivity closely approaches the maximum signal-to-noise ratio that can be attained in theory.

3.1 Cantilever fabrication

Currently, the vast majority of Atomic Force Microscopes use optical beam deflection detection systems with laser spot sizes of a few tens of micrometers in width. This poses a lower limit for the lateral dimensions of cantilevers that can be used in these instruments. Commercial availability of cantilevers of smaller sizes has therefore remained problematic. Although several publications about miniature cantilever fabrication have appeared in the literature in the past ten years [45,48,57,74-76], no cantilevers shorter than 60 μm or narrower than 20 μm have appeared on the market. To our knowledge only one company is now offering miniature cantilevers as a commercial product [77], but developments are still in a prototype stage. This paragraph describes two alternative methods for the fabrication of cantilevers optimized for low-noise, high-speed operation in liquid.

An issue that specifically deserves additional attention in the fabrication of short cantilevers is corner clearance. This phenomenon is illustrated in figure 3.1A. AFM support chips are usually placed under an angle of 12-14 degrees to ensure that only the tip touches the surface. In the direction perpendicular to the cantilever length axis, the support chip must be mounted parallel to the surface. The degree of parallelism that is required depends on the width of the support chip W_s , the cantilever length L , the angle α_1 , and the tip height h_t .

$$\sin\alpha_2 < \frac{L\sin\alpha_1 + h_t}{\frac{1}{2}W_s} \quad (3.1)$$

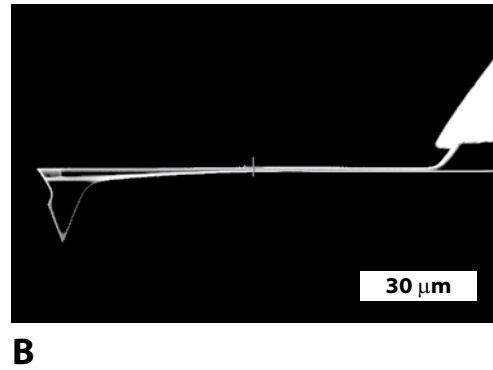
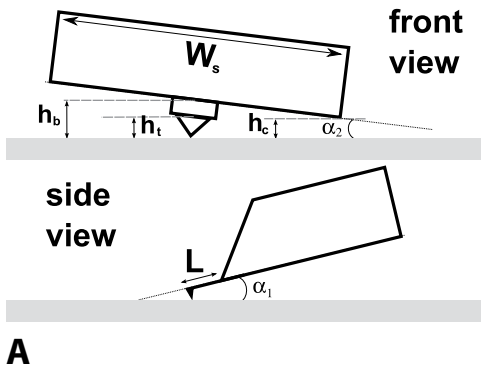


Figure 3.1 Illustration of corner clearance

A: The height h_b of the cantilever base above the sample increases with the length of the cantilever. The corner clearance h_c is therefore lower for smaller cantilevers.

B: A MicroMasch NSC19 cantilever with elevated base.

For a typical commercially available cantilever of 200 μm in length, mounted centrally on a chip with a width of 2 mm, and with a tip height of 10 μm , this amounts to a maximum angle of ± 3.3 degrees. Miniature cantilevers of 15 μm in length will usually have a smaller tip height, say 2 μm . If such a cantilever is mounted on the same chip, the maximum tilt angle is only 0.3 degrees. This is not enough. For practical operation on flat surfaces, a minimum angle tolerance of somewhere between 1 and 3 degrees is desirable, depending on the apparatus. One trick manufacturers of cantilevers have used is to etch the corners off the support chips, effectively reducing the chip width. But often this reduction is merely a factor of 2, leading to a still unacceptable angle tolerance of 0.6 degrees. A more effective tactic is to elevate the base of the cantilever with respect to the support surface. This is illustrated in figure 3.1B by an electron micrograph of a silicon cantilever made by MicroMasch. This can be done quite easily, and immediately gains extra clearance. With an extra 20 μm of elevated base height, the angle tolerance increases to 1.5 degrees, and to a comfortable 2.9 degrees if combined with narrowing the chip front.

3.1.1 Focused Ion Beam modification of existing cantilevers

A simple way to create smaller cantilevers is to take commercially available cantilevers and cut them down to the desired size using a Focused Ion Beam (FIB). The FIB is a tool that uses electrostatic lenses to focus a beam of accelerated ions (usually gallium) onto a sample. The secondary electrons that are produced in this way can be used for imaging. But more importantly, the energetic ions can be used to mill material away. Material can also be deposited, if a precursor gas is let into the chamber and cracked by the ion beam. This is not a method suited for mass production of cantilevers, but it is a relatively easy way to get the right size of cantilever in a short amount of time, especially for those who have limited access to microfabrication facilities.

All the FIB processing described here was done on an FEI Strata DualBeam 235 system, equipped with both electron and ion beams. This allows imaging and coarse alignment of the cantilevers without the destructive action of the ion beam. Unfortunately thermal drift effects and tiny misalignments of the two columns necessitate imaging with the ion beam prior to every patterning step. For deposition of material, the system was equipped with a Gas Insertion System containing trimethyl(methylcyclopentadienyl)platinum.

Starting material

The base material, the starting cantilever, should be chosen with care. The starting cantilevers should have the right thickness. Thinning a cantilever with the FIB creates a lot of stress in the material. When the thinning is done by ion bombardment from the top, the thinning will be very inhomogeneous, creating large surface roughness. Thinning from the side avoids this, but the alignment on high length-to-thickness ratio cantilevers is almost impossible, as the cantilever will bend during the milling.

Milling away large amounts of material from the support chip is very time consuming, therefore a cantilever with base elevation and narrow front support chip is preferred. Unfortunately, thin cantilevers such as the Olympus Biolever and other Si_3N_4 cantilevers have wide rectangular chips and no base elevation. Several manufacturers offer silicon cantilevers with elevated bases, but most of these have thicknesses of 1 to 7 μm , compared to 150 to 800 nm for silicon nitride. The most suitable cantilever that is commercially available at this moment is the MicroMasch NSC19, a 1 μm thick silicon lever. A prototype silicon cantilever that was received as a kind gift from Nanoworld AG was also used in our work. This cantilever, the Arrow UHF, was 600 nm thick and had a 40 μm base elevation.

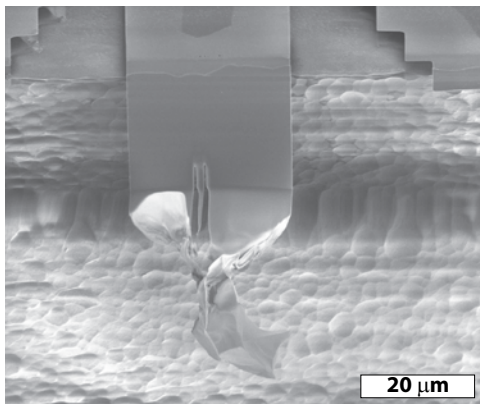


Figure 3.2 Deformation of cantilever remains during coarse milling

In the last stages of milling a thin flexible structure such as a cantilever, a very thin membrane remains. During milling, this membrane will deform, and often bend either over or under the part of the cantilever that is not to be milled away. This makes further processing impossible.

Fabrication process

The fabrication process consists of four steps: coarse milling, tip pedestal deposition, fine milling, and tip deposition. The separation into coarse and fine milling is needed to decrease the amount of damage done to the cantilever by unwanted side effects of milling at high ion currents.

Coarse milling

Coarse milling, to remove the largest part of the existing cantilever, is best done at a high beam current, typically 10 to 30 nA. One could either mill away the entire unwanted part of the cantilever, or make only a cut of the outline of the new cantilever. In both of these cases, a problem arises in the last stages of the milling. When the milled part of the cantilever has become very thin, the stress induced by the milling and/or cantilever charging will make the unwanted part of the cantilever bend, move and warp. An example of this warping is shown in Figure 3.2. Based on our experience with about 20 cantilevers, in about 2 out of 3 of cases it will flip over onto the part that has to remain, or otherwise move into a position that cannot be reached by the ion beam. Once this has happened, it is not possible anymore to remove the remaining unwanted part.

The most effective way of removing the large part of the cantilever is to cut the outline, but leave a small part at the base of the cantilever, near the edges. Applying mechanical stress to the cantilever with a sharp needle will then break off the unwanted part of the lever. Even though

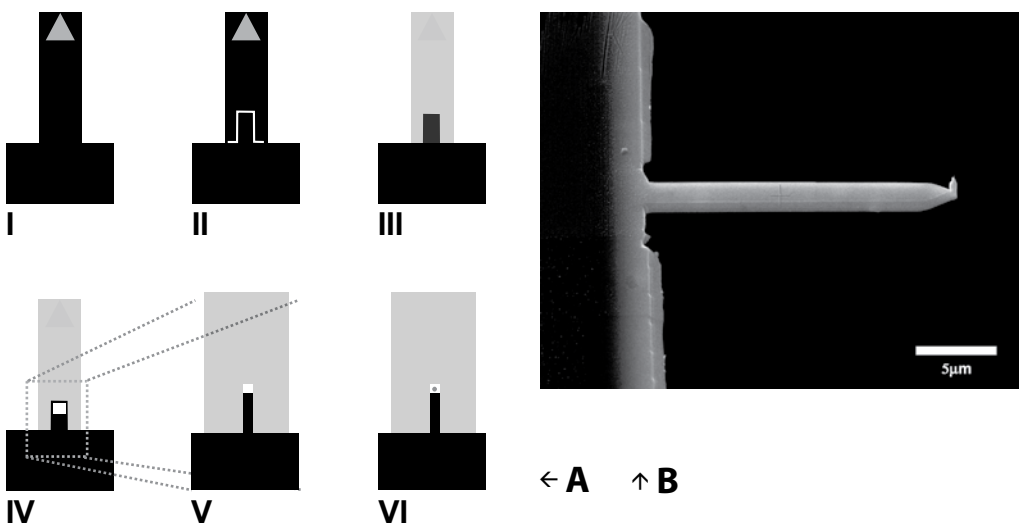


Figure 3.3 Steps in the FIB cantilever production process and finished product

A: (I) Starting situation (II) (optional, see text) coarse outline only milling (III) Main cantilever removal (IV) Tip pedestal deposition (V) Fine milling (VI) Tip deposition or mounting. **B:** Finished cantilever with EBD tip

in most FIB systems this means that the sample has to be taken out, this process is the quickest and most convenient. If done in this way, time for the coarse milling is 2-10 minutes, depending on the size and thickness of the cantilever. Time for venting and pumping down again is about 15 minutes, but when several cantilevers are processed this only has to be done once. Breaking only takes a few minutes.

Deposition

The next step is the deposition of a tip pedestal. This is necessary to increase tip height without creating a very long tip which will bend easily. The final scanning tip can be created by electron beam induced deposition (EBID) or by mounting of a nanowire or carbon nanotube.

Growth speed in Ion Beam Induced Deposition (IBID) depends on the current density. However, it is not linear in the beam current. The growth speed is a balance between the amount of precursor gas that is cracked by the beam, and simultaneous milling of the deposited structure. For precursor gas used, the highest growth speed of platinum is obtained at a current density of $1\mu\text{A}/\text{m}^2$. To deposit small structures like a tip pedestal of $2\times 2\ \mu\text{m}$, a beam current below 10 pA is necessary.

Mounting of nanostructures is facilitated by smooth, steep sidewalls of the tip pedestal. Since milling is faster at the edges of structures, sidewalls of deposited patterns are often rounded near the top. A $2\ \mu\text{m}$ thick pattern deposited on a $2\ \mu\text{m}$ square will have a shape that is more like a pillow than like a cube. Mounting of nanotubes that stick out perpendicular to the cantilever

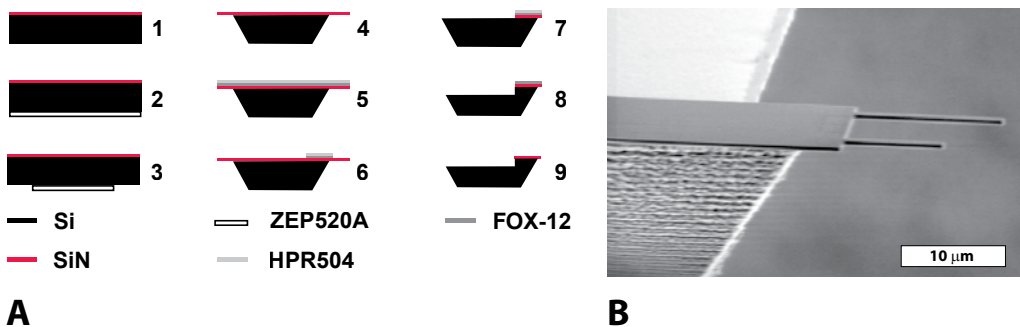


Figure 3.4 Steps in the lithographic cantilever production process and finished cantilevers

A: Steps in the production process. 1) LPCVD deposition of silicon nitride 2) Application of resist on bottom side 3) Patterning bottom side 4) KOH etching through the wafer 5) Application of double layer of resist on tip side 6) Patterning tip side 7) RIE etching of silicon nitride 8) Bosch anisotropic etch of base elevation 9) Mask removal. **B:** Finished chip with two tipless cantilevers of 2×10 and $2\times 15\ \mu\text{m}$

is facilitated when the sidewalls of the tip pedestal are steep and straight. This is why the tip pedestal should be deposited before the step of fine milling. If the pedestal deposited is wider than the final cantilever, its edges are milled away and the sidewalls will be steep and straight. Depositing a 2 μm high tip pedestal takes around 10 minutes of milling time.

Fine milling

Fine milling is done using a patterning mode called “cleaning cross section”, scanning the ion beam one line at a time. If these lines are chosen parallel to the cantilever edge, working from the outside in, membrane formation is avoided and a clean sidewall is obtained. This fine milling is done at a medium current of 300-1000 pA, to prevent damage to the cantilever by scattered ions. Unfortunately, this process takes considerably longer than the time needed for the milling alone. Overhead time in the patterning software can increase the total patterning time by a factor of up to ten. Furthermore, drift in the imaging system and/or the positioning system requires frequent monitoring of the pattern position. Fine milling of an 8 x 25 μm cantilever to a 2 x 20 μm size therefore takes around 45 minutes, and cannot be automated by simple scripting of commands. If scripting can be combined with pattern recognition to correct for drift, this would surely facilitate the production process.

Total processing time for a cantilever with tip pedestal, including alignment and focusing of the different beams needed in the process, is around 2 hours per cantilever.

3.1.2 Lithographically defined cantilevers with elevated base

FIB cutting is not a suited production technique for producing large numbers of cantilevers, since cantilevers are produced in series. Lithographic methods can produce many cantilever chips on a wafer in a single production run. A procedure was developed to fabricate silicon nitride cantilevers with an elevated base on silicon support chips.

A 500 nm thick silicon nitride layer was deposited with low pressure chemical vapor deposition on one side of a double-side polished silicon wafer. The other side of this wafer was spin-coated with ZEP520A positive resist (Zeon corporation, Tokyo, Japan). This resist was patterned and developed to create the support chip shape. The support chips are etched anisotropically with potassium hydroxide, leaving the silicon nitride film intact. Subsequently, the silicon nitride is covered with a double-layer of HPR504 (FujiFilm electronic materials) and FOX-12 (hydrogen silsesquioxane, Dow Corning Inc., Midland, MI, USA) resists. The shape of the cantilevers and the elevated base is defined in the FOX-12 resist by direct electron beam writing and developing in Microposit MF322 (Shibley Company, Marlborough, MA, USA). Reactive Ion Etching (RIE) in oxygen plasma removes the HPR504 everywhere except on the cantilevers and base. A subsequent CHF_3 RIE step etches the silicon nitride away, while the silicon oxide that is formed from

the FOX-12 resist in the previous step acts as a mask to protect the cantilevers and base. A Bosch etch is then used to anisotropically etch the surface of the silicon chip for approximately 20 μm , creating the elevated base. The silicon oxide on the cantilevers and base is also removed in this step, but the HPR504 protects the cantilevers from damage by the reactive ions. A final oxygen plasma treatment removes the HPR504 from the cantilevers.

3.2 Optical detection system

One of the major reasons to use smaller cantilevers is the enhanced noise performance. But this noise performance can only be realized if the thermal noise is the limiting factor rather than the cantilevers' position detection.

The most commonly used way of detection the deflection of an AFM cantilever is the optical beam deflection (OBD) method [29]. Other methods include STM detection (as was done in the first AFM ever) [15], various forms of interferometric detection [30,78-80], and self-sensing techniques based on piezoelectric or piezoresistive effects [81,82]. The principle of the optical beam deflection method is strikingly simple: a laser beam is focused onto the cantilever, and the position of the reflected beam is monitored with a position sensitive photodetector. Despite its simplicity, displacements of the order of atomic diameters can be detected within several kHz of bandwidth. The optical beam deflection method is so popular because of its ease of use (compared to interferometric methods), high sensitivity (compared to most self-sensing schemes), and versatility with respect to the types of cantilevers and environments that can be used. This paragraph describes the design and performance of an optical beam deflection sensor for cantilevers $\geq 1 \mu\text{m}$ in width with shot noise limited performance up to 5 MHz.

3.2.1 Sensitivity limit in optical beam deflection

Before discussing the design, a derivation of the sensitivity limits of an OBD system will be presented. These sensitivity limits were worked out before, in ascending level of detail, by Mayer [29], Gustafson [83], Putman [84] and Schaeffer [85]. The analysis given by Fukuma [86] is very readable and orientated towards practical applications. The analysis presented here is specifically directed at systems using miniature cantilevers, that use lenses with a numerical aperture (NA) of 0.5 or larger. In this situation, it is most convenient to use one lens or objective to focus and recollimate the laser. Separating the incoming and outgoing laser beams may be done by using a quarter wave plate / polarizing beam splitter combination, but it is also possible to separate the laser beams just by a shift of the center position that is greater than half the width, as illustrated in figure 3.5. This requires a sufficiently high numerical aperture of the lens. An added advantage of the spatial separation method is that unwanted reflections from the surface can be completely

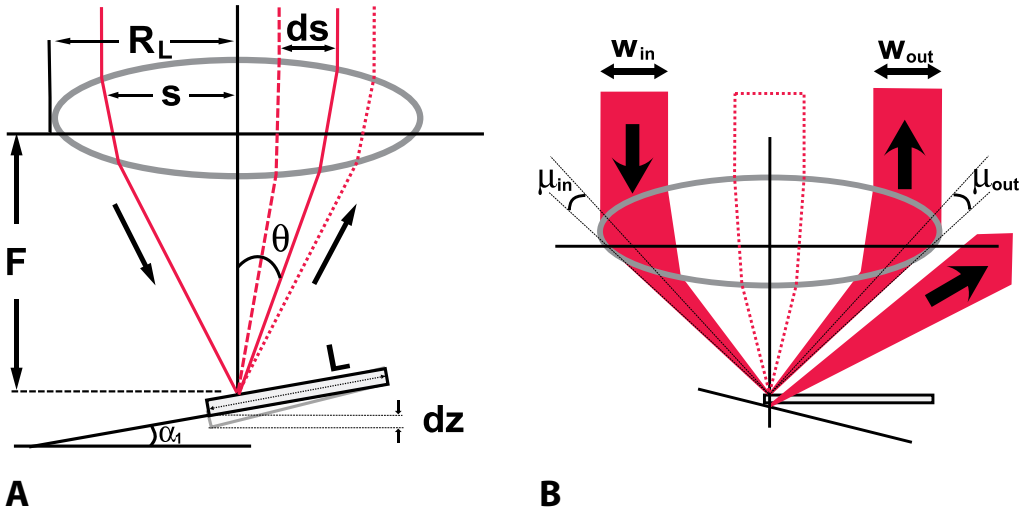


Figure 3.5 Optical path in a single lens optical beam deflection system

A: Schematic of an optical beam deflection setup using a single lens. The optical leverage is attained through the ratio between the cantilever length and focal distance (which should be measured from the front principal plane), but also depends on the eccentricity s . **B:** Surface reflections can be eliminated from the outgoing path by using a strongly eccentric beam. The dashed beam outline illustrates that a centered beam has a higher numerical aperture (opening angle at focus) than an eccentric beam with the same width.

eliminated from the detector path. Although the influence of cantilever tilt and eccentricity could in principle be calculated with the formulas from reference [85], the more simplified approach used here is easier to apply to a practical situation.

Suppose a laser beam comes into a focusing element with focal length F parallel to the optical axis, but at a distance s from this axis, and is reflected by a cantilever of length L , tilted under an angle α_1 whose end is displaced from equilibrium position by a height dz , then the displacement of the laser beam central ray from its equilibrium position is amplified by:

$$\frac{ds}{dz} = \frac{2F}{L} (1 + \tan^2(\theta)), \quad \theta = \arctan\left(\frac{s}{F}\right) - 2\alpha_1 \quad (3.2)$$

This value is called the optical leverage. We treat the cantilever as a flat, hinged plate in this analysis. The analysis incorporating the functional shape of the cantilever was done by Schaeffer [85,87], but for now we ignore all the complications this introduces. For a centered beam and a cantilever perpendicular to the optical axis this simplifies to the well known $ds = dz * (2F/L)$. Note that

for a high numerical aperture system, the standard paraxial approximation of $\sin\theta = \tan\theta = \theta$ does not hold, even at zero tilt. Both eccentricity and tilt angle can be negative, and in special cases can cancel each other, but the optical leverage in an eccentric or tilted system is as least as large as that of a centered, perpendicular system.

For the responsivity, the beam displacement relative to its width on the detector is more important than the absolute displacement. The width of the outgoing beam scales as follows:

$$w_{out} = F(\tan(\theta + \mu_{out}) - \tan(\theta - \mu_{out})) \quad (3.3)$$

With w_{out} the outgoing width, and μ_{out} the half opening angle of the outgoing beam. As long as the cantilever is considerably larger than the laser spot size, the outgoing opening angle is equal to the incoming angle, which is related to the incoming beam width via:

$$\mu_{in} = \frac{1}{2} \arctan\left(\frac{2s-w_{in}}{2F}\right) - \frac{1}{2} \arctan\left(\frac{2s+w_{in}}{2F}\right) \quad (3.4)$$

If a split photodiode detector is used, the displacement signal is measured as a change $2d*P_D$ in the difference between the power incident on the two segments of the detector. This change is proportional to the product of ds and P_D , the incident power on the detector, which in turn is the cantilever's reflection coefficient c_r times the incoming laser power P_{in} . Therefore, the optical responsivity can be expressed as:

$$r_o = \frac{2dP_D}{dz} = \frac{2C_g c_r P_{in}}{w_{out}} \frac{ds}{dz} \quad (3.5)$$

If the outgoing beam is not collimated, the width of the beam at the detector may be different, but the ratio of the displacement and width is the same. The quantity C_g is a scaling factor that corrects for a non-uniform beam profile: $C_g = w_{out} P_L / P_D$, with P_L the linear intensity (in W/m) at the position of the slit. For a Gaussian beam with the width defined as the $1/e^2$ width, C_g is $\sqrt{8/\pi}$.

As long as diffraction does not play a significant role, incoming and outgoing beams always have the same width if the cantilever is perpendicular to the optical axis. The width increases more strongly with tilt angle, and less strongly with eccentricity than the optical leverage, leading to the rather surprising conclusion that detection responsivity increases with increased distance of the laser beam to the center. The cantilever tilt angle has very little effect on responsivity at angles below 30 degrees, but the maximum responsivity is at zero tilt.

The numerical aperture of the beam, $NA = n \sin(\mu_{in})$, with n the refractive index of the medium the cantilever is in, determines the size of the spot on the cantilever. Diameter of the diffraction limited spot (distance between the first zeros of the Airy pattern) is $1.22\lambda/NA$, with λ the wavelength of the laser light. When the spot size becomes larger than the cantilever, two effects start to play a role. First of all, the reflected power is decreased because part of the spot is not reflected anymore. Secondly, the width of the outgoing beam is now determined by the cantilever length, instead of by the incoming beam width. These effects can be described with the following two equations:

$$P_D = c_r P_{in} \int_{-L/2}^{L/2} f(x) dx \bigg/ \int_{-\infty}^{\infty} f(x) dx, \text{ with } f(x) = \left(\frac{J_1(2\pi n \sin(\mu_{in})x)}{2\pi n \sin(\mu_{in})x} \right)^2 \quad (3.6)$$

$$\mu_{out} = \max(\mu_{in}, \arcsin \frac{1.22\lambda}{nL}) \quad (3.7)$$

Here the Airy function is used to describe the intensity profile in the focus. The cut-off imposed on the outgoing angle in (3.7) is quite coarse, in reality the transition will be more smooth, see also ref. [85]. Up until this point, we have been concerned only with the responsivity, which tells us about the signal, but the true figure of merit of a detection system is its sensitivity, which is determined by the signal-to-noise-ratio. Fundamental limits on the noise are posed by the shot noise and thermal noise. If the photodiode is connected to an amplifier with feedback resistor R_f , the input referred current noise spectral density will be $\sqrt{4k_b T/R_f}$. Shot noise spectral density is given by $\sqrt{2eI_D}$, where I_D is the current generated by the photodiode, which is simply the product of the diode's responsivity and the incident power. This responsivity can be expressed as a quantum efficiency times the photon energy multiplied by the electron charge: $I_D/P_D = Q_D * (\lambda e/hc)$. It is easily seen that the ratio of thermal and shot noise is $\sqrt{51mV/R_f I_D}$ (at room temperature).

Less fundamental, but equally important in practical applications is the amplifier noise. The most common amplifier circuit for photodiode transimpedance amplification is shown in figure 3.6. The amplifier will have current noise density I_n and voltage noise density V_n . The equivalent current noise corresponding to this voltage noise is calculated by:

$$I_{v,n}(\omega) = V_n \left(\frac{1}{R_f} + \frac{\omega(C_D + C_A)}{1 + R_f C_f \omega} \right) \quad (3.8)$$

where the bracketed term is the voltage amplification divided by the feedback resistance. The noise sources have to be added in quadrature, and each of the two segments has its own amplifier, so that the effective current noise spectral density is:

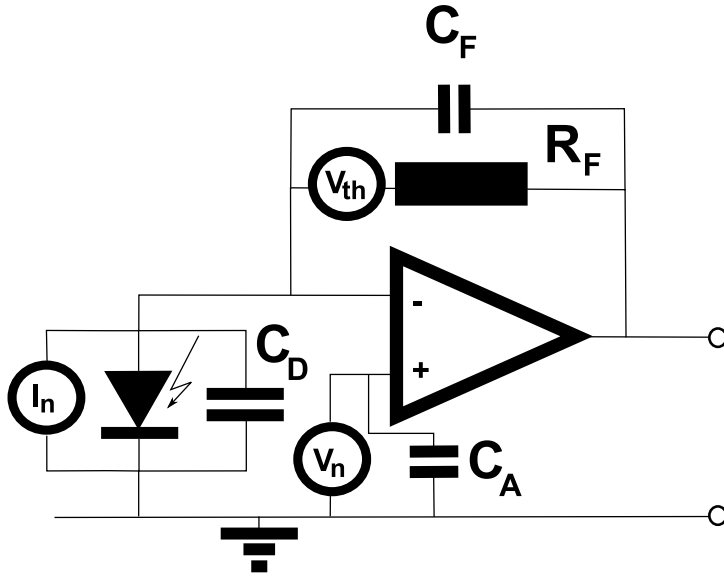


Figure 3.6 Photodiode amplifier with noise sources

The op-amp current noise source is added to the photocurrent and its associated shot noise coming from the diode. The resistor thermal noise is added to the input voltage noise source.

$$I_{n,eff} = \sqrt{2\left(4k_b T / R_f + I_n^2 + I_{V,n}^2(\omega)\right) + 2Q_D \frac{\lambda e^2}{hc} P_D} \quad (3.9)$$

From the previous formulas, we can calculate the output current signal-to-noise ratio spectral density as follows:

$$SNR_I|_{\omega} = S_z \frac{2C_g Q_D \lambda e P_D}{w_{out} \sqrt{2h^2 c^2 \left(4k_b T / R_f + I_n^2 + I_{V,n}^2(\omega)\right) + 2Q_D hc \lambda e^2 P_D}} \frac{ds}{dz} \quad (3.10)$$

Where S_z is the power spectral density of the displacement signal. The maximum signal to noise ratio at a given input power is independent of eccentricity, and it is reached when the spot size matches the cantilever length. The exact value of the incoming beam width that satisfies this condition depends on the length of the cantilever, refractive index of the medium, the objective focal length, wavelength of the light, and eccentricity. The maximum attainable value of $ds / (dz * w_{out})$ is $2n / 1.22\lambda$, independent of focal length or cantilever size, provided that the numerical aperture of the objective is sufficient to form a diffraction limited spot no larger than the cantilever. If in addition, the shot noise dominates all other noise sources, the minimum noise floor in a position measurement with an optical beam deflection setup is:

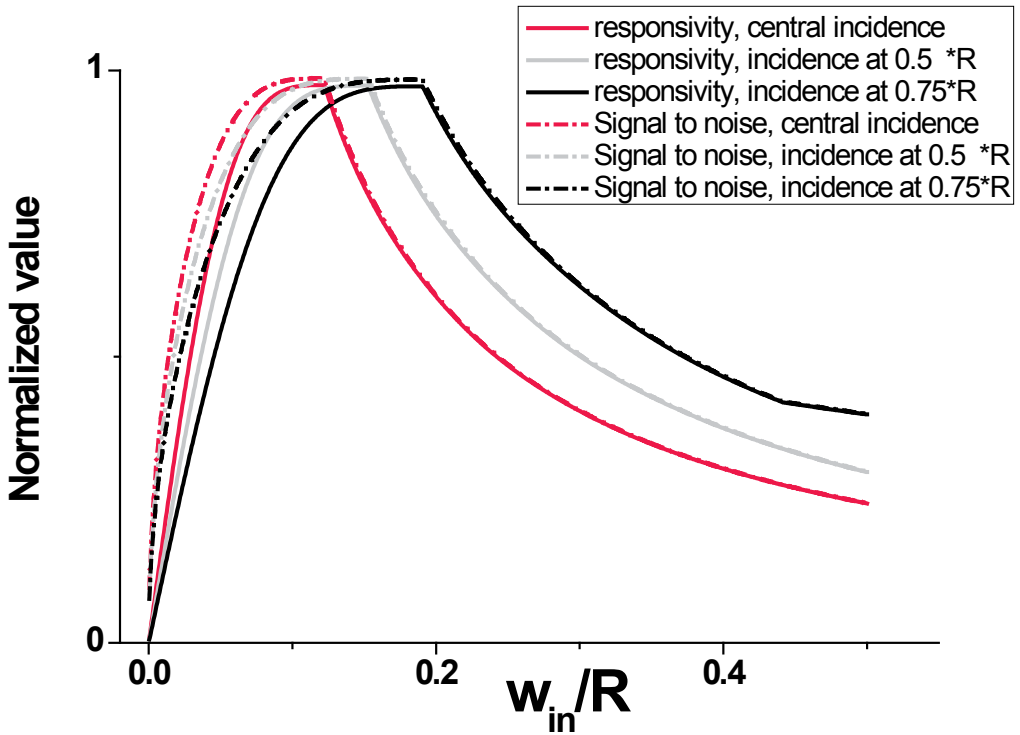


Figure 3.7 Signal and signal-to-shot-noise ratio as a function of incoming beam width (relative to lens radius) for different eccentricity

Normalized responsivity (solid lines) and corresponding normalized signal to shot noise ratio (dashed) for a beam incident on an NA=0.7 objective, and a cantilever 20 times as long as the laser wavelength. Three sets of curves are shown: beam incident at the center of the lens (red), at 50 percent of the radius (grey), or 75 % (black). At low widths of the incoming beam, part of the light spills over the cantilever. The signal increases linearly with the reflected power, the SNR increases with the square root of the power. When the spot is fully reflected (upward from $w_{in} = 0.1$ to 0.2, depending on eccentricity), power is constant and the decrease of the relative shift lowers the responsivity. Eccentricity has an effect on the spot size and hence on the signal and noise. Incoming laser power is assumed to be the same for all curves.

$$S_{z,\min} = \frac{n}{1.22C_g} \sqrt{\frac{hc\lambda}{8QP_D}} \quad (3.11)$$

For realistic values of $n = 1$, $\lambda = 780 \text{ nm}$, $Q_D = 0.9$, a Gaussian beam and 1 mW of total reflected laser power, this amounts to $6.7 \text{ fm}/\sqrt{\text{Hz}}$.

A number of remarks have to be made regarding the practical application of equation (3.10). Firstly, the optical path was assumed to be ideal. In practice, aberrations of the focusing system, bending of the cantilever and corrugations on the cantilever's reflecting surface will lead to a

larger spot size than that limited by diffraction only. Not only the width, but also the shape of the spot may change, leading to much lower C_g values. This last problem may be tackled with the use of a detector with more than 2 sections [88].

Secondly, when the ratio of focal distance to cantilever length is very high, a very narrow input beam is required for optimal sensitivity. With long cantilevers or short focal distances, diffraction in the beam path from the lens to the detector may start to become significant. In a paraxial approximation, the width of the beam on the detector depends on the detector distance D_D as $w_D = w_{out} + D_D * F/L$. With e.g. a 10mm focal distance, a 200 μm cantilever, and 780 nm laser light, the beam will have doubled its width already at a detector distance of 4 mm, while a 20 mm focal distance lens on a 20 μm cantilever will need 0.8 m for this.

Thirdly, the assumption of shot noise being the only source of noise is often made, but at low frequencies, such as used in contact mode AFM, amplifier voltage and (in some cases) current noise show a $1/f$ character, and easily dominate the shot noise. For large bandwidth systems, the amplifier voltage noise is strongly amplified by amplifier and diode capacitance, so care should be taken in selecting the components. On top of this, fluctuations in the laser power or pointing direction will add to the noise. Although it is possible to cancel out the influence of power fluctuations by dividing the difference signal of the diodes by the sum signal, division is difficult to implement in analog electronics without introducing significant amounts of noise. Therefore, laser power must be strictly controlled.

AFM cantilevers can have length to width ratios of up to 10. In order not to lose a large amount of laser power by adjusting the laser spot size to fit the length, an elongated incoming beam (elongated perpendicularly to the long axis of the cantilever) should be used. The size of the spot in the perpendicular direction has no influence on the signal to noise, as long as no power is spilled over the edges. Shaping the laser beam should preferably be done with lenses or prisms, since using an aperture reduces the total power.

Summarizing, we can give the following design rules to optimize signal to noise for an optical beam deflection setup for miniature cantilevers:

1. Adjust the width of the incoming beam to have a spot size equal to the cantilever length
2. Maximize the laser power
3. Use the smallest wavelength possible
4. Minimize electronic noise and laser noise
5. Use high quality, high NA optics to focus all the light on the cantilever and minimize aberrations

6. Use long focal distance optics and short detector-to-lens distance to minimize diffraction in the outgoing path
7. In case of a distorted beam profile: use an array detector

3.2.2 A versatile optical beam deflection detection system based on commercially available optical components

A schematic drawing of a setup that was realized with the design rules of the previous paragraph in mind is depicted in figure 3.8. This setup was designed to be used with different sizes of cantilevers, and is made such that each component can be easily replaced. With exception of the photodetector, it consists entirely of commercially available optical components and is built up on a 90 x 120 cm breadboard.

A 25 mW, 780 nm laser diode (Sanyo, DL4140-201S) is mounted in a holder with a thermo-electric cooling element for temperature control (Thorlabs TCLDM9). 780nm was chosen because smaller wavelengths may cause damage to samples or interfere with simultaneous fluorescence measurements. Laser current is supplied by a low-noise current source (Lightstar LD2000), and temperature is controlled by a Seastar Optics TC-5100. The temperature control minimizes mode hopping and increases the pointing stability of the laser. Collimating the output of the diode is done using a high-quality anti-reflection coated molded aspheric lens (Thorlabs C240TM-B). A miniature Faraday-rotation type optical isolator (Optics For Research IO-D-780) is used to prevent back reflections of laser light into the diode. Such back reflections cause laser feedback, which is a source of large power fluctuations. The laser beam is not collimated at the output of lens 1, but actually focused at the isolator, and then recollimated by lens 4. This lens can easily be interchanged to alter the beam size. A polarizing beamsplitter / quarter wave plate (CVI laser) combination is used to separate the incoming and outgoing beams. By placing a half wave plate (Thorlabs) in the path between the isolator and the beam splitter, laser power incident on the cantilever can be adjusted. An anamorphic prism pair (CVI laser AP-3X-10.0-780-UNP) is used to expand the beam by a factor 3 in one direction. Since the diode laser outputs an elliptical beam with approximately 3:1 aspect ratio, the aspect ratio of the beam on the lens is approximately 9:1. The AFM and cantilever are mounted on an inverted microscope (Zeiss Axiovert 200). A dichroic mirror (CVI laser SWP-45-RUNP-780-TUNP-633) separates the laser path from the viewing optics of the microscope, but a small fraction of the laser light is still transmitted. The microscope viewing system can then not only be used to visualize the sample, but also to assist in aligning the laser on the cantilever. The focusing element is interchangeable. Microscope objectives such as the Carl Zeiss W-PLAN-APO 63/0.95 (2mm working distance water immersion objective with 0.95 numerical aperture) can be used, but also long working distance aspheric lenses such as the C240TM-B from Thorlabs (8mm EFL, NA 0.5, molded glass), or the Asphericon 25-20 HPX-B (20 mm EFL, NA 0.56, precision machined). The reflected light follows the same path back up to

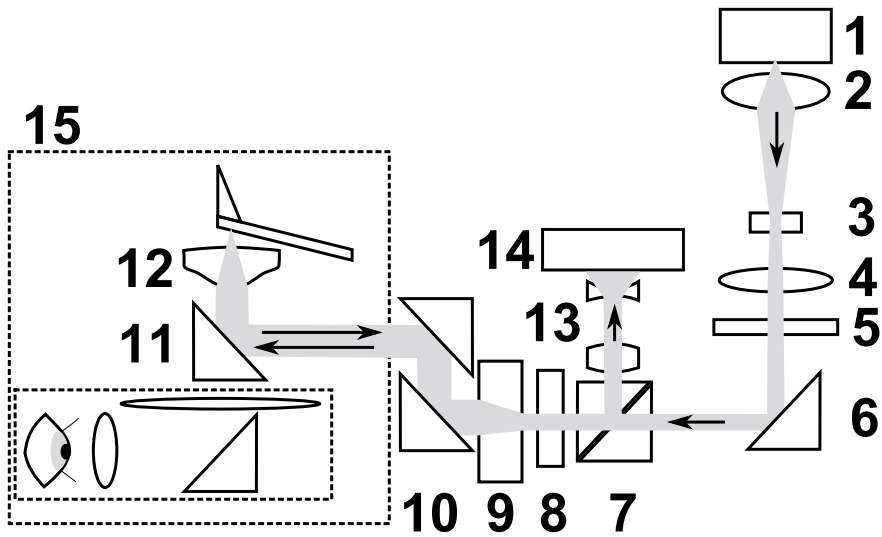


Figure 3.8 Optical beam deflection detection setup

Legend: 1) TE cooled 780 nm 25 mW laser diode 2) Collimating aspheric lens 3) Optical isolator 4) Interchangeable collimating lens 5) Half wave plate 6) Steering mirror 7) Polarizing beam splitter 8) Quarter wave plate 9) Anamorphic prism pair 10) Periscope assembly 11) Dichroic mirror, short wave pass 750 nm 12) Focusing lens, interchangeable 13) Beam shaping cylindrical lenses 14) Photodiode array detector 15) Inverted microscope

the polarizing beamsplitter, where it is directed towards the detector. The detector is based on a linear array of 16 photodiodes (Hamamatsu S8558). Such an array allows for an optimal signal to noise even for distorted beam shapes. Two cylindrical lenses shape the beam to optimally fit on the detector.

This system can be used to monitor angular deflection of miniature cantilevers with very high sensitivity (see below), but when the beam is pointed such that it is under an angle with the optical axis and off-center in the objective, displacements of large and small objects parallel to the optical axis can be measured. The optical responsivity is much lower in this case, but can reach up to 1 mV/nm, with the same bandwidth as the cantilever detection. Any object that can be placed on top of the microscope with a reflecting surface facing the objective can be measured. An example is given in paragraph 4.3 .

3.2.3 A high bandwidth, low noise array detector for AFM

When cantilevers are diminished in size down to only a few wavelengths of the light used to detect their displacement, small irregularities on the surface can lead to large distortion of the optical wavefront. This may lead to beam shapes on the detector that have a very low intensity around the center, which lowers the sensitivity. As was shown by Schaeffer *et al* [88,89], the use of a detector with more than 2 sections in the direction of interest can significantly increase the signal-to-noise ratio, as well as widen the linear range of the sensor. These improvements can be reached by weighing the output of each of the diodes before adding them. The optimal weight factors depend on the beam shape. To fully benefit from the increase of signal-to-noise, the added noise that is introduced by using more amplifiers needs to be kept to a minimum.

The most important decision when designing a photodiode amplifier is the choice of the op-amp used in the first amplification stage, and the gain to be used in this stage. The gain determines the maximum laser power that can be used, as well as the amount of thermal current noise coming from the feedback resistor and the relative importance of the amplifier's input voltage noise. At gains above a few kV/A, the amplifier's current noise is often the dominating noise source. An exception is formed by low noise FET-input operational amplifiers. Of currently available op-amps, the Texas Instruments OPA 657 has the best combination of input current noise (1.3 fA/ $\sqrt{\text{Hz}}$), voltage noise (4.5 nV/ $\sqrt{\text{Hz}}$), and gain-bandwidth product (1.6 GHz) for use in MHz bandwidth photodiode amplifiers. Bandwidth of the amplifier is also determined by the RC circuit in the feedback. Stray capacitance in the feedback resistor and in the leads on the printed circuit board limit the capacitance to a minimum of about 0.2 pF. A $7 \cdot 10^4 \Omega$ resistor then leads to a 10 MHz -3dB bandwidth. A lower resistor value would increase both bandwidth and maximum useable laser power, but when the amount of reflected light is low, amplifier noise is most critical. Therefore, a 69 k Ω resistor is chosen. Together with the 3.5 V maximum output of the amplifier and the 0.57 A/W responsivity of the photodiode, this choice limits the incoming power to 90 μW per diode or 1.4 mW in total.

The output of the transimpedance amplifiers is buffered and sent to a summing module. This module has one amplifier per channel, with a gain that is set by the user with a potentiometer knob and polarity (+, - or 0) switch on the front panel. The gain can be varied between +3 and -3. Output of all 16 amplified channels is summed, and this weighted signal, the equivalent of the difference signal in conventional AFM detectors, is output to a front panel connector. Optimizing signal to noise can be performed by oscillating the cantilever, measuring AC and DC signal levels from each channel individually, calculating the optimal gain levels from these measurements, and turning all potentiometers to the desired value. Unfortunately, the determination and setting of optimal gain factors is very elaborate. An automated approach for setting gain factors could greatly enhance the user-friendliness of the array detector. As an alternative, a much more coarse

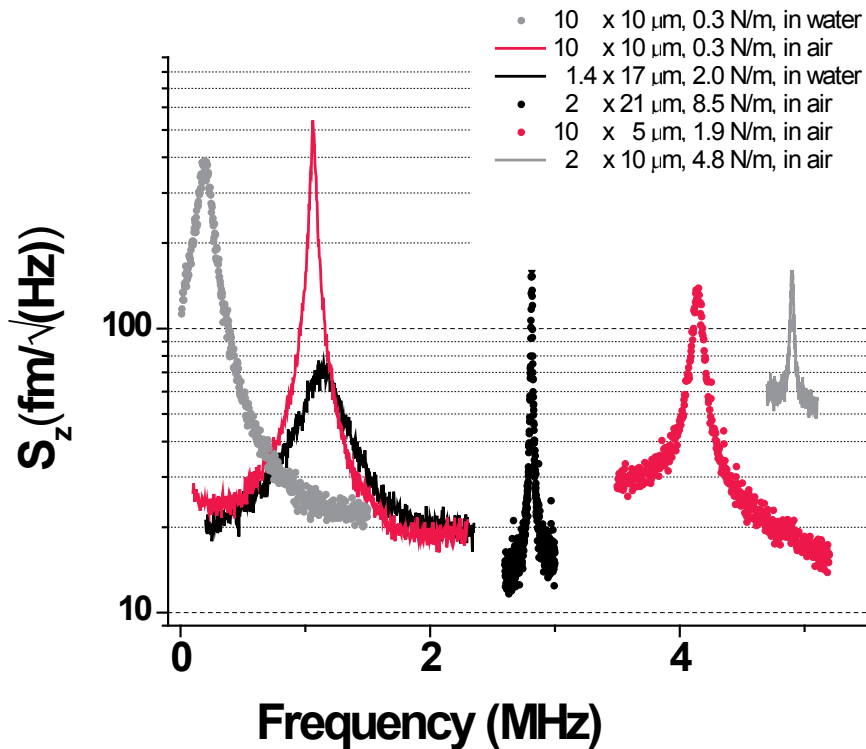


Figure 3.9 Experimentally measured thermal spectra of several miniature cantilevers

These six spectra from five different cantilevers illustrate the practical sensitivity limits of the OBD system. Noise floors are between 15 and 50 fm/√Hz. The higher noise floor of the 2x10 μm cantilever is mainly due to the low amount of light reflected from this thin, uncoated cantilever.

method is to use only the polarity switches, aided by an LED bar graph beam profile monitor that gives a quick visual indication of the light level of each diode segment. All diodes with a light level below a threshold value can be switched off (polarity 0). The other diodes can be switched in polarity one by one, keeping the polarity that increases the AC signal. With asymmetric beam profiles, optimal sensitivity is not necessarily attained when the DC difference signal is 0.

3.2.4 Detector performance

The performance of the optical detection system is demonstrated in figure 3.9. The thermal spectra of a number of small cantilevers are displayed there, showing the large bandwidth (>5 MHz) and low noise of the system. Spectra were measured by connecting the output of the summing module to an Anritsu MS2651B spectrum analyzer, controlled via a GPIB interface by LabView software (National Instruments). Converting the voltage spectral density to motion spectral density was done using an implementation of the Higgins-Sader method [90]. This method is

developed for cantilevers with large length-to-width aspect ratios, and some systematic error may be present in the scaling of the 10x10 and especially the 10x5 μm cantilevers. Nevertheless, the Sader Plan view method has been shown to be quite robust against low aspect ratios [63], and it is the most convenient non-contact method of determining the spring constant. Measurements performed in fluids of different viscosities can be used to eliminate the systematic error.

As can be seen in figure 3.9, noise levels below 20 $\text{fm}/\sqrt{\text{Hz}}$ are obtained even on very narrow cantilevers, both in air and in liquid. Thermally limited detection at 5 MHz is attained even on a relatively stiff (4.8 N/m) cantilever made of badly reflecting, uncoated silicon nitride. The long laser path and imperfections in the optics (especially astigmatism) limit the beam diameter at the objective to a minimum of approximately 2mm. To optimally make use of *standard* cantilevers in this system, long focal distance, low NA lenses should therefore be used. This was not attempted, so the sensitivity on larger cantilevers is worse. The more so, because at low frequencies (< 50 kHz) $1/f$ noise is an important factor, and the electronic noise floor increases. The lowest noise floor attained with a 160 μm long cantilever was 66 $\text{fm}/\sqrt{\text{Hz}}$ at 367 kHz (data not shown).

4 Design and performance evaluation of a miniature cantilever AFM scanner

4.1 Scanner and coarse approach

This paragraph describes the design of a compact scanner assembly for atomic force microscopy. Goal of this design was to achieve a high resonance frequency scanner suitable for high speed scanning in liquid with feedback enabled. Furthermore, two electronic modules were developed to adapt the signal from the beam deflection measurement set-up to make it suitable for feedback in different situations. For the high-speed detection of the cantilever amplitude in Amplitude Modulation AFM, a sampling peak-detector is presented that can measure the amplitude within a single oscillation. For force-volume measurements, a complete feedback system based on a combination of time-lag and emergency feedback actions was developed. The working of all these developments is illustrated with a number of examples.

4.1.1 Scanner design

A sample scanning design was chosen for this AFM. Scanning the tip is possible as well, but this causes difficulties in the alignment of the optics used for the position detection. To minimize the mass of the total scanned structure, the sample is mounted as closely as possible on top of the scanning piezo. Because the microscope is also operated in conductive liquids, the scanning piezo's electrode surfaces must be well-isolated from the environment. Furthermore, to prevent contamination, all surfaces in contact with the liquid must be chemically inert. A number of different actuator geometries were tested: a homemade piezo stack similar to that described in a paper by Rost *et al* [91], a commercial piezo stack (PI 123.01, Physik Instrumente GmbH), and an adapted commercial piezo tube (Staveley EBL 2, 1/2" x 1/4" tube shortened to 9 mm height). Although high resonance frequencies could be obtained with the piezo stacks, the geometry of the tube was more suited for creating a scanner assembly for operation in liquid. After the wires were attached to the piezo tube, it was covered in nail polish (Max Factor) for insulation. Several insulating agents were tested, but the nail polish was best at covering the sharp edges of the wires, which were the most problematic areas. The top of the tube was covered with an anodized aluminum plate, which was grounded to reduce electrostatic forces on the cantilever due to the scanning voltages. Samples can be attached directly to this plate, but it is difficult to clean the whole scanner thoroughly after use. Therefore, PEEK sample holders were made, that screw tightly onto the scanner top plate. These sample holders make it easier to handle thin small samples, and reduce contact of the scanner with the liquid during scanning. Nevertheless,

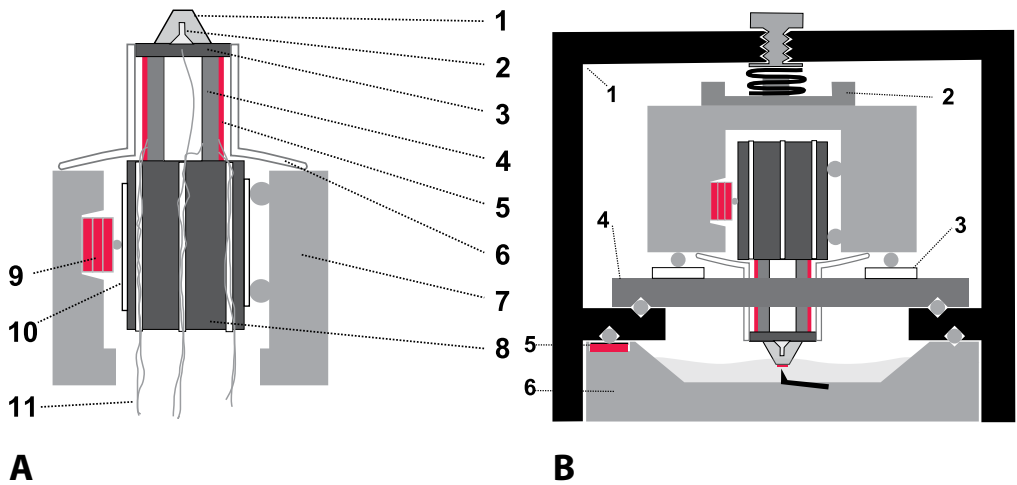


Figure 4.1 Scanner and coarse approach design

A: Scanner and z-approach Legend: **1**) Sample holder, PEEK **2**) Sample holder screw, stainless steel **3**) Ground plate, anodized aluminum **4**) Piezo tube **5**) Nail polish insulation **6**) Flexible silicone protection jacket **7**) Approach motor housing, aluminum **8**) Motor slider block, Invar steel **9**) Shearmode piezo motor actuator **10**) Motor slide plates, glass **11**) Scan voltage wiring. **B:** Complete assembly. Legend: **1**) Outer body, anodized aluminum **2**) Slider assembly, PTFE **3**) Coarse XY motion slide planes, glass **4**) Supporting bridge, anodized aluminum **5**) Cantilever excitation piezo **6**) Tip holder

spilled liquids can easily wet the scanner. To protect the scanner from this, a silicone jacket was fabricated to fit around the tube.

The piezo tube is mounted on an invar steel block, that serves as the slider of the coarse approach motor. This motor is a stick-slip piezo motor, which uses a homemade stack of shearmode piezos as the actuator. To provide a smooth hard surface for the hardened steel balls of the motor to slide over, glass plates are glued into V-grooves in the slider block. The piezo wires are protected by leading them through holes in the slider block.

The scan tube and motor housing are placed upside-down in a housing that sits on top of the inverted microscope which is part of the beam deflection setup described in paragraph 3.2.3 and figure 3.8. The motor housing rests on three balls, that can slide over glass plates to position the sample over the tip. This positioning is done by hand, and is therefore quite coarse. The glass plates are glued onto a bridge that is attached to the AFM outer body. A slider assembly, consisting of a PTFE slider, a spring and a screw, can be used to adjust the pressure with which the motor housing is pressed down. When the scanner is in the desired position, the spring is compressed and the motor housing is locked firmly into place. The tip holder can be clicked

with three grooves on to three balls that are attached to the AFM outer body, and is kept in place by strong magnets. One of the grooves in the tip holder is supported by a piezo, that is used for excitation of the cantilever.

The tip holder is made of Zerodur glass ceramic (Schott) and Invar steel. A PEEK ring separates the steel parts from the liquid bath. The top and bottom of the central Zerodur part are precision polished for low distortion of the optical wavefront. The cantilever sits in a groove in the Zerodur part, which is ground under an angle of 13 degrees with respect to the top face. Two grooves perpendicular to the cantilever groove serve as guides for a liquid flow. The liquid can be deposited in the tip holder before scanning, but it is also possible to flow liquid through the holder while scanning. Pumping equipment can be attached to the tip holder through standard 1 mm PTFE tubing.

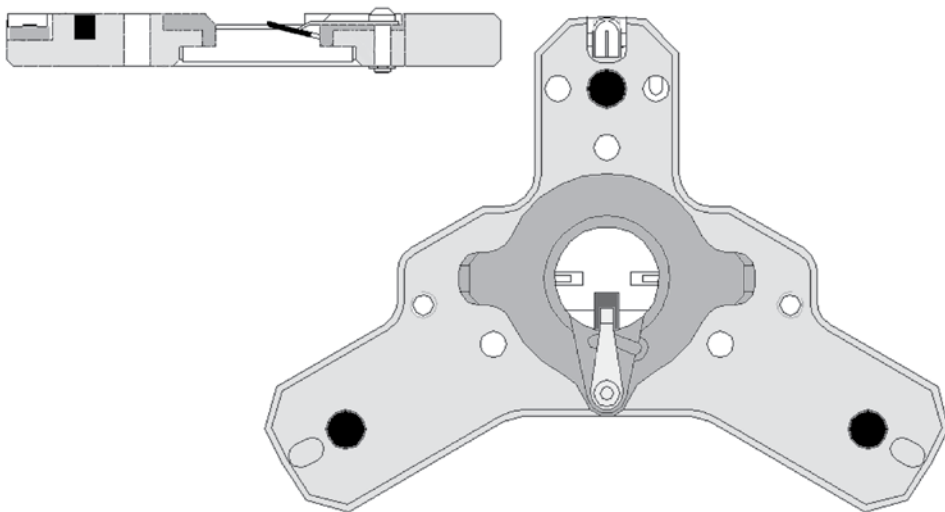


Figure 4.2 Tip holder

The tip holder body (light grey) is held to the rest of the AFM by three magnets (black). The cantilever (black) is held by a stainless steel spring (lightest grey) onto a Zerodur window, that serves as the bottom of the liquid cell. A PEEK ring (dark grey) protects the liquid and the steel body from each other. In the cross section (taken along the vertical center line) the piezo underneath the top anchor point is depicted in dark grey.

4.2 Control and feedback electronics

Data acquisition, scan control and feedback of the AFM were performed with an LPM Camera system (Leiden Probe Microscopy B.V.). A detailed description of this controller can be found in reference [91]. This system was developed for STM imaging applications, therefore a number of adjustments to, or replacements for, electronic modules had to be made. Two major developments were the realization of a high speed amplitude detector for Amplitude Modulation AFM (AM-AFM), and a special feedback for three-dimensional measurements.

4.2.1 High speed amplitude detector

Most dynamic AFM methods rely directly or indirectly on a measurement of the oscillation amplitude of the cantilever. The most commonly used device to measure the oscillation amplitude in AM-AFM is a lock-in amplifier. The output stage of a lock-in amplifier contains a low-pass filter, which determines the bandwidth of the output signal. Low-pass filtering is used to suppress noise and spurious signals outside the band of interest, but is also necessary to suppress strong variations of the output signal at twice the oscillation frequency, which are produced in the lock-in measurement process. If the desired bandwidth of the amplitude measurement is close to the oscillation frequency, as is the case for high-speed dynamic AFM with low quality-factor cantilevers, using a lock-in is problematic. A method to measure amplitude in AFM with a bandwidth of twice the oscillation frequency was proposed and implemented by Ando [46]. We use a similar method, that is represented graphically in figure 4.3. Apart from the high bandwidth, an additional advantage of this detection method is that the correct peak-to-peak amplitude is still measured when the oscillation deviates from a sine shape.

The deflection signal from the photodetector is amplified and differentiated. The zero-crossings of the differentiated signal correspond in time with the top and bottom of the input signal. The difference between the value of the input signal at consecutive zero crossings therefore corresponds to the peak-to-peak amplitude of the signal. The top and bottom values are also available separately, which can be useful in recognition imaging [92]. To compensate the propagation delays in the path between the input and the pulse generation, the user can delay the signal before it is sampled. The user can also set a window to ignore zero crossings of the differentiated signal far away from the peak positions expected for the input. This significantly reduces the noise in the output. The window size can be increased to the entire period if no windowing action is desired.

The noise analysis of the peak detection scheme is not straightforward, so only a qualitative analysis is presented here. Although the sampling action is a very non-linear operation, its noise propagation can be understood in terms of aliasing in analog-to-digital converters. Below the

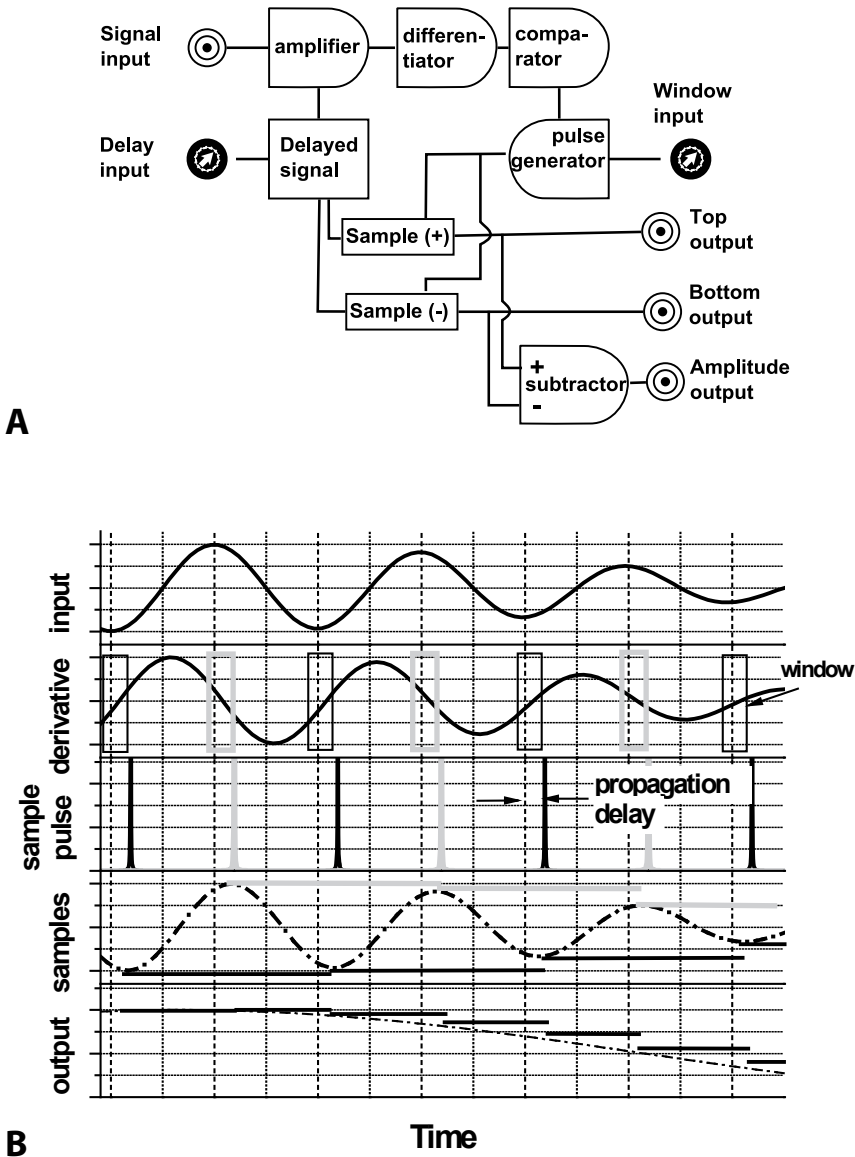


Figure 4.3 Schematic representation and time diagram of the peak detection amplitude converter

A: Schematic representation. The signal from the deflection detection system is amplified and split into two channels. One channel is differentiated and the zero-crossings of this signals trigger two sample-and-holds to capture the positive and negative peaks of the other channel. This channel is simply a delayed version of the amplified input. The two sampled signals are available individually, subtracted as an amplitude signal. **B:** Timeline representation of the sampling process with a sine of decaying amplitude as the input signal.

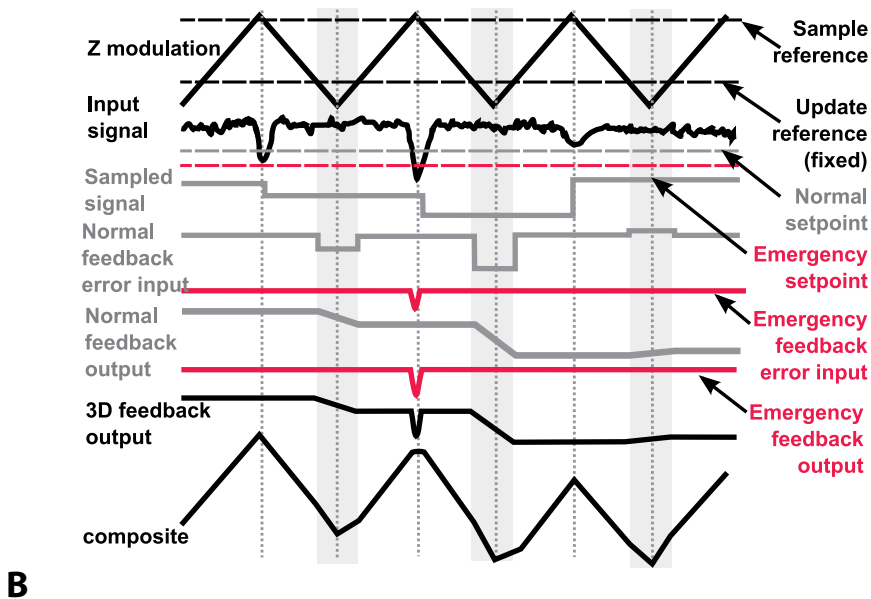
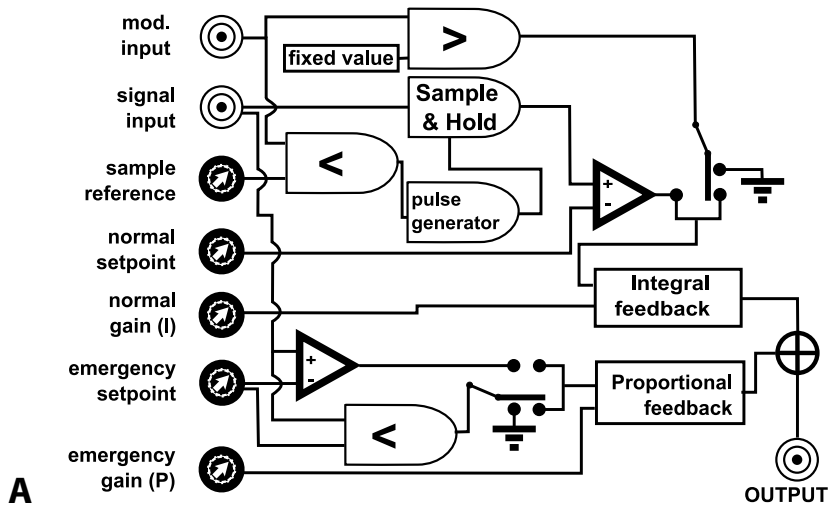


Figure 4.4 Schematic and time diagram of 3D feedback

A: Schematic representation. The signal is sampled at a point close to the surface (sample reference), and the setpoint for the normal feedback is subtracted from the sampled value. Only when the tip is far away from the surface, this difference is supplied to the input of the normal (integral) gain. The emergency setpoint is continuously compared to the signal, but only supplied to the emergency (proportional) feedback if this difference is negative. **B:** Resulting signals at different points in the feedback in a typical measurement situation. The signal amplitudes are not to scale.

oscillation frequency ω_d of the cantilever, which is the Nyquist frequency of the sampling, noise at a frequency ω_n in the deflection signal is directly transferred to the output signal. Higher frequency noise is also detected, but will appear at a frequency $\omega_{o,n} = \omega_d - \omega_n \bmod \omega_d$. So in principle, the noise bandwidth of this peak detection scheme is infinite. Although in practice finite values of component bandwidths will limit the noise bandwidth, low-pass filtering of the input signal at the maximum desired signal bandwidth of 10 MHz is applied in our implementation. Low-pass filtering of the output signal cannot eliminate high-frequency noise in the input. If we can assume that none of the noise is phase-coherent with the cantilever oscillation, the noises in the top and bottom signals are independent, and the signal-to-noise ratio of the subtracted amplitude output is $\sqrt{2}$ higher than that of the individual signals.

The noise in the input signal will not only appear at the sampled output, but also influence the sampling process itself. Noise in the differentiated input signal will lead to false zero crossing detections, and hence to noise in the position of the sample pulse and an underestimation of the amplitude. The exact value of this underestimation depends on a complex interplay between the shape and amplitude of the oscillation, the settings of the window, the frequency of the noise component that leads to the false zero crossing and the width of the sample pulse. Using a narrow window greatly reduces the influence of false zero crossings. The trade-off is that this limits the correct detection of peaks of oscillations with a shape that is not constant over time, such as occur when scanning on a sample with inhomogeneous adhesion properties.

4.2.2 Three-dimensional feedback system based on sample and hold action

The AFM is not just a tool for imaging or for measuring force profiles. These two functions can be combined. By making an approach-retract cycle at each point in a grid over a surface, a three-dimensional scan volume is defined. During this three-dimensional scanning, the cantilever deflection can be recorded continuously, a technique that is usually called force-volume imaging [93,94]. The sheer amount of data that is produced by recording one force curve for each image pixel limits the resolution and scan speed of this technique on most commercially available AFM systems. For this reason, several methods have been developed for online extraction of information from the force curve, storing only a few values per curve. These techniques are known as adhesion imaging [95], pulsed force mode [96], or jumping mode [97]. Imaging feedback such as is used in two-dimensional scanning cannot be used in 3D, since for a considerable portion of the imaging time the tip is not in contact with the sample. Usually, 3D scanning techniques employ a trigger strategy to control the maximum force applied to the sample: instead of scanning a fixed distance in the z-direction, the tip is lowered until a setpoint force is detected. This detection triggers the reversal of the scan direction.

Most commonly, force-volume and related imaging methods use the deflection of the cantilever as the measurement variable. Only few examples exist of three-dimensional scanning with dynamic techniques such as force modulation [98], or frequency modulation AFM [28].

The high data acquisition speed of the Camera SPM control electronics enables the acquisition of force-volume images at speeds and with resolutions comparable to present-day two-dimensional image acquisition. For example, a 512 x 512 pixel, 1024 total points per force curve image can be acquired within 80 seconds. A disadvantage of the Camera system is that its completely analog scan generation is not easily made compatible with triggering. Therefore, a time-lapse feedback module was developed for the Camera system. This module replaces the PI regulator that is used in two-dimensional scanning, and can be used with any SPM signal at the input, including deflection, current and amplitude. The main function of this feedback is to compare a setpoint to the SPM signal measured at close approach to the sample, and when the tip is far away from the sample, regulate average tip-sample distance accordingly.

A schematic drawing of the 3D feedback is depicted in figure 4.4, along with a time diagram that illustrates its working principle. The 3D feedback consists of two feedback units. During normal operation, only one feedback unit is active. This is a delayed action integral feedback, whose gain can be regulated by the user. The error signal that this feedback works on, is nonzero only when the tip is far away from the surface. This is achieved by switching the input of the feedback to ground whenever the modulation input is more than -7.5 V. This value can only be changed by opening the module and adjusting a trimpot on the printed circuit board. When the feedback is active, its error signal is a difference between a user-defined setpoint and a previously sampled value of the input SPM signal. At what value of the modulation input the sample is taken, can be set by the user.

This scheme allows the average height of the tip to be adjusted when the tip is far from the surface, thus regulating the height without interfering in the force-distance measurement. However, the regulation is always delayed with respect to the measurements, so when large height differences occur between two consecutive curves, the tip-sample interaction may become larger than acceptable. In this case, the second feedback loop (the emergency feedback) can be used.

The emergency feedback is a conditional proportional gain feedback. Whenever the SPM input signal crosses the emergency threshold, this feedback loop becomes active, and adds an additional signal to the piezo-voltage governing the approach to prevent the tip from further approaching to the sample. This action influences the shape of the ramp close to the sample, and should be avoided as much as possible. Emergency actions can be prevented by keeping the

distances between consecutive force curves small, by taking great care on the initial approach and tuning of the normal gain setting.

When switching to the 3D mode in the Camera software, the high-speed analog scan generator (X-generator) serves as the generator of the Z scan signal (Z-modulation). It has to be connected to the Z piezo driver via an additional mixer. The role of the X-generator is taken over by the sample voltage generator. The additional mixer attenuates the +/- 10 V signal from the generator to obtain the desired scan size in Z. The second output of the generator is used to trigger the 3D feedback. The output of the feedback is connected to the second input of the additional mixer, so that the composite signal at the bottom of figure 4.4B is obtained. This signal is connected to the Z-piezo driver, and used as an input for the data acquisition.

4.3 Scanner characterization

The scanner described in paragraph 4.1.1 was characterized by measuring its response to a sinusoidal excitation with a lock-in amplifier (Signal Recovery 7280). During the measurement, only one of the electrodes of the scan tube was excited, and the other electrodes were grounded. The response was measured by either monitoring the current through a 500 Ohm series resistor, or by using the optical setup described in chapter 3. For the optical measurements, the laser was reflected from a tiny mirror (an AFM cantilever chip), that was attached to the scanner top plate with a bit of Apiezon T grease. The results are shown in figure 4.5. The first scan tube resonances are found around 22.5 kHz, and correspond to the X and Y bending modes of the scanner. The laser is sensitive mainly to displacement in the Z direction in the way it was used in this measurement (off-axis, angled entrance into the objective, out of focus), but to a lesser extent also to bending in the X direction. This explains the different phase behavior for the excitation of X and Y directions. Resonances with a strong response in the Z direction are found at 39.5 and 55.4 kHz. At much lower frequencies, between 1 and 10 kHz, there are small peaks in the response that have strong X and Y phase changes associated with them. By clamping the slider block and housing, or only the slider block in a vice in different configurations, these resonances could be identified as resonances of the slider block, the motor housing and other parts of the AFM set-up.

Because of their limited phase lag, the resonances of the mechanical structure lead to image artifacts, but not necessarily to feedback instability. This is demonstrated in figure 4.6, where high-speed scans of DNA on mica are shown. An oscillation with a frequency of 1.5 kHz strongly distorts the image, but is only barely visible in the error signal (vertical bands about $\frac{1}{4}$ image wide). The faster oscillation induced by the turnaround of the piezo on the other hand has only

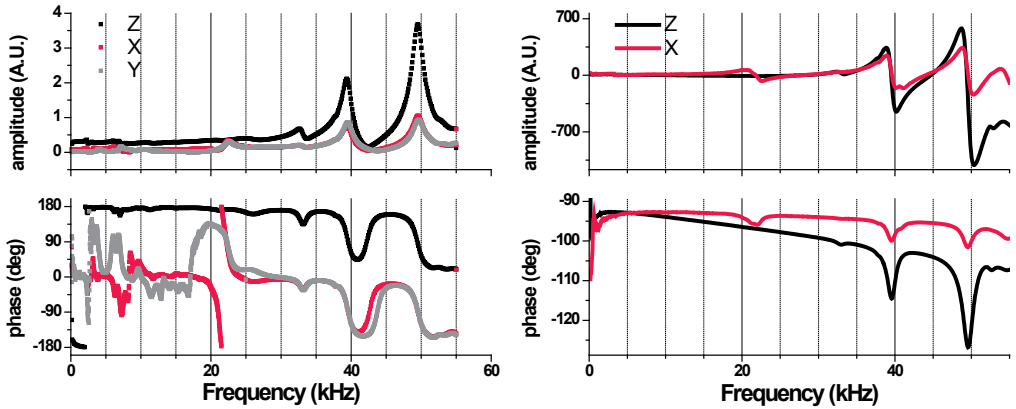


Figure 4.5 Scanner resonances measured optically and electrically

Left optical beam deflection measurement of scanner response. The optical method is most sensitive to z response, but also to tilting in the x-direction. Only z and x were measured electrically; to correct for capacitive current a straight line was subtracted from the electrically measured amplitudes and the z-amplitude was divided by 4. Resonances are found at 22.4 kHz for x, 22.6 kHz for y, and 39.4 and 49.5 kHz in z. An increased response at 32.6 kHz is also present, but the phase shift is small for all directions. Many low-frequency resonances of low amplitude are present in the optical signal, especially in the x and y directions. They are ascribed to resonances of the z-slider block and the motor housing. Confirmation of this was found by measuring the response when the slider was solidly clamped in a vice (data not shown). The low-frequency resonances cannot be distinguished in the electrical response, which is much less sensitive to resonances other than piezo resonances.

limited amplitude, but gives very large oscillations in the error signal (narrow vertical bands in the left half of the image). A high feature on the bottom right-hand side of the image induces oscillations of the same frequency as the turnaround. These images were acquired with a different scanner than the one that produced the resonance curves of figure 4.5, which is why the oscillation frequency is not 22.5, but 27 kHz. The cantilever may also play a role in the closed-loop feedback response time. Far away from the surface, the cantilever used for these scans has a resonance frequency of 1685 kHz and a quality factor of 132. The response time of such a cantilever is $2Q_c/\omega_c = 2.5 \mu\text{s}$, which is close to the period of the piezo oscillations. However, the rather large amplitude reduction of 50% used in this measurement may considerably decrease the response time because of surface damping, as was found in measurements and simulations by Kokavecz *et al* [99].

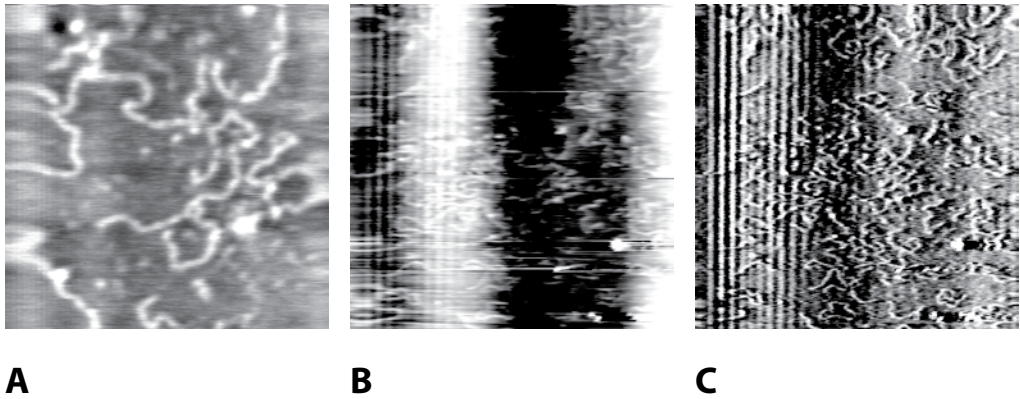


Figure 4.6 High speed scanning in air on a DNA sample

Sample: 1kb lambda phage DNA on mica that was modified with polylysine before deposition of the DNA. Scanned in intermittent contact mode (amplitude detection with the peak detector described in 4.2.1 with a $2 \times 20 \mu\text{m}$ cantilever that had a resonance frequency of 1.685 MHz and quality factor of 132. Environment: air at room temperature **A:** Height image at 240 lines per second (2 s/frame), 480 nm scan size, 1.12 nm total height scale **B:** Height image at 500 lines per second (1s/frame), $1.2 \mu\text{m}$ scan size, 1.33 nm total scale. **C:** Amplitude (error) image of the scan in B). The images are distorted by the resonances of the scanner. Image distortion is only small for the 240 lines per second image. In the faster image, that also has larger scan size and thus more excitation of non-piezo resonances the distortion amplitude is over 1 nm. The feedback can follow the slow oscillations induced by the resonances of the mechanical structure, but large amplitude variations occur after the turnaround as a result of piezo resonances.

A test of the high-speed performance of the scanner on samples with large surface corrugation was performed in contact mode. When scanning fast on samples with a large corrugation, large error signals can be expected. When using intermittent contact mode, the error signal is linear in the surface corrugation in a range that is always smaller than the oscillation amplitude, but in contact mode scanning the linearity is usually only limited by the detector. A standard silicon nitride triangular contact mode cantilever was used (Digital Instruments, NP, long, wide cantilever), and the sample was a thin film of gold on mica that had been exposed to the ambient environment for several days. The sample was contaminated with many dust particles with sizes of 10-100 nm. The image in figure 4.7 demonstrates that tip speeds of 1.2 mm per second in the vertical direction are possible.

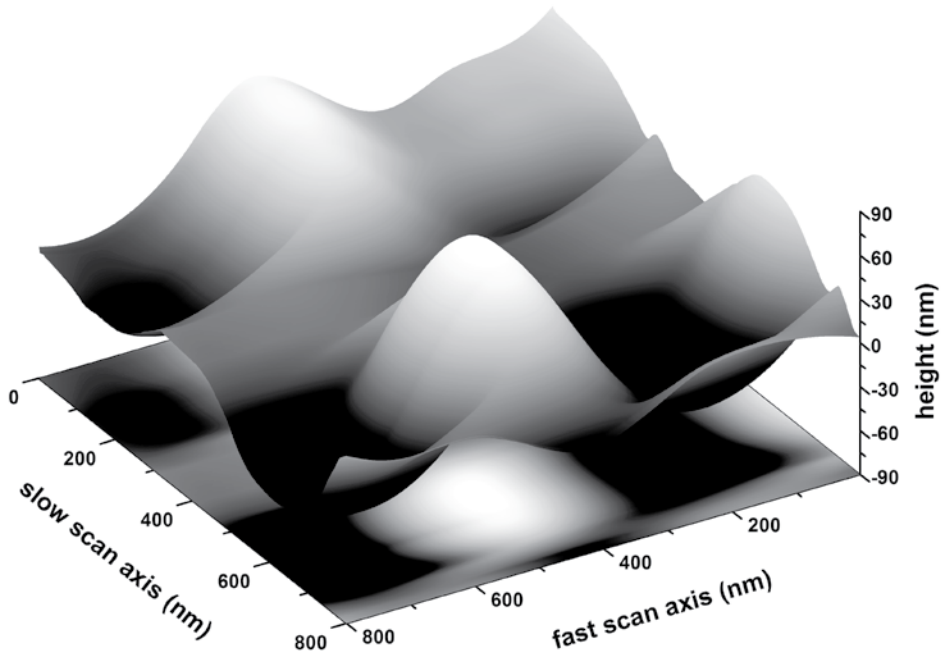
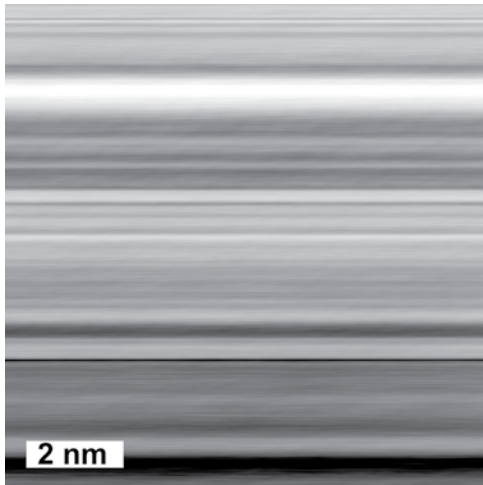


Figure 4.7 High speed scan with 1.2 mm/s vertical tip speed

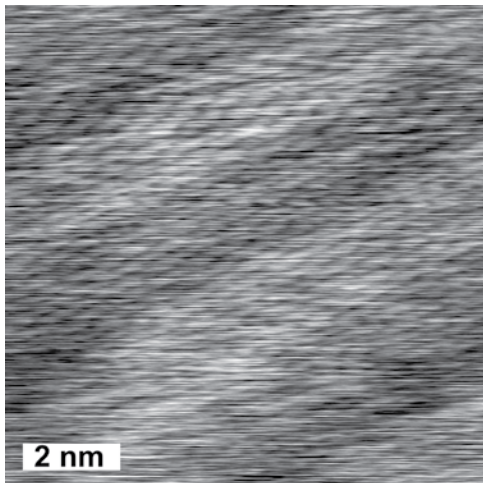
Sample: gold thin film on mica with dust particles. Scanned in contact mode with a standard triangular cantilever (free resonance frequency 15.8 kHz). Environment: air at room temperature. The vertical tip speed reaches up to 1.2 mm/s, but this is at the cost of a very large error signal.

A very different contact mode image is shown in figure 4.8A. This image was acquired in pure water, with a moderate scan speed of 33 lines per second, and serves as an illustration of the noise level of the system. It is clear from the image that the noise in the frequency band below 10 Hz dominates the noise. Images acquired in intermittent contact mode show much less of this noise, which indicates that the cantilever deflection detection system is to blame for most of the low-frequency noise. The low-frequency noise can be filtered with a line-by-line background subtraction, but this introduces artifacts, like jumps between lines and bending in the fast scan direction, especially when noise in a band close to the line frequency is present. The data was therefore filtered in the time domain with a 30 Hz fourth order high pass filter, and subsequently smoothed with a 10 kHz low pass filter to smoothen the influence of the digitization. Because of strong drifts, no signal amplification in the ADC's of the Camera electronics was applied, so the total height of the filtered image is only 36 least significant bit values.

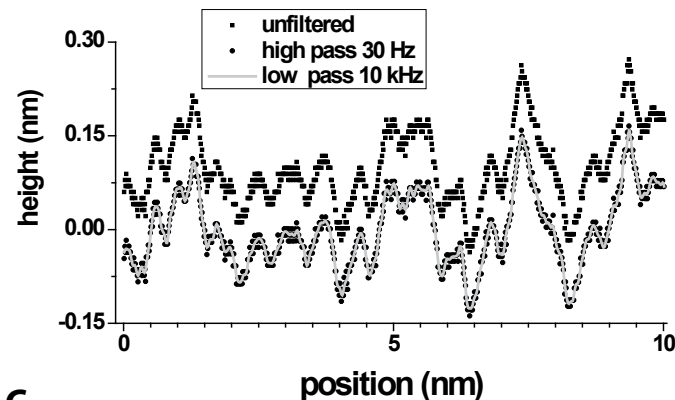
More examples of low-noise measurements, as well as a demonstration of the working of the 3D imaging module are found in chapter 7.



A



B



C

Figure 4.8 Molecular resolution scan in liquid, contact mode

Contact mode scan with a standard cantilever (NP, Digital Instruments) on a dodecanethiol / mercaptoethanesulfonate / aminoethanethiol mixed self-assembled monolayer on gold.

A: unfiltered image, 10x10 nm image with 5.6 nm height scale, image speed 33 lines per second.

B: Filtered image, 0.35 nm height scale, time domain band pass filtered in a 30Hz-10kHz band. The original sample frequency was 68.2 kS/s. The high-pass filtering is very similar to a line-by-line background subtraction, but introduces less jumps between the lines. The wide diagonal bands running from bottom left to top right are artifacts of 50 Hz line frequency interference, but the narrow features correspond to individual molecules.

C: Horizontal cross section of the scan under A) and the effect of the filtering action. The unfiltered curve is offset for clarity.

5 Force versus distance measurements in dynamic AFM: the case of non-constant amplitude

5.1 Introduction

As has been noted before, the atomic force microscope is a versatile instrument, that can be used as an imaging device as well as a force measurement tool. Already early on in the development of AFM, it was realized that a dynamic mode of operation could be beneficial to the spatial resolution of images and the force resolution of force profiles [100]. Two modes of detection in dynamic operation are commonly used: amplitude modulation (AM) and frequency modulation (FM) AFM. Reconstructing force versus distance profiles from dynamic AFM measurements has long been a theoretical problem that has limited quantitative use of this experimental technique. For FM-AFM, Albrecht [36], and Durig and Giessibl [101,102] derived inversion formulas that are valid in limiting cases of very large or very small amplitudes (with respect to the range of the interactions of interest). Recently, Sader and Jarvis [103-105] derived the long-awaited formula for arbitrary amplitudes. This chapter proposes a new method to apply their results to measurements conducted with the AM-AFM technique. Since the hardware of many homebuilt and commercial AFMs does not allow the use of FM-AFM, this can provide many researchers with a new tool for quantitative force measurements.

5.2 The harmonic oscillator as a model for an AFM cantilever

In many practical situations, an AFM cantilever moving through a fluid can be modeled accurately as a point mass m^* , attached to a spring with spring constant k_c , and experiencing viscous drag with drag coefficient γ_c . The equation of motion for the cantilever tip is then:

$$m^* \ddot{z}(t) = -k_c z(t) - \gamma_c \dot{z}(t) + F_{th}(t) + F_d(t) + F_{tip}(t) \quad (5.1)$$

The displacement z is taken relative to the cantilever equilibrium position in absence of external forces, so $z = z_t - z_0$. External forces acting on the cantilever are divided into the thermal force F_{th} , that is responsible for the Brownian motion of the cantilever, the applied driving force F_d , and the interaction forces F_{tip} , acting only on the tip. Generally, we want to measure the latter.

F_{tip} may be further divided into a conservative force $F_{tc}(z)$ and a dissipative force $F_{td}(z, dz/dt)$. A helpful discussion on the subtle differences between conservative / dissipative and even / odd forces can be found in Sader *et al* [105], but here we will adopt the common habit of using the terms “conservative” and “dissipative” even when “even” and “odd” are meant.

Static AFM force measurements correspond to the case where the driving force F_d is zero, and the speed is negligible. The force acting on the tip is then simply equal to the product of the cantilever spring constant and the displacement. When a driving force is present, this is no longer true. Let us now assume that the driving force is a sinusoidal function: $F_d(t) = |F_d|\sin(\omega_d t)$. If we ignore for the moment the tip and thermal forces, we have a completely linear system, and the tip will move sinusoidally at the driving frequency:

$$z(t) = a \sin(\omega_d t + \varphi) \quad (5.2)$$

The well known transfer function of a harmonic oscillator gives us the amplitude and phase shift of the tip motion:

$$a = \frac{|F_d|}{k_c \sqrt{\left(1 - \frac{\omega_d^2}{\omega_c^2}\right)^2 + \frac{\omega_d^2}{\omega_c^2} Q_c^2}} \quad (5.3)$$

$$\varphi = -\pi/2 + \arctan\left(Q_c \left(\frac{\omega_c}{\omega_d} - \frac{\omega_d}{\omega_c}\right)\right), \quad -\pi < \varphi < 0 \quad (5.4)$$

Here we have used the cantilever’s quality factor $Q_c = \sqrt{k_c m^*} / \gamma_c$, and the free resonance frequency $\omega_c = \sqrt{k_c / m^*}$. Throughout this chapter we will assume that the effective mass is not a function of the tip-sample distance. There are situations when this is not justified, however; in a fluid the added mass of the fluid moving with the cantilever may change when the cantilever comes closer to the surface. The range over which this added mass change is significant, is usually of the order of the width of the cantilever [106,107]. As this is long compared to most interactions probed with the tip, the constant mass assumption is very common in the analysis of AFM measurements, and usually justified. If the analysis presented in this chapter is applied to forces with a range that is within an order of magnitude of the cantilever width, the possibility of a distance-dependent effective mass should be kept in mind.

When the tip forces are non-zero, in general the motion can no longer be described by a pure sine. But as long as the force gradients remain much smaller than the cantilever spring constant, a single sine is a good approximation to the trajectory of the tip. This is called the harmonic

approximation. We will come back to cases where this approximation is not valid in chapter 6. Although a sine wave can accurately describe the motion of an oscillating tip that is subjected to tip-sample interactions, the amplitude and phase of the motion are different from the expressions given in (5.3) and (5.4). The effect that the tip force has on the amplitude and phase of the cantilever is used in different ways in the two modes of dynamic AFM.

In AM-AFM, the driving force is constant both in frequency and amplitude. A lock-in amplifier is used to measure the amplitude and phase of the cantilever deflection signal, with the drive signal used as a reference. The measured amplitude and phase are the signals that can be used for feedback during imaging, or for recording during a force-distance cycle.

Albrecht *et al* [36] were the first to realize that for very high cantilever quality factor, such as found under ultra-high vacuum conditions, the response time of AM-AFM is rather slow. Instead of using a constant drive frequency and amplitude, they employed a self-excitation scheme. The deflection signal is phase shifted and amplified, and used as the drive signal. The phase shift is chosen such that the total phase shift between drive and response is 90° . In this way, the cantilever is always at resonance. A feedback system that controls the amplification of the phase shifted deflection signal adjusts the drive amplitude such that the deflection amplitude stays constant. Thus, the first of the two signals available to the user is the frequency shift $\omega_d - \omega_c$, with ω_c the resonance frequency in absence of interaction. The second signal is the drive amplitude needed to attain the set deflection amplitude. The latter is usually called the dissipation signal.

In ultra-high vacuum, the quality factor of the cantilever is often very high. Frequency modulation detection then has two distinct advantages over amplitude modulation: A) A very sharp resonance makes that interactions with the surface easily shift the response curve such that the response amplitude at the original resonance frequency is orders of magnitude lower than for the free oscillation B) The response time of the frequency shift is much lower than the amplitude response time. FM-AFM has therefore been the method of choice in most UHV experiments. At lower quality factors, such as found in ambient or especially in liquid environments, the advantage of using FM-AFM is much reduced. Most importantly, FM-AFM places more stringent requirements on the transfer function of the transducer that generates the cantilever oscillation. The phase response of the transducer should be approximately flat in the entire range of frequencies that are used in a measurement. Peaks or dips in either the amplitude or phase response will lead to artifacts in the measurements, because the measured response is partly due to the transducer. Sharp peaks in the transducer will even lead to instable operation. A piezo element in the cantilever holder, by far the most popular driving transducer, often displays such peaks. Although there is a number of techniques available to excite cantilevers with a flat phase response even in liquids [108-113], these require modifications to the cantilever and/or the instrument. For

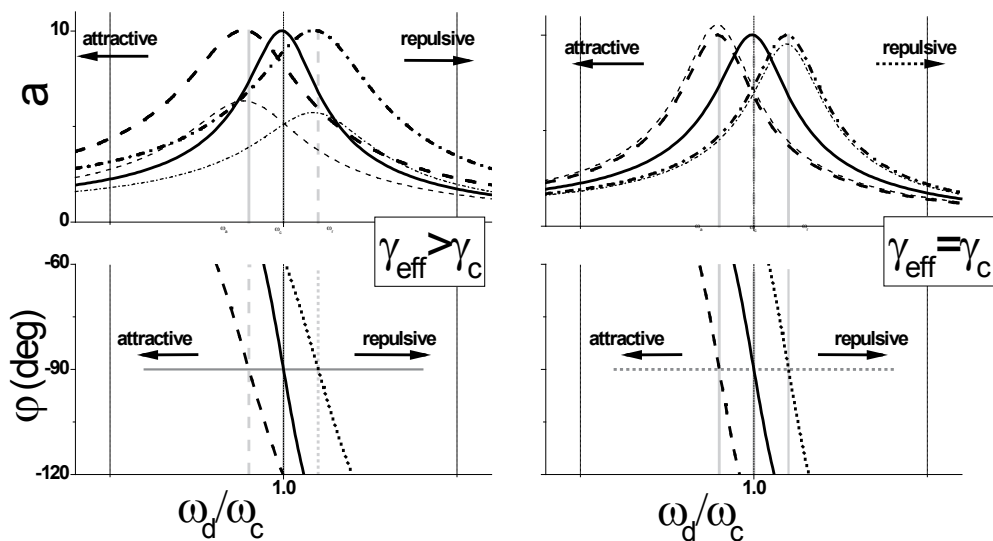


Figure 5.1 Response curves in FM-AFM

The solid lines show the response of a harmonic oscillator with a quality factor of 10. When an interaction shifts the resonance curve towards lower frequencies (attractive interaction, dashed lines) or higher frequencies (repulsive interaction, dotted lines), the driving frequency (vertical lines) is adjusted such that the phase shift (bottom panels) remains at 90 degrees. To remain at constant amplitude, the driving force has to be adjusted, whether the damping coefficient changes (left panels) or not (right panels). Response curves with unadjusted drive amplitude are shown as thinner lines. The relative frequency shift in these figures is $\pm 5\%$, and the damping coefficient for the left panes is 66% higher than for the right panels.

this practical reason, AM-AFM is by far the most used technique for work in ambient or liquids. A graphical illustration of the difference between AM and FM operation is shown in figure 5.1 and figure 5.2.

There are two varieties of dynamic AFM in between the AM and FM modes of operation. Constant Excitation Frequency Modulation (CE-FM) [114,115] uses a variable driving frequency, and frequency modulation detection, but no feedback loop to keep the response amplitude constant. This mode is sometimes preferred when small interaction forces between tip and sample are required. Very recently, Constant Amplitude Phase Modulation AFM was developed [116,117]. This method uses a constant excitation frequency but a variable excitation amplitude. The phase difference between the deflection and drive signals, and the required driving amplitude to keep the deflection amplitude constant are the measured parameters. Improved robustness with respect to several different types of instabilities are mentioned as the main motivation for using this mode.

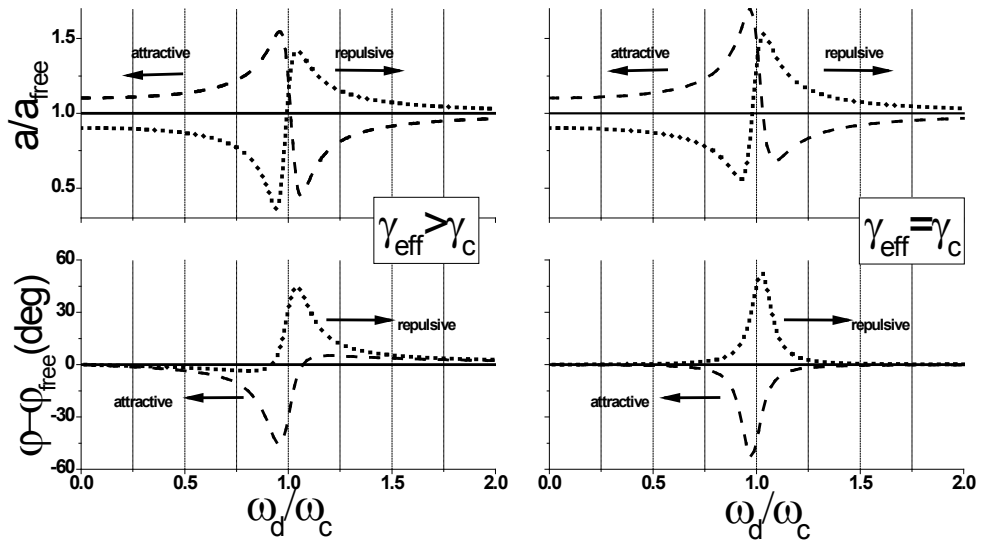


Figure 5.2 Response curves in AM-AFM

The driving frequency and driving amplitude can be chosen freely. Once this choice is made, the amplitude a_{free} in absence of interaction is fixed. The amplitude ratio and phase difference then depend on the interaction with the surface. Solid (flat) line: no interaction, dashed line: attractive interaction, dotted line: repulsive interaction. The same parameters as in figure 5.1 were used.

5.3 Force inversion

When the force F_{tip} in equation (5.1) is known, the tip trajectory can easily be calculated by (numerical) integration. But usually, the tip force is the unknown quantity that one tries to measure. More precisely, the entire profile of the force versus tip-sample distance $F_{tip}(z)$ is sought after. A force-distance curve is then employed as the measurement protocol: the cantilever base to sample distance is varied, and the cantilever deflection is monitored. The inverse problem, getting the tip force from the measured trajectory, is conceptually as simple as calculating the trajectory: one only has to apply equation (5.1) to the measured trajectory and subtract the known forces. In Dynamic Force Spectroscopy (DFS), this requires sampling the cantilever deflection at sampling rates much larger than the cantilever resonance frequency. This method, or similar techniques, have been used by several authors [69,71,72,118-120]. But because it requires special hardware, and generates a large amount of data that has to be processed, Tapping Mode Force Profile Reconstruction - as it is sometimes called - has not yet become a popular method. Because of these practical considerations, AM or FM detection are the common methods of monitoring the cantilever deflection. Conceptually, this makes force inversion far more complicated, as the measured quantities reflect only the interactions averaged over a numbers of oscillations. If the

amplitude is very small with respect to the distance over which the interaction changes, this is not a big problem; the potential can then be linearized. But operation stability, noise concerns or other practical limitations often demand amplitudes of the range of the interaction or even much larger. Many people have therefore been working on formulas that calculate the force from the standard dynamic force microscopy signals, i.e. amplitude and phase for AM detection [67,121-124], or frequency shift and dissipation for FM detection [102,125,126].

Given the nature of the signals that are available to the user, it is not strange that two different paradigms have evolved. In the FM world, a holistic approach is used. The sum of the cantilever harmonic potential and the tip-sample potential is regarded as the system, reacting to an external drive signal, which is the sinusoidal self-excitation signal. This system has an effective spring constant k_{eff} that depends on the interaction as $k_{eff} = \langle k_c + k_{ts}(z) \rangle$, where $k_{ts} = -\partial F_{tc}/\partial z$. The brackets denote an average over the cantilever oscillation period. This in turn makes the resonant frequency of the cantilever-tip-sample system $\omega_{eff} = \sqrt{k_{eff}/m^*}$. The effective damping coefficient can be expressed as $\gamma_{eff} = \langle \gamma_c + \gamma_{ts}(z) \rangle$, and the effective quality factor $Q_{eff} = k_{eff}/(\omega_{eff} \gamma_{eff})$. The quantity γ_{ts} is a generalized damping coefficient, that is defined by the relation $F_{td} = -\gamma_{ts} \dot{z}$. The generalized damping coefficient is not a constant, but can be a function of frequency, speed, amplitude and position, depending on the physical origin of the dissipation. In the case of simple viscous damping, it is independent of experimental parameters like driving frequency and oscillation amplitude, but it can still be a function of the tip position.

Mostly, those who have been involved in force inversion methods for AM-AFM have taken a slightly different approach. They have mostly viewed the cantilever as the system, reacting to a combination of the constant-frequency, constant-amplitude driving force, and a distance-dependent tip-sample force.

5.3.1 Force inversion in FM-AFM

The effective spring constant and resonance frequency are not unique functions of the distance to the sample. Even though the conservative tip-sample force and hence the tip-sample spring constant are uniquely defined, the way they are averaged depends on the oscillation amplitude. The most general formulation for this was published by Durig [101,127]. Through a Fourier analysis, he found that as long as the motion is sinusoidal, the frequency shift can be calculated by:

$$\Omega(d) = \frac{\omega_{eff}(d) - \omega_c}{\omega_c} = \int_{-1}^1 F_{tc}(d + (1+u)a) \frac{u}{\sqrt{1-u^2}} du \quad (5.5)$$

This integral is a convolution of the tip-sample force with a term that diverges at both ends of the integral. The divergence reflects the fact that at the turnaround points of the oscillation, the velocity is zero. Force inversion then consists of the deconvolution of this diverging function.

Approximating formulas for small and large amplitudes, and exact inversions for specific force laws have been published. The most simple case is the small amplitude limit: when the force gradient can be considered constant over the oscillation amplitude, the frequency shift is simply linear with the force gradient [36]:

$$\begin{aligned} \left| a \frac{\partial^2 F_{tc}}{\partial z^2} \right| \ll |k_{ts}| &\Rightarrow k_{ts} \approx 2k_c \Omega \\ \Rightarrow F_{tc}(d) &= 2k_c \int_d^\infty \Omega(t) dt \end{aligned} \quad (5.6)$$

For very large amplitudes, we only have to consider the forces at the turnaround points. The large amplitude approximation is therefore [101]:

$$F_{tc}(d) = -\frac{a^{3/2}}{\sqrt{2}} \int_d^\infty \frac{\partial k_{\text{eff}}}{\partial z} \frac{dz}{\sqrt{z-d}} \quad (5.7)$$

The inversion problem for FM-AFM was solved recently for arbitrary amplitudes by Sader and Jarvis [104,105]. Based on a Laplace transform approach, combined with the properties of fractional integrals, they found a solution to the inverse formula of equation (5.5):

$$F_{tc}(d) = 2k_c \int_d^\infty \left(\left(1 + \frac{a^{1/2}}{8\sqrt{\pi(u-d)}} \right) \Omega(u) - \frac{a^{1/2}}{\sqrt{2(u-d)}} \frac{d\Omega(u)}{du} \right) du \quad (5.8)$$

Formally, this formula is an approximation. The approximation lies in the fact that the function $\frac{1}{2}x(1 + \frac{1}{8}\sqrt{x} + \sqrt{\frac{\pi}{2}}x^{\frac{3}{2}})$ is used to approximate $I_1(x)\exp(-x)$, where $I_1(x)$ is the modified Bessel function of the first kind of order one. The error is never more than 5%, but if higher precision is needed extension of the formula is possible by the use of a polynomial with more terms for the approximation [104,105]. This formula is valid for any force law, and any free amplitude used, as long as the motion is sinusoidal. The limits of the assumption that the motion is sinusoidal, which mathematically cannot be the case when the tip moves in an anharmonic potential, will be discussed in chapter 6. Furthermore, in the derivation of this formula, it is assumed that the amplitude is constant, and the cantilever is driven at resonance, as is usually the case in FM-AFM. An extension to the formula was later published that deals with a correction for those cases when the cantilever is driven at a different frequency than the resonance frequency [128]. The expression has a closed form, and the force-distance curve is easily recovered from the frequency-shift versus distance curve through numerical integration and differentiation. These properties make formula (5.8) a very practical formula to use for force inversion.

5.3.2 Dissipation measurements in AFM

One of the advantages of using dynamic, as opposed to static, force measurement techniques in AFM is that it offers the possibility to measure dissipative as well as conservative forces. This offers a possibility to make images with material contrast added to topographical information, and offers insight into molecular scale damping. The measurement of dissipative forces is usually done by measuring the total amount of energy dissipated per oscillation cycle.

The total dissipated power by the tip-sample interaction in dynamic AFM experiments can be calculated using a power balance [126,129]. The instantaneous driving power delivered to the cantilever is $P_{in}(t) = F_d(t) * \dot{z}$. The instantaneous power dissipated is $P_{out}(t) = P_{ts}(t) + P_c(t) = (\gamma_{ts} + \gamma_c) * \dot{z}^2$. If the driving force and motion are sinusoidal, this becomes $P_{in}(t) = |F_d| \sin(\omega_d t) * a \omega_d \cos(\omega_d t + \varphi)$ and $P_{out}(t) = (\gamma_{ts} + \gamma_c) * a^2 \omega_d^2 \cos^2(\omega_d t + \varphi)$. The dissipation in the case of a non-sinusoidal motion was worked out by Ashby [118], but this will not be treated here. If we consider only steady-state situations, the average power dissipated

by the cantilever and tip is equal to the input power: $\langle P_{out} \rangle = \frac{\omega_d}{2\pi} \int_0^{2\pi/\omega_d} P_{out}(t) dt = \langle P_{in} \rangle$. Thus, the power balance for one oscillation cycle becomes:

$$\langle P_{in} \rangle = -\frac{1}{2} a \omega_d \sin(\varphi) |F_d| = \frac{1}{2} a^2 \omega_d^2 (\langle \gamma_{ts} \rangle + \gamma_c) = \langle P_{out} \rangle \quad (5.9)$$

In FM-AFM, the amplitude is constant and the phase is $-\pi$, so the balance for the power dissipated during one oscillation cycle becomes:

$$\langle P_{tip} \rangle = \langle P_{out} - P_c \rangle = \langle P_{free} \rangle \frac{\omega_{eff}}{\omega_c} \Theta \quad (5.10)$$

With the power dissipated by the free cantilever $\langle P_{free} \rangle = \frac{1}{2} a^2 k_c \omega_c / Q_c$ and the damping function $\Theta = |Fd| / |Fd|_{free} - \omega_{eff} / \omega_c$. Subscripts “free” are used here for values that reflect experimental conditions that can be tuned, in contrast to values with subscript “c”, that refer to properties that follow from dimensions and material constants of the cantilever and medium. In AM-AFM, the driving frequency and the driving power are constant, so that the power balance yields:

$$\begin{aligned} \langle P_{tip} \rangle &= \frac{1}{2} a \omega_d (-\sin(\varphi)) |F_d| - \gamma_c a \omega_d \\ &= \langle P_{free} \rangle \frac{a}{a_{free}} \left(-\sin(\varphi) \sqrt{\left(\frac{\omega_c - \omega_d}{\omega_d \omega_c} \right)^2} + \frac{1}{Q_c^2} - \frac{a}{a_{free}} \frac{k_c}{\omega_c Q_c} \right) \end{aligned} \quad (5.11)$$

Where we have used equation (5.3) to express the driving force in measurable parameters. In the case of AM-AFM, the driving frequency is not necessarily the resonance frequency, and $\langle P_{free} \rangle = \frac{1}{2} a_{free}^2 k_c \omega_d^2 / \omega_c Q_c$.

The powers in equations (5.9) - (5.11) are quantities that are averaged over the cantilever oscillation amplitude. In many cases, one is interested in the distance dependence of the damping coefficient. To measure this, one has to employ Dynamic Force Spectroscopy. If the experimental conditions do not allow for a free amplitude that is much smaller than the range over which the damping coefficient varies, this leads to a problem very similar to the force inversion problem.

For frequency-modulation AFM, Sader *et al* show in ref. [105] that although the convolution of the generalized damping coefficient with the cantilever motion is not the same as that of the frequency shift, it can be written such that they are mathematically equivalent. The deconvolution method used to obtain formula (5.8) can also be applied to the generalized damping coefficient, and this yields the following equation:

$$\gamma_{ts}(d) = -\gamma_c \frac{\partial}{\partial d} \int_d^{\infty} \left(\left(1 + \frac{a^{1/2}}{8\sqrt{\pi(u-d)}} \right) \Theta(u) - \frac{a^{3/2}}{\sqrt{2(u-d)}} \frac{d\Theta(u)}{du} \right) du \quad (5.12)$$

5.4 A new force inversion method for AM-AFM

5.4.1 Previous work

The amount of work done to achieve exact force-inversion formulas for AM-AFM is considerably less than in FM-AFM. An explanation for this, is that AM-AFM is mainly used for imaging purposes. The most common method for investigation of force-distance relations in liquid or ambient environment is static deflection detection. In those situations in which the forces exerted in AM-AFM were calculated, the motivation has often been either finding the right parameters for imaging with a low force on soft samples [130,131], or interpretation of phase images in terms of material properties [123,129,132]. Most studies have therefore concentrated on calculating effective (oscillation-averaged) forces and frequency shifts with a given force profile. Often, numerical simulations of the tip trajectory are used [124,131,133-135]. An advantage of this method is that it can go beyond the harmonic approximation. Many studies show that this approximation is not valid in a number of typical experimental situations [120,124,131,135-138]. An obvious shortcoming is that an assumption about the functional form of the force profile has to be made in advance. Two force inversion methods based on the harmonic approximation have appeared fairly recently. Hölscher [121] proposed an AM analog to formula (5.7), valid for large amplitudes. Lee and Jhe [139] used a method similar to that of Sader [104,105] to find differential equations to calculate the interaction forces. Although their method is quite general, they do not propose a closed-form formula.

5.4.2 From amplitude and phase to frequency shift and effective Q factor

As long as the harmonic approximation is valid, it is possible to unite the two paradigms of dynamic force microscopy. The key to this is viewing the cantilever as an oscillator that is harmonic, but has a resonance frequency and quality factor that both depend on the tip-sample interaction. If neither the mass nor the driving force change with time, the measured amplitude and a_{free} , the amplitude in absence of an interaction, are related by the following formula

$$a = a_{free} \frac{\frac{|F_d|}{m^* \sqrt{(\omega_{eff}^2 - \omega_d^2)^2 + \frac{\omega_{eff}^2 \omega_d^2}{Q_{eff}^2}}}}{\frac{|F_d|}{m^* \sqrt{(\omega_c^2 - \omega_d^2)^2 + \frac{\omega_c^2 \omega_d^2}{Q_c^2}}}} = \frac{a_d}{\sqrt{\left(\left(\frac{\omega_{eff}}{\omega_d}\right)^2 - 1\right)^2 + \frac{\omega_{eff}^2}{\omega_d^2 Q_{eff}^2}}} \quad (5.13)$$

For convenience, we use the zero-frequency related driving amplitude

$a_d = (a_{free} / \omega_d^2) \sqrt{(\omega_c^2 - \omega_d^2)^2 + \omega_d^2 \omega_c^2 / Q_c^2}$, which can be calculated from experimentally accessible parameters.

The phase shift is given by

$$\varphi = -\pi/2 + \arctan\left(Q_{eff} \left(\frac{\omega_{eff}}{\omega_d} - \frac{\omega_d}{\omega_{eff}}\right)\right) \quad (5.14)$$

The disentanglement of the contributions of frequency and quality factor from the equations (5.13) and (5.14), can be done by rewriting them, solving for the resonance frequency and quality factor. The two resulting equations are:

$$\omega_{eff} = \omega_d \sqrt{1 + \frac{a_d}{a} \cos(\varphi)} \quad (5.15)$$

$$Q_{eff} = \frac{-1}{\sin(\varphi)} \frac{a}{a_d} \sqrt{1 + \frac{a_d}{a} \cos(\varphi)} \quad (5.16)$$

Verification of these formulas by inserting them back into equations (5.13) and (5.14) is straightforward. It should be stressed that the functional form of equations (5.15) and (5.16) depends on both the choice to model both the drive and the response as a sine (as opposed to a sine and a cosine), and the choice of the sign of the phase in equation (5.2). Modifying these expressions to

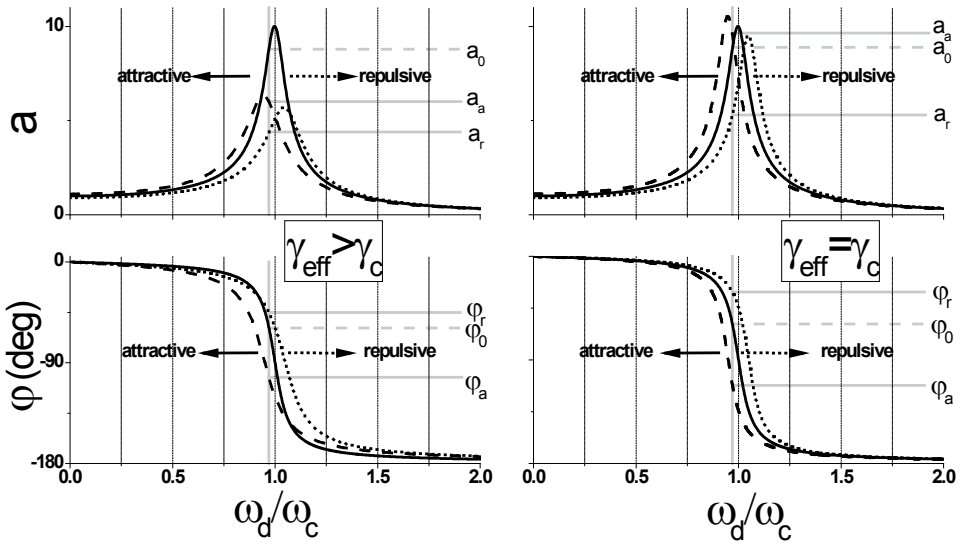


Figure 5.3 Effective frequency shifts and amplitude variations in AM-AFM

Graphical representation of how tip-surface interactions modify cantilever response in the harmonic oscillator model. The solid lines show amplitude and phase response as a function of driving frequency for a cantilever with a quality factor of 10. Dotted and dashed lines show the influence of an interaction that increases or decreases the resonance frequency with 5 % respectively. The left-hand graphs represent a situation when in addition to the conservative interaction, the effective damping coefficient is increased with 40%. The right-hand graphs show the situation when the damping coefficient is unaffected. The light grey vertical line represents an arbitrarily chosen AM driving frequency, and the light grey horizontal lines show the behavior of the amplitude and phase at this frequency. Both these variables are needed to recover the effective frequency and damping coefficient.

accommodate other definitions of the phase is straightforward, but one should be aware of how the phase is defined when these formulas are to be applied to measured data.

Analogs to these formulas have been used before in a slightly modified form in the context of small-amplitude AFM in liquids, using not the resonance frequency and quality factor, but interaction stiffness and damping as variables [67]. The advantage of using the resonance frequency as the variable is that this allows to use the force-inversion tools developed for FM-AFM to be used. Some other formulas for effective resonance frequency estimation, for example that published by Martin [140] use a distance-independent quality factor to get the frequency shift from the phase. Furthermore, they use an approximation of the square root to get to a closed expression. Whangbo [123] relies on taking an amplitude and phase versus frequency curve at each distance to experimentally measure the resonance frequency and quality factor.

5.4.3 Frequency shift to force

When we have extracted the frequency shift from the amplitude and phase data, using equations (5.15) and (5.16), it is straightforward to calculate the force and generalized damping coefficient. First we calculate the relative frequency shift and the damping function for Amplitude Modulation AFM from measured parameters by

$$\Omega_{AM}(d) = \frac{\omega_d}{\omega_c} \sqrt{1 + \frac{a_d}{a(d)} \cos(\varphi(d))} - 1 \quad (5.17)$$

$$\Theta_{AM}(d) = -\frac{\omega_d}{\omega_c} \sqrt{1 + \frac{a_d}{a(d)} \cos(\varphi(d))} \left(\frac{Q_c a_d \omega_d}{a(d) \omega_c} \sin(\varphi(d)) + 1 \right) \quad (5.18)$$

And we insert them into formulas and to obtain

$$F_{tc}(d) = 2k_c \int_d^\infty \left(1 + \frac{a(u)^{1/2}}{8\sqrt{\pi(u-d)}} \right) \Omega_{AM}(u) - \frac{a(u)^{3/2}}{\sqrt{2(u-d)}} \frac{d\Omega_{AM}(u)}{du} du \quad (5.19)$$

$$\gamma_{ts}(d) = -\gamma_c \frac{\partial}{\partial d} \int_d^\infty \left(1 + \frac{a(u)^{1/2}}{8\sqrt{\pi(u-d)}} \right) \Theta_{AM}(u) - \frac{a(u)^{3/2}}{\sqrt{2(u-d)}} \frac{d\Theta_{AM}(u)}{du} du \quad (5.20)$$

It is of course necessary to use the amplitude and phase as a function of the closest approach distance d . A common way to calculate the closest approach distance is using $d = z_c - a(z_c)$. To what degree this is justified will be discussed in chapter 6. An important difference with formulas (5.8) and (5.12) is that the amplitude is not a constant here, but depends on the distance. In the derivation of (5.8) and (5.12), it is explicitly assumed that the amplitude is constant. The properties of the Laplace transform, that are used in the derivation, do not apply for non-constant amplitudes. Nevertheless, formulas and are exact in both the large and the small amplitude limit. They are therefore an approximation to the arbitrary amplitude case. In contrast to formulas (5.8) and (5.12), we have no analytical expression for the error bound of this approximation. In other words, it is not rigidly possible to say how well they approximate the real force and damping coefficient.

5.4.4 Simulation approach to verification of the force-inversion method

To estimate how well formulas and approximate the real forces acting on the tip, a number of experiments were simulated. A Dynamic Force Spectroscopy simulation program was written in C++. This simulation was constructed such that it models an actual AM dynamic force spectroscopy experiment as closely as possible. The equation of motion is integrated numerically, while with each timestep the cantilever base to sample distance is adjusted. In this way, the tip trajectory is calculated. A numerical lock-in algorithm is applied to the data to calculate the

amplitude and phase shift. A large number of points per oscillation is used, typically several thousands. In a simulation of a high-frequency cantilever, recording the entire trajectory during the simulation of a typical experiment of a few seconds would lead to very large data files. For this reason, calculation of amplitude and phase is done during the simulation, and only these quantities, along with the cantilever base position, time and average deflection, are stored on disk. For further inspection, it is possible to store an interleaved version of the entire trajectory, with a lower number of points than that used in the calculation.

The user can specify:

- The force and damping profiles as a function of tip-sample distance.
- The cantilever properties resonance frequency, quality factor, and spring constant.
- The experimental parameters free amplitude, driving frequency, approach time and distance.
- The time step for the simulation, time in between lock-in measurements and an optional number of points of the time trace to save to a separate file.

Using this program, a number of different experimental situations were simulated. The results of the simulation were inserted into formulas and , to calculate the force and damping profiles. These calculated values were then compared to the force and damping profiles that were used as input for the simulation. For the free amplitude a range of values was chosen, from much smaller than σ (the typical length scale of the potential), to much larger. Furthermore, both driving above and below the resonance frequency was simulated. A quality factor of 400, typical for measurements in air, was used. The force profile chosen was a Lennard-Jones-like potential: $F_{tc}(d) = \epsilon\sigma(\sigma^4/d^6 - 1/d^2)$, since this profile exhibits both repulsive and attractive forces, with very different distance behavior. To investigate the influence of damping on the force inversion results, and vice versa, the same simulation parameters were used with and without including a distance-dependent damping. When damping was included, a damping profile decaying exponentially with distance was used, with a decay constant $\frac{1}{4}$ of the length scale of the conservative force: $\gamma_{ts}(d) = \gamma_c \exp(-4d/\sigma)$.

All these different experimental situations lead to a variety of different amplitude-distance and phase-distance profiles. Nevertheless, as can be seen from the figures , the input force and damping profile can be recovered in all different experimental situations. The correspondence in the force profile reconstruction for low quality factor cantilevers is slightly worse for large amplitudes. This reflects the fact that higher harmonics of the driving frequency have a relatively larger influence when the cantilever quality factor is lower.

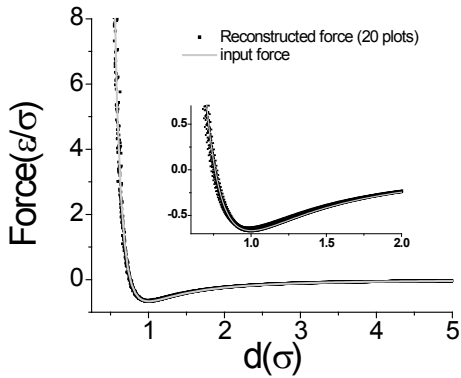


Figure 5.4 Reconstructed force profiles for a high quality factor

Results of numerical simulations reconstructed to force-distance profiles. Quality factor of the cantilever in the simulations was 400. Experiments with a driving frequency 1/1000 above and below the resonance frequency, and with and without distance-dependent damping were simulated. For each of these cases, free amplitudes of 0.1, 0.5, 1, 2, and 10 times σ were simulated. All reconstructed force curves deviate less than 5% from the input force.

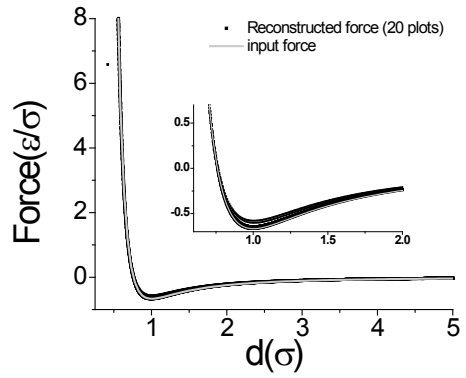


Figure 5.6 Reconstructed force for a low quality factor

Results of numerical simulations reconstructed to force-distance profiles. Quality factor of the cantilever in the simulations was 2. Experiments with a driving frequency 3% above and below the resonance frequency, and with and without distance-dependent damping were simulated. For each of these cases, free amplitudes of 0.1, 0.5, 1, 2 and 10 times σ were simulated. Out of 20 reconstructed force curves, only the largest amplitude curves with included damping deviate more than 5% from the input force. Maximum deviation there is 12 %.

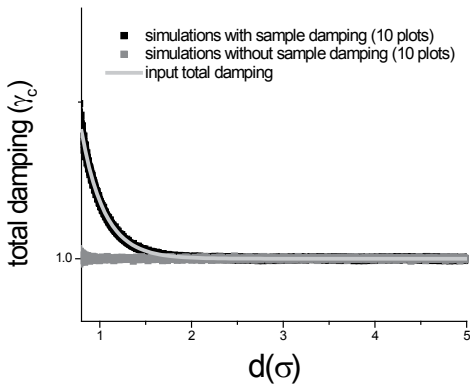


Figure 5.5 Reconstructed damping for a high quality factor

Reconstructed effective damping profiles for a cantilever with a quality factor of 400. The exponential added damping profile is recovered for all experimental situations.

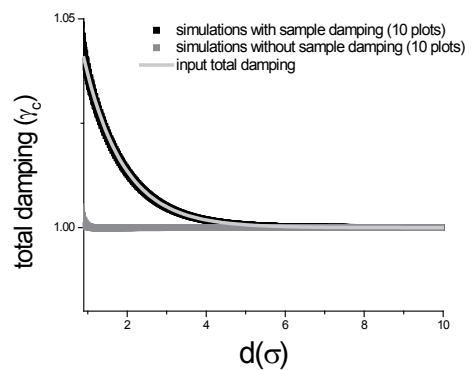


Figure 5.7 Reconstructed damping for a low quality factor

Reconstructed effective damping profiles for a cantilever with a quality factor of 2. The exponential added damping profile is recovered for all experimental situations.

6 Exploring the limits of amplitude modulation force spectroscopy with numerical experiments

In the previous chapter, a method was developed to calculate profiles of the force and damping coefficient versus distance from measured amplitude and phase versus distance profiles. The validity of this method was asserted with numerical calculations of cantilever dynamics. In this chapter, the same type of calculations is used to explore the boundaries of some of the assumptions that were made in the derivation of the force inversion method of chapter 5. The errors that arise when these assumptions are violated are illustrated, and the underlying mechanisms for these errors will be made clear. Furthermore, the influence of experimental parameters on the signal to noise ratio is explored. Primary goal of this chapter is to provide the experimentalist with the knowledge that is necessary to choose the optimal setting of parameters in an Amplitude Modulation-Dynamic Force Spectroscopy (AM-DFS) experiment .

6.1 Phase offsets and finite measurement range

The main result of chapter 5 is that when amplitude and phase are measured as a function of distance in an AM-DFS experiment, the frequency shift and damping functions can be calculated by

$$\Omega_{AM}(d) = \frac{\omega_d}{\omega_c} \sqrt{1 + \frac{a_d}{a(d)} \cos(\varphi(d))} - 1 \quad (6.1)$$

$$\Theta_{AM}(d) = -\frac{\omega_d}{\omega_c} \sqrt{1 + \frac{a_d}{a(d)} \cos(\varphi(d))} \left(\frac{Q_c a_d \omega_d}{a(d) \omega_c} \sin(\varphi(d)) + 1 \right) \quad (6.2)$$

These functions are the equivalents of the frequency shift and dissipation signals measured in FM-AFM. They can be weighted and integrated to obtain the conservative force and generalized damping coefficient as function of the distance:

$$F_{tc}(d) = 2k_c \int_d^\infty \left(\left(1 + \frac{a(u)^{1/2}}{8\sqrt{\pi(u-d)}} \right) \Omega_{AM}(u) - \frac{a(u)^{3/2}}{\sqrt{2(u-d)}} \frac{d\Omega_{AM}(u)}{du} \right) du \quad (6.3)$$

$$\gamma_{ts}(d) = -\gamma_c \frac{\partial}{\partial d} \int_d^\infty \left(\left(1 + \frac{a(u)^{1/2}}{8\sqrt{\pi(u-d)}} \right) \Theta_{AM}(u) - \frac{a(u)^{3/2}}{\sqrt{2(u-d)}} \frac{d\Theta_{AM}(u)}{du} \right) du \quad (6.4)$$

In an experimental situation, the measurement of the phase shift is usually performed by using the voltage that drives an excitation transducer (e.g. piezo element or coil) as the reference for a lock-in measurement of the signal that comes from the deflection detection system. If there is any delay in either the excitation or the measurement, this will cause a phase offset. This phase offset should be properly calibrated, and subtracted from the data before the application of equations (6.1) and (6.2). Even very small phase offsets can lead to large deviations in the force, since the offsets are integrated over the entire measurement range. A good way of calibrating the phase offset is to hold the cantilever at a distance from the surface that is far away enough to exclude tip-sample interaction effects, and measure at this position both the Brownian motion spectrum of the cantilever, and the amplitude and phase lag when a drive is applied. A fit of the driven harmonic oscillator equation (5.3) will then provide the cantilever's resonance frequency and quality factor. These can then be used to calculate the frequency shift and damping function using equations (6.1) and (6.2). The phase offset should be chosen such that the frequency shift is zero at this distance. The position where this calibration is done should preferably be chosen still reasonably close to the surface, since phenomena such as cantilever squeeze damping or optical interference can alter the phase offset, resonance frequency and quality factor.

A second cause of offsets in measuring force profiles in real or simulated experiments is finite measurement range. To yield the correct value of force and damping coefficients, the measured amplitude and phase profiles should extend to infinite distance. In practice, the measurement range is always finite, and often a short range is preferred to achieve high spatial resolution. If the force is finite at the far end of the force profile, both the force and the force gradient are misestimated. It is therefore advisable to always extend the measurement to a distance where neither amplitude nor phase changes with distance. If high spatial resolution is required close to the sample, combining short-range and long-range measurements is a good option.

6.2 Limits of the harmonic approximation

The force inversion method was derived on the basis of the harmonic approximation, i.e. assuming that the motion of the cantilever is completely described by the amplitude and phase of a sine

wave of a frequency equal to the driving frequency. In practice, this means that the conservative force gradient should be much lower than the cantilever spring constant, and the gradient of the generalized damping coefficient should be much less than the viscous drag coefficient of the cantilever divided by the oscillation amplitude. It is not so much the magnitude of the tip-sample forces themselves that leads to deviations from this assumption, but the magnitude of the gradients. For example, a strong, but constant conservative tip-sample force will only lead to a static bending of a cantilever in addition to the oscillation, and a large damping coefficient will lower the amplitude, but the shape of the oscillation remains the same. If static bending occurs, it should of course be included when calculating the distance of closest approach.

6.2.1 High stiffness potentials

To investigate the influence of a high stiffness potential on the accuracy of the force reconstruction equation, a Dynamic Force Spectroscopy experiment was simulated. The cantilever in this experiment had a spring constant of 25 N/m, and the tip force was a Lennard-Jones force $F_{tc}(d) = \epsilon\sigma(\sigma^4/d^6 - 1/d^2)$, with a length scale $\sigma=0.6$ nm and an energy scale $\epsilon = 5 \cdot 10^{-19}$ J. This model force profile has an extremely steep repulsive part at close distances, steeper than more realistic models such as the Derjaguin-Müller-Toporov [141] or Maugis [142] models of contact mechanics. Free amplitudes of 0.5 and 10 nm were used, and quality factors of 2 and 100. Thermal noise was left out in this simulation. The amplitude-distance curves for these four cases are displayed in figure 6.1. It is immediately visible from the amplitude distance curve for low amplitude and high quality factor, that there is an instability around $z_0=0.75$ nm. This phenomenon is well known, and is a consequence of the fact that there are multiple solutions to the equation of motion in the presence of a combination of attractive and repulsive forces [46,124,143]. As can be seen from the reconstructed force-distance plot in figure 6.2, this jump is not a problem for the force reconstruction. There is a gap in the force profile, but after the jump, the force continues with correct values.

If we take a closer look at the high forces that occur at close approach distances, we see that the reconstructed force starts to deviate. Because the driving force is largest for the large-amplitude, low quality factor experiment, one might expect that this would suffer the least from deviations that are caused by the high sample stiffness. Nevertheless, the deviation appears at the same point and with the same magnitude as for the high quality factor experiment. A first hint at what causes this unexpected behavior can be found in the amplitude profile, if we plot this against the closest approach distance instead of the cantilever base displacement. This is done in figure 6.3.

The amplitude as a function of closest approach distance shows a strong inward bending, which means that the closest approach distance goes up, even though the cantilever base position is brought down. This bending immediately explains why there are fewer points at close approach

distance for the low quality factor cantilever in figure 6.2. When the bending sets in, formula (6.3) cannot be applied anymore, because the frequency shift is no longer a single-valued function of the distance. Furthermore, the term containing the square root will become an imaginary number. We would like to point out that none of the points in figure 6.2 corresponds to the amplitude bending region, as the algorithm that is used to compute the force outputs ‘not a number’ values in this case. In some cases, the bending can be caused by a shift in the effective resonance frequency of the tip. This shift may lower the response amplitude of the cantilever so much that the closest approach amplitude goes up. But a frequency shift will only cause a bending if the major contribution to the frequency shift comes from a tip-sample interaction acting over the entire trajectory of the tip. Furthermore, this effect is stronger for higher quality factors, while for the curves depicted in figure 6.3, the bending is much more pronounced for the low quality factor. This suggests that there is a different mechanism going on here. To see what is actually happening, we must look at the total trajectory of the tip, not just at the measured amplitude and phase.

Figure 6.4 shows three excerpts from simulation time traces. They are plotted together with the time traces that correspond to a purely sinusoidal curve with the amplitude and static bending that are measured from the actual trace. This trace, that will henceforth be referred to as the harmonic trajectory, is calculated by taking a sine wave with the amplitude measured at the closest point in time to where the excerpt was taken. The phase of the harmonic trajectory is not related to the measured lock-in phase, but adapted such that the first zero crossings of the simulated time trace and harmonic trajectories occur at the same moment in time. Figure 6.4a shows the trace for the cantilever with a quality factor of 100, at the point where the amplitude has been reduced from 10 to 8.7 nm. This is at a point higher than where the bending occurs. The deviations of the inferred trajectory from the real trajectory are below 0.3% of the amplitude. The main deviation is caused by the long attractive tail of the potential. This causes the trajectory to have a slightly steeper downward slope than upward slope, and this gives a slight overshoot in the downward direction with respect to the harmonic trajectory. The same effect, with a slightly larger magnitude, can be seen in figure 6.4B. This time trace is taken from the simulation of the cantilever with quality factor 2, at the upper left tip of the amplitude-distance curve of figure 6.3. Even though the amplitude reduction is only 0.02 nm, the deviation from the harmonic trajectory is already 0.12 nm. Note that this amplitude reduction is one to two orders of magnitude smaller than what is typically used in imaging applications. The shape of the trajectory is still very much like a sine wave, but the distance of closest approach is overestimated by the harmonic trajectory. When the tip is brought closer to the surface, the shape of the trajectory deviates much more strongly from the harmonic. The long attractive tail of the potential accelerates the tip on its downward path, and it is quickly stopped and accelerated back up by the sharp rise of the potential below $d = 0.6$ nm. The sharp features at the bottom of the trajectory are filtered out by the lock-in, which results in an overestimate of the closest approach distance.

The force inversion method described by equation (6.3) was derived assuming a sinusoidal trajectory of the tip. The oscillation amplitude was assumed to describe both the range of tip-sample separations the tip travels through during one oscillation, and the relative amount of time spent at each separation. The presence of higher harmonics in the deflection signal alters both these quantities. This observation points to a possible strategy to improve the range of applicability of the force inversion method. The tip-sample separation range can be more accurately measured by taking the minimum and maximum of the trajectory in a time interval, instead of using a lock-in algorithm. This is analogous to the signals coming from the peak detection system used in high speed AFM [46], as was also used in some of the experiments described in this thesis, or the commercially available TREC system [92]. In the following, we will investigate whether the use of peak-to-peak amplitude estimation can lead to improved accuracy of force inversion in AM-DFS.

If we plot half the peak-to-peak amplitude versus the minimum separation for a simulation with exactly the same parameters that generated the curves of figure 6.3, we get the curves displayed in figure 6.5. The bending of the amplitude-distance curves is now only present in the curves of high quality factor cantilevers, at distances below 0.5 nm. This bending can be assigned to a frequency shift.

The amplitude-distance curves obtained from the full trajectories can be used as input for the force inversion formulas, to see the real effect of non-sinusoidal motion on the accuracy of the force inversion algorithm. Although the peak-detection method gives an easy handle on the amplitude of the trajectory, it is much more difficult to assign a single phase lag. The amount by which the trajectory trails the driving signal changes within a fraction of an oscillation, and the zero crossings occur at the same point as the harmonic trajectory. We therefore continue to use the phase information that is obtained by the lock-in. Force curves reconstructed from the peak-to-peak amplitudes and lock-in phase are shown in figure 6.6. As compared to the results shown in figure 6.2, the steep repulsive part of the force profile at close separations is followed more closely for all situations.

In the foregoing, the presence of higher harmonics in the cantilever deflection signal due to a steep force gradient was shown to lead to misinterpretation of the interaction force in the region where the interaction stiffness is larger than the cantilever stiffness. The misinterpretation is mainly due to the wrong estimate of peak-peak amplitude, and hence also of closest approach distance, that arises when peak-peak amplitude is estimated from a measurement of the RMS amplitude of the first harmonic. In the case investigated here, fidelity of the reconstructed force is extended up to a range where the contact stiffness is orders of magnitude higher than the cantilever stiffness by using the correct peak-peak amplitude. This suggests that the force reconstruction method is

quite robust with respect to deviations from a sinusoidal trajectory. But since the nature of the deviation from a sinusoidal trajectory depends strongly on the shape of the potential, we should be careful not to generalize these results to other potentials. Nevertheless, these results suggest that the force inversion method is at least as robust as the quite generally accepted method of measuring a cantilever's oscillation amplitude by only the amplitude of the first harmonic.

6.2.2 Effects of strong damping gradients

Just as large force gradients, strong damping gradients can lead to deviations from the harmonic approximation. However, the nature of these deviations is very different. Furthermore, if there are both conservative and dissipative forces present, the effects of these forces may counteract or strengthen each other. An illustration of the effect of a damping coefficient that varies strongly with distance is shown in figure 6.7. A Lennard-Jones force profile with $\sigma=2$ nm and $\epsilon=5\cdot 10^{-19}$ J, combined with a damping profile that falls off exponentially with distance with a decay constant of 0.5 nm and zero distance value of 50 $\mu\text{Ns/m}$ was used. The two cantilevers that are compared have intrinsic damping coefficients of 5.3 $\mu\text{Ns/m}$ and 0.073 $\mu\text{Ns/m}$.

For the standard cantilever, the variation in damping coefficient gives only a small perturbation to the amplitude and phase profiles. All qualitative features of the profiles are the same whether or not damping is included. For the small cantilever however, a number of things change considerably. Most noticeably, the amplitude decay close to the surface is completely dominated by the damping for small and intermediate amplitudes, and the phase shift change upon contact is reversed for a large amplitude. Not surprisingly, this has effects on the accurateness of the force inversion. For the standard cantilever, the force and damping profiles are reconstructed correctly in all cases. Only at the closest separations, where the force is very high and higher harmonics induced by the potential stiffness start to play a role, the damping is strongly overestimated. At larger separations, the small (<10%) misestimation of the total damping coefficient leads to a large misestimation of the tip damping, because the intrinsic damping of the cantilever is so much larger.

For the small cantilever, the smallest (0.2 nm) free amplitude profile reconstructs very well, since the gradient of the damping is only small when evaluated over one oscillation cycle. The 2 nm free amplitude profile from a simulation which included damping shows a dip in the force and a bend in the damping roughly between 2.7 and 2 nm separation. At smaller separations, the reconstruction returns to the correct values. Interestingly, this sort of feature is also seen in simulations with no distance-dependent damping for a cantilever with the same force constant, but a higher quality factor (data not shown). What causes it is not yet clear.

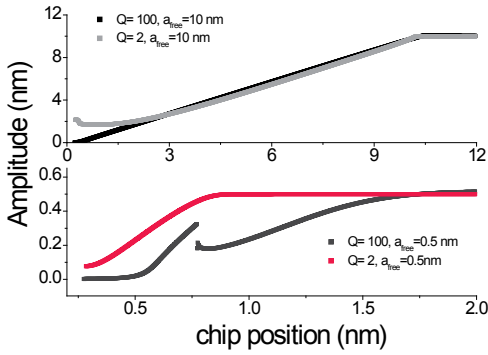


Figure 6.1 Amplitude versus chip position in a simulated DFS experiment

The sharp jump in the black curve around $z_0=0.75$ nm is a result of a switch between the two solutions of the equation of motion. At small driving amplitudes, it is clearly visible that the amplitude of a low quality factor cantilever is much less affected by the tip-sample force. This effect is also present for the large driving amplitude, but only close to the first bending point around $z_0 = 10$ nm, and difficult to see on this scale (note that top and bottom graphs have different position and amplitude scales).

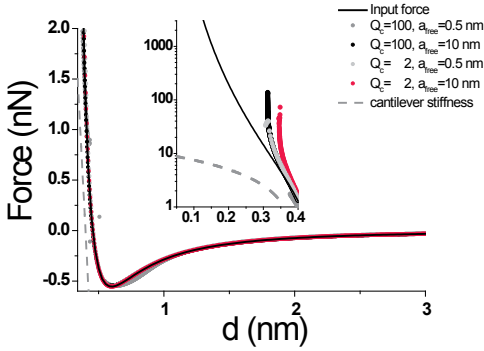


Figure 6.2 Force as a function of closest approach distance on a stiff sample

The derivative of the dotted line is equal to the cantilever stiffness. The reconstructed forces for 10 nm amplitudes are a good approximation of the real force until the sample stiffness is considerably larger than this. ($k_{ts}=k_c$ at $d \approx 0.4$ nm). There is a gap in the force profile of the simulated measurement with small amplitude and large quality factor. The inset shows the forces at close separations on a log scale.

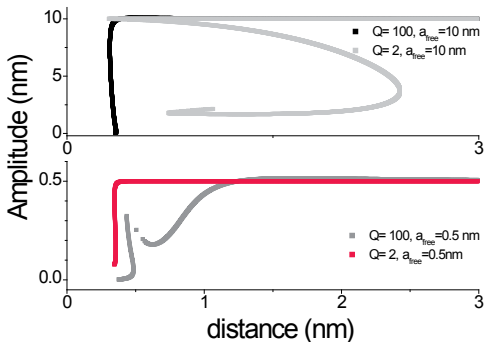


Figure 6.3 Amplitude as a function of closest approach distance on a stiff sample

Closest approach distance is defined here as the cantilever base distance z_0 minus the amplitude, plus the static bending. Quite unexpectedly, the amplitude curve bends inwards strongly for a low quality factor cantilever with larger amplitude. For both the smaller amplitude and the higher quality factor, this happens as well, but on a much smaller scale.

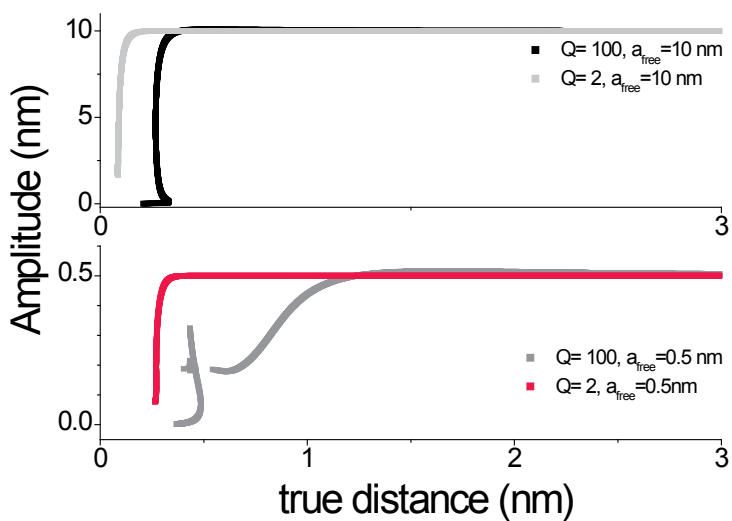
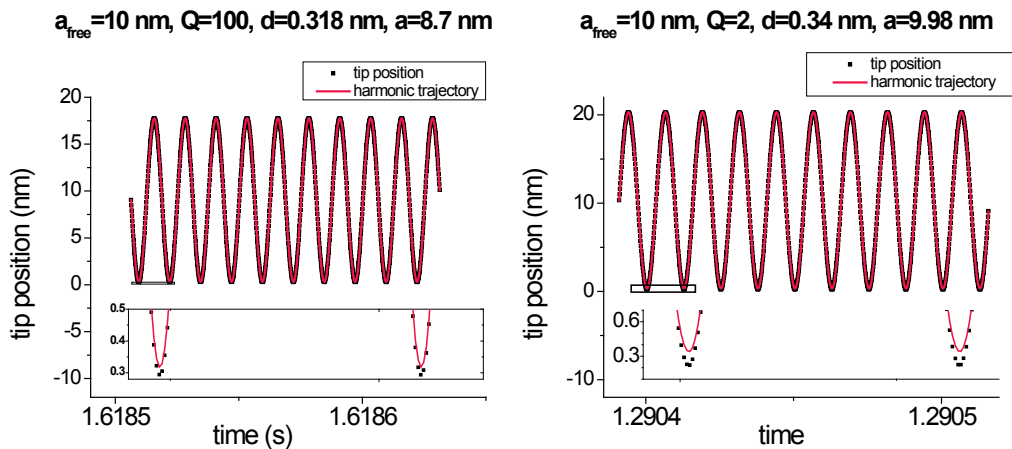


Figure 6.5 Amplitude as a function of closest approach distance as measured from time traces

Inward bending of the large amplitude, low Q factor curves has disappeared. For the large amplitude, low quality factor curve, the true closest approach distance is much closer than that estimated from the measured amplitude.

$a_{\text{free}}=10 \text{ nm}$, $Q=2$, $d=1.9 \text{ nm}$, $a=7.36 \text{ nm}$

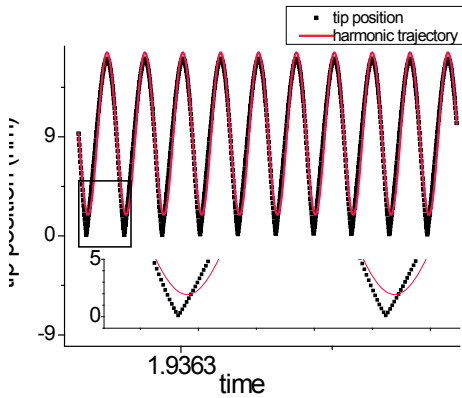


Figure 6.4 Simulated time traces of cantilevers

Black dots are the calculated positions during the simulation. The actual calculation of the trajectory was performed with 20 times the number of points shown here. The red lines represent the supposed position on the basis of measured amplitude and static bending. On average, the deviation is zero, but at the bottom of the swing, where the force gradient is high, deviations are substantial.

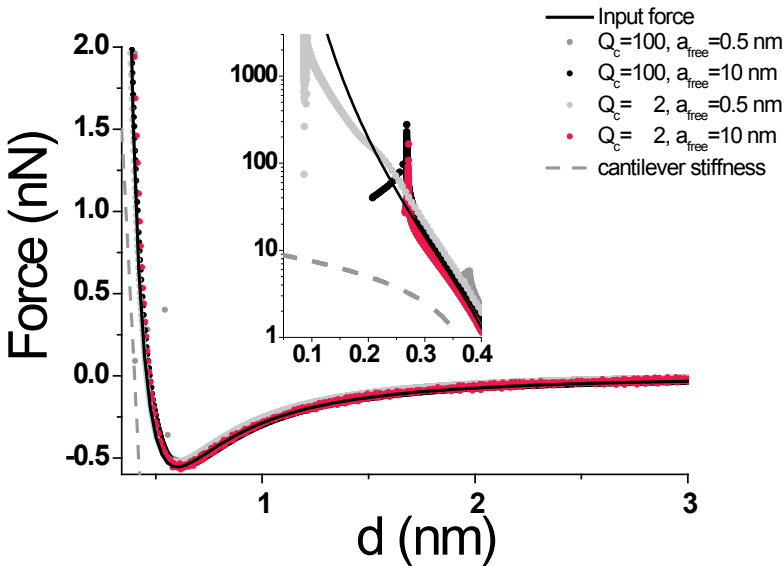


Figure 6.6 Force as a function of the true closest approach distance

For all four cases, but most clearly for the high-amplitude, low quality factor case, the fidelity of the reconstructed force has an extended range. To save disk space, the simulation that generated the full trajectory was started at $d=5 \text{ nm}$, instead of $d=30 \text{ nm}$. This causes the slight underestimation of the attractive forces at large separations as compared to figure 6.2.

Table 6.1 Parameters used for simulations of figure 6.7

Quality factor and resonance frequency are typical for use in aqueous solution.

	Standard cantilever	Small cantilever
Spring constant	2 N/m	2 N/m
Resonance frequency	30 kHz	1100 kHz
Drive frequency	29.5 kHz	1080 kHz
Quality factor	2	4
Lock-in time constant	0.5 ms	
Approach time	1 s	
Free amplitudes	0.2 nm; 2 nm; 10 nm	

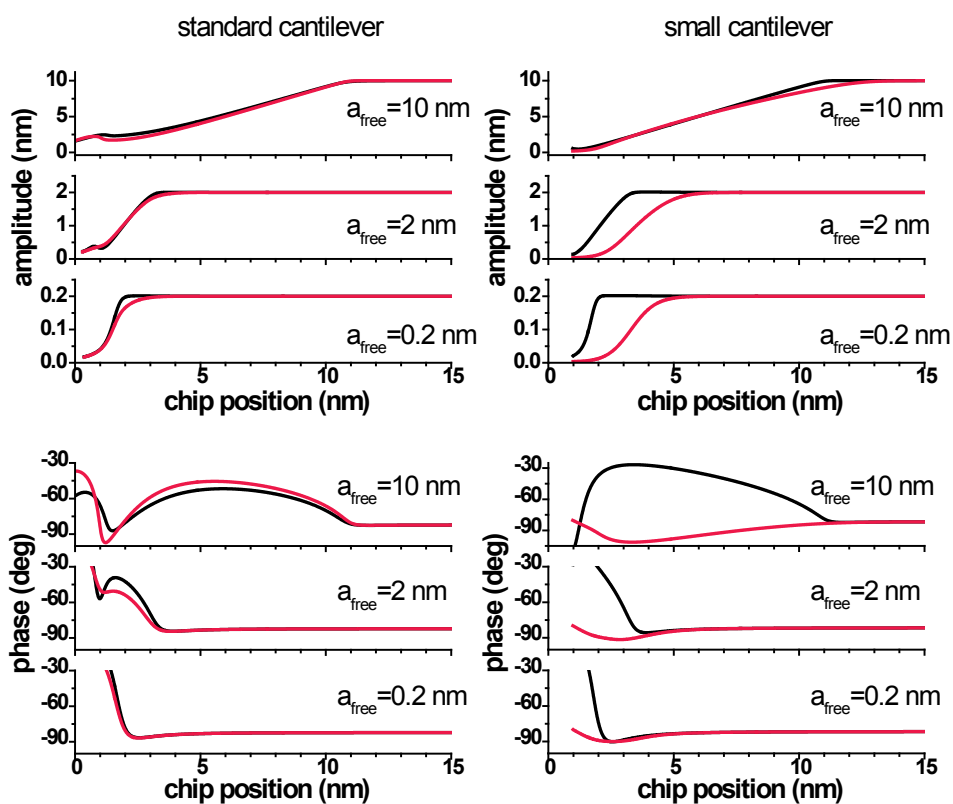


Figure 6.7 Effect of damping gradient on amplitude/phase versus distance profiles

Amplitude and phase behavior for two simulated cantilevers in the same Lennard-Jones force profile. Black lines: only conservative interactions. Red lines: with addition of an exponential damping profile. Left panels: a standard cantilever, right panels: a small cantilever, with low intrinsic damping.

The force reconstruction at 10 nm free amplitude is completely off below separations of about 2.5 nm. In this regime, the total damping increases by a factor of 5 within the bottom 1/3 part of an oscillation. Combined with the low intrinsic value of the quality factor, this makes that the long-range attractive part of the potential can have its effect on the oscillation unhampered, while the repulsive action is overshadowed by the damping, as illustrated by figure 6.9. This is why the force reconstruction only shows an increasing attractive force.

For all amplitudes, the damping at separations between 3 and 5 nm is reconstructed very well, demonstrating the large sensitivity of small AFM cantilevers for measuring damping effects.

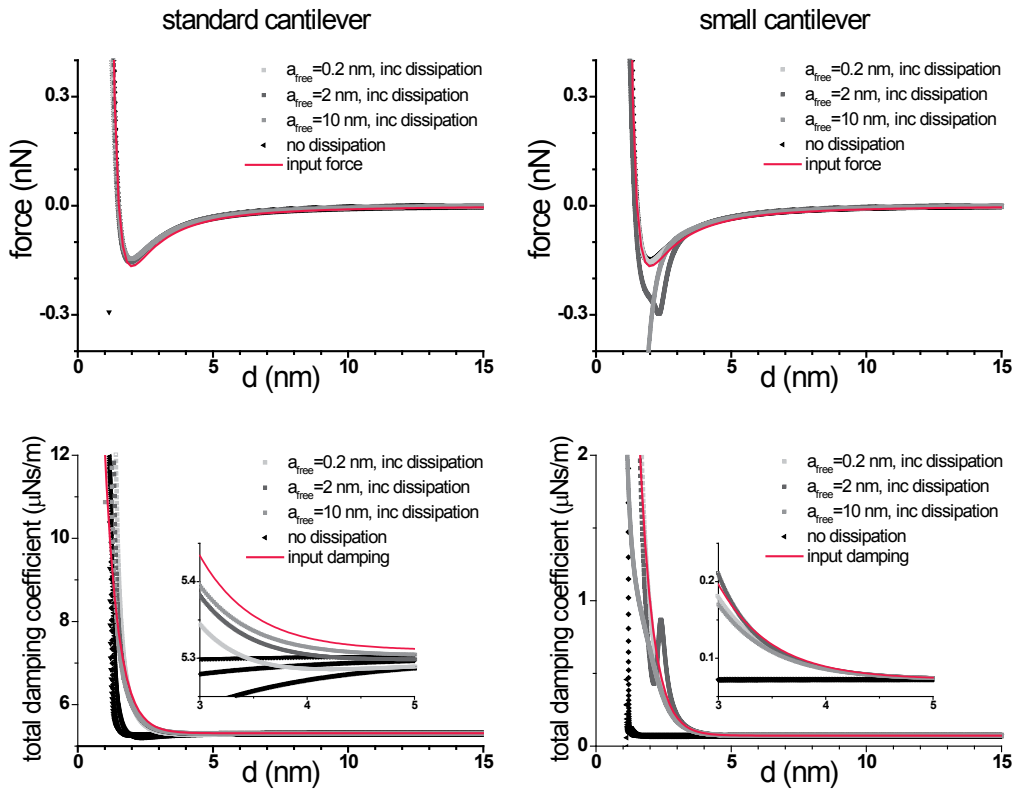


Figure 6.8 Effect of damping gradient on reconstructed force and damping profiles

Calculated force and damping profiles for the amplitude and phase profiles of figure 6.7. Insets in the bottom graphs are zoom-ins of the region between 3 and 5 nm separation. Although they are not always visible, all graphs contain three curves without dissipation, that were calculated with the same three amplitudes as the curves with dissipation included.

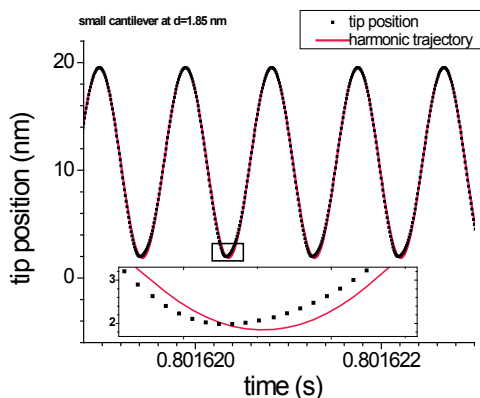


Figure 6.9 Time trace of a cantilever moving in a potential with a large damping gradient

The bottom part of the oscillation is truncated by the strong damping. As a result of this, the turnaround point occurs slightly earlier in time and further away from the surface than that of the harmonic trajectory.

6.3 Noise effects

The force inversion equations (6.3) and (6.4) are non-linear equations of the measured variables amplitude and phase. This means that the noise in the calculated force and damping will scale non-linearly with the measurement noise. In many experimental situations, AFM measurements are limited by fundamental noise sources such as the Brownian motion of the cantilever. To obtain the best signal-to-noise ratio, it is then important to choose experimental parameters such that the noise amplification by the force inversion algorithm is kept to a minimum. In this paragraph, a number of simulated experiments are presented that include the thermal position noise inherent in AFM force measurements. All instrument noise is neglected, and the Brownian motion is modeled as a random force with a constant spectral density of $\sqrt{4k_b T \gamma_c}$. These simulations serve as an illustration of how the force inversion equations influence signal-to-noise ratio.

Noise in force profiles

Figure 6.10 shows the results of a set of simulated AM-DFS experiments performed with two different cantilevers, one standard cantilever and a feasible miniature cantilever of the same spring constant. In each case the potential was a Lennard-Jones potential with length scale σ of 2 nm and energy scale ϵ of $5 \cdot 10^{-19}$ J. Other simulation parameters are summarized in table 6.2. The left and right panels of demonstrate the advantage of small cantilevers in force measurements. The amplitude noise for the smaller cantilever is a factor 3 lower. It is immediately clear from the bottom panels that smaller free amplitude experiments yield a better signal-to-noise ratio. This is surprising, since the absolute noises in the amplitude measurements, as well as the relative noises in the phase measurements, are roughly equal among the different free amplitudes.

To find the cause of this, we need to take a closer look at the force inversion equation. We then see that the third term in the integrand contains a derivative. Taking a derivative strongly increases the high-frequency noise in a dataset. There is a subsequent integration, that would normally smooth this noise again. But the third term is divided by a factor that is zero at the lower integration boundary and then goes up quickly. This means that the integration will not smoothen the noisy derivative, but instead the scatter of the first few points upwards from one measurement point determines the error at that point.

A more physical explanation of the noise amplification is obtained by noting that the third term in the inversion equation is the large amplitude approximation term. In this approximation the tip behavior is almost completely determined by interactions close to the turning points of the oscillation, where the tip spends only a small fraction of the oscillation period. Since the noise bandwidth is inversely proportional to measurement time, the effective noise bandwidth of a large amplitude measurement is much higher than the resonance frequency.

In general, a quantitative comparison of noise is complicated by the fact that it is the entire force profile that determines the outcome of an amplitude and phase measurement. A special case is when the tip-sample force is zero over the entire oscillation. In this case all the measured force is noise, and a comparison of the noise levels is straightforward. If the only source of noise is cantilever thermal motion, the expected noise in the force measurement can be calculated from the noise in the amplitude measurement using the cantilever transfer function:

$$\Delta F_{th} = \frac{\Delta a_{th}}{\sqrt{n_{av}}} * k_c \sqrt{\left(1 - \frac{\omega_d^2}{\omega_c^2}\right)^2 + \frac{\omega_d^2}{\omega_c^2 Q_c^2}} \quad (6.5)$$

Table 6.2 Parameters used for simulations of figure 6.10. Quality factor and resonance frequency are typical for use in aqueous solution.

	Standard cantilever	Small cantilever
Spring constant	40 N/m	40 N/m
Resonance frequency	100 kHz	2 MHz
Drive frequency	95 kHz	1950 kHz
Quality factor	10	15
Lock-in time constant	0.4 ms	
Approach time	2 s	
Free amplitudes	0.5 nm; 2 nm; 10 nm	

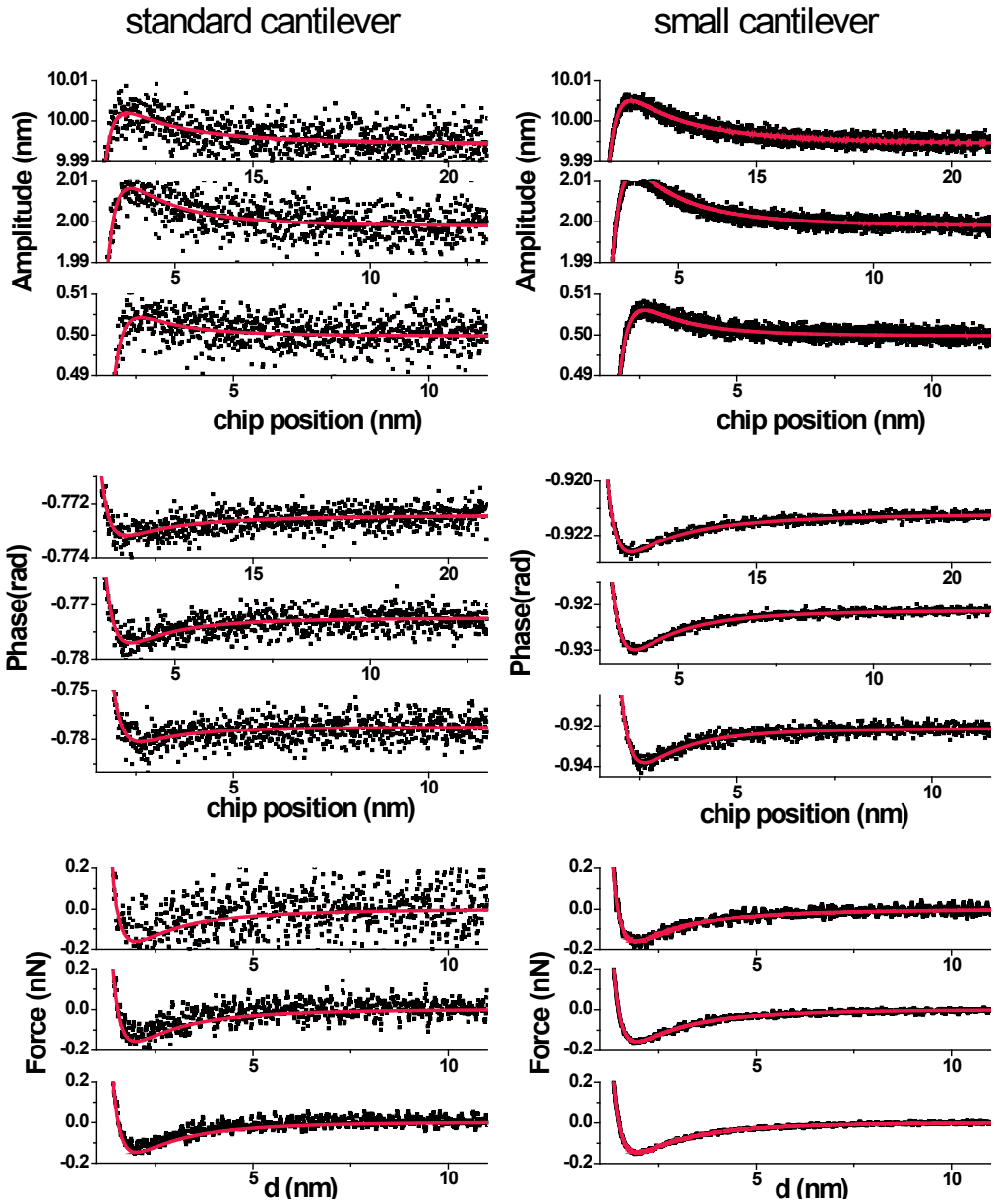


Figure 6.10 Simulated experimental results including thermal noise compared to noiseless simulations

Within each panel from top to bottom: free amplitude 10, 2 and 0.5 nm. Solid lines are the results of simulations that did not include a noise term. For calculating the force, amplitude and phase were smoothed with a 13 point first order Savitzky-Golay filter. Although the absolute noise in amplitude measurement, and relative noise in phase measurement are similar, noise in the calculated force is much smaller for smaller amplitudes.

The ratio of this value and the real force noise is the noise amplification. This is plotted in figure 6.11. The noise amplification depends on many parameters, but the results of many different simulations suggest that the free amplitude is by far the most important one. The noise is amplified most in the large amplitude term, which scales with the $3/2$ power of the amplitude, suggesting that the noise amplification should scale with the square root of the free amplitude. This is illustrated by the empirical fit function shown in figure 6.11.

In a force profile measurement, signal to noise ratio is also dependent on the relative size of the features in the force profile and the oscillation amplitude. For example, the attractive dip in the force profile of figure 6.10 causes a larger change in amplitude and phase shift (as compared to the noise level) for the 2 nm free amplitude case. Nevertheless, the force noise around the force minimum is still significantly larger than when a free amplitude of 0.5 nm is used.

Noise in damping profiles

Calculating damping profiles involves taking yet another derivative compared to calculating force profiles. It is therefore expected that the effect of noise amplification is even stronger in calculating damping profiles. The beneficial effect of smaller cantilevers on signal to noise ratio is expected to be much larger, too. Not only is the position noise less for the same bandwidth, the cantilever drag coefficient is much smaller as well, increasing the sensitivity for small changes in the damping coefficient at the tip.

Simulations with the same parameters as used for figures 6.7 and 6.8 were also performed with a thermal noise term included. The results of this are displayed in figure 6.12. For the standard cantilever, the measured damping from simulations with and without tip-sample damping only differs significantly in a region that is 0.5 nm wide. The difference in noise performance between small and standard cantilevers is immediately obvious.

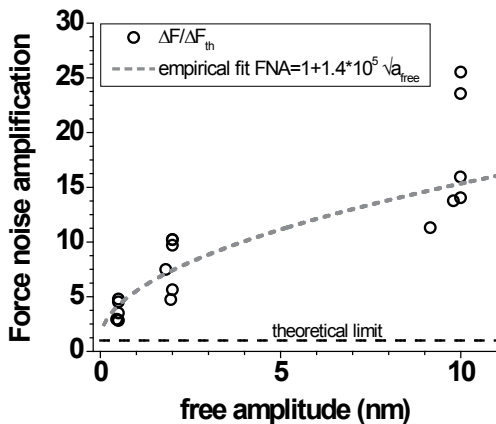


Figure 6.11 Force noise amplification plotted versus amplitude

Noise amplification was calculated by dividing the standard deviation of 500 points far away from the surface (where the force is much smaller than the force noise) by the noise expected on the basis of the amplitude standard deviation. An empirical fit of a square root function is shown for comparison. Data shown is calculated from the data shown in figure 6.11 and a second dataset calculated with the same parameters.

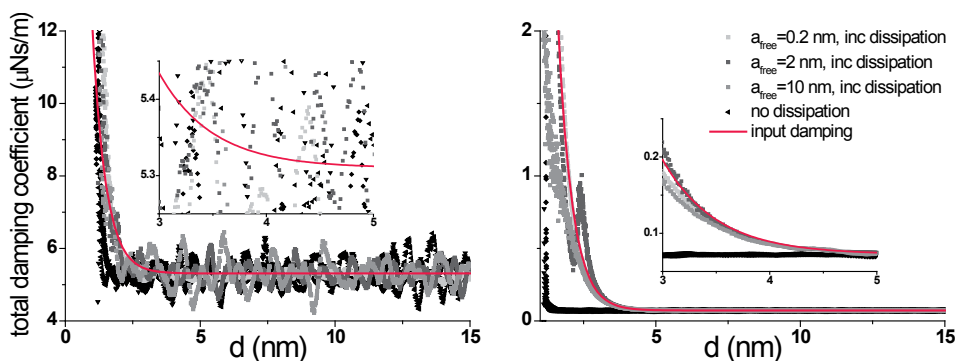


Figure 6.12 Effect of noise on calculated damping profiles

As the noise scales with the cantilever's free damping constant, the noise level is dramatically lower when a small cantilever (right) is used.

When there is no variation of the damping coefficient over the cantilever oscillation, the damping coefficient is directly proportional to the amplitude, and the relative noise levels in the amplitude and damping coefficient should be proportional to each other. The top graph in figure 6.13 shows that this is not at all the case. A clear indication that numerical differentiation is a major source of added noise, is found in the stronger noise amplification for a group of simulations that used smaller distances dz between measurement points. The time for the total measurement was adjusted such that the time per point was the same. The amplification of noise by numerical differentiation is linear in the distance between points, but the ratio of noise amplification factors here is far larger than the ratio of spatial sampling frequencies. Also, a strong amplitude dependence of the noise amplification is present. As shown in the bottom graph, a scaling of the noise by a factor $(a/dz)^{3/2}$ yields a fairly constant number. The physical meaning of this scaling factor is at present not quite clear. The stronger dependence on amplitude of the noise scaling (as compared to noise scaling of the force) may reflect the fact that the damping function Θ_{AM} depends more strongly on the measured amplitude than the frequency shift Ω_{AM} when the driving frequency is close to the resonance frequency, as was the case in all the simulations presented here.

In the current implementation of the force inversion algorithm, all calculus (integrating, differentiating) is done numerically. In principle, it is possible to fit a function to the amplitude and phase versus distance profiles, and do the calculus analytically. This circumvents the generation of noise by numerical differentiation, and its subsequent amplification. But it should be kept in mind that many deviations of the fitted profiles from the “true” amplitude and phase behavior are amplified in the same way as the noise.

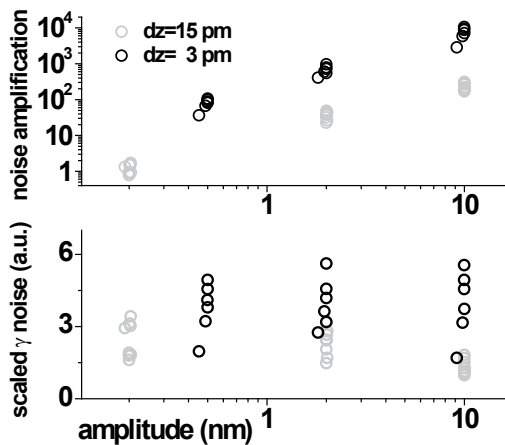


Figure 6.13 Noise scaling in the damping coefficient

The top graph shows the ratio of relative noises in amplitude and damping coefficient for datasets with two different distances between the points. Separation of these two sets shows that the numerical differentiation is a major contributor to the noise. Bottom graph shows the relative noise level scaled by $(\text{amplitude} / \text{point distance})^{3/2}$. In this scaling, all noise levels fall within the same order of magnitude.

6.4 Conclusions

In this chapter we investigated a number of artifacts that can lead to deviations of the reconstructed force in an AM-DFS experiment from the force that was actually measured. Numerical simulations using realistic experimental conditions were used to reliably relate input and output forces. We found that force profiles with gradients on the order of the cantilever stiffness can be reliably reconstructed, even though the force inversion method is based on the assumption that the gradient is much smaller. It was found that by using the peak-to-peak amplitude as a measure of oscillation amplitude, the influence of non-sinusoidal motion of the tip on the accuracy of the reconstruction is greatly diminished. Strong gradients in the amount of damping can lead to misinterpretation of the conservative force, and vice versa. Small cantilevers, with their smaller intrinsic damping coefficients, are more sensitive to changes in the damping coefficient, which leads to a diminished coupling of the conservative force into the reconstructed damping, but enhanced effects of the damping on the reconstructed force. Small cantilevers also measure conservative forces and damping coefficients with a higher signal-to-noise ratio, with the improvement being more pronounced in the measurement of dissipation. The noise in the reconstructed force increases above the fundamental limit with the square root of the oscillation amplitude of the cantilever, even when the only source of noise is the thermal oscillation of the cantilever. Noise in the damping coefficient scales even with the $3/2$ power of amplitude. This scaling favors the use of small oscillation amplitudes in force measurements.

7 Measuring hydrophobic interactions with three-dimensional nanometer resolution

7.1 Abstract

We investigate forces between two nanoscopic hydrophobic surfaces under pure water. One of the surfaces is a multiwall carbon nanotube AFM tip with a radius of curvature of 8.5 nm, the other a hydrophobic domain in a mixed self-assembled monolayer. The monolayer has domains consisting of hydrophobic dodecanethiol, surrounded by domains of shorter alkanethiols with hydrophilic endgroups. On samples with larger hydrophobic domains (30-80 nm), nanobubbles cover the surface when immersed in water. On samples with smaller domains (10-50 nm), nanobubble formation is greatly diminished, and it is possible to do force measurements that are unaffected by nanobubbles. Using dynamic AFM at a frequency of 1.16 Mhz, which is at least 20 times higher than commonly used in liquid, force-distance profiles are measured with high spatial resolution. On hydrophobic domains we find an attractive hydration force from distances of 5 nm and closer, that reaches a maximum of 0.1 nN at a separation of 1.5 nm. Surprisingly, we see a smooth transition to repulsive forces at closer separations. Attractive forces are well fitted by an exponential decay with 0.6 nm decay length, and we find no evidence for a long-range (>5nm) attractive force on these samples.

7.2 Introduction

Hydration forces

In many processes in nature and technology, hydration forces are believed to play an important role [1]. Examples include self-assembly of micelles, vesicles, and membranes [2], folding of proteins [3], the properties of zeolites and clays, stabilization of colloidal solutions, lubrication, and microfluidic transport. Hydration forces are the forces between particles or surfaces in aqueous solution that exist because of their specific interaction with the water molecules, and that cannot be explained by Derjaguin-Landau-Verwey-Overbeek (DLVO) theory [1]. This partly negative definition reflects the absence of a complete and consistent theory of the nature and origin of hydration forces. Generally, hydration forces are separated in two classes: repulsive hydrophilic or structural forces, and attractive hydrophobic forces. In the past three decades,

numerous experiments have been conducted to determine the distance dependence of these forces. Direct force measurements have been done with either the Surface Forces Apparatus (SFA) or Atomic Force Microscope (AFM). The hydrophilic repulsive force is generally considered to be short, decaying exponentially with typical lengths of 0.2-1.4 nm [1,5,6]. In contrast, the experimental body of work on the range of the hydrophobic force does not converge so easily, and numbers ranging from a few nm to hundreds of nm are proposed [7-9]. Recent overviews by Christenson [10] and Meyer [11] summarize direct measurements of the hydrophobic force and some of the artifacts that have led to the overestimation of its range. Even when these artifacts are circumvented, the hydrophobic force is still expected to be the dominant interaction between hydrophobic surfaces up to distances of 10 nm. Many surfaces where the hydrophobic force plays a key role, in particular proteins and biological membranes, are heterogeneous on this length scale. Surprisingly, the influence of heterogeneity on hydration forces has not been investigated experimentally. Although the microscopic theory of the hydrophobic effect has made significant advances in recent years [13], to our knowledge only one - very recent - theoretical investigation of hydration forces between nanoscale patterned surfaces is reported in the literature [14].

Nanobubbles

One complicating factor in many force measurements on hydrophobic surfaces is the formation of nanoscopic features, usually referred to as nanobubbles. Nanobubbles were first introduced as explanation for long-range jumps of attractive forces seen in Surface-Forces Apparatus measurements by Parker *et al* [144]. Since then, a great number of SFA and AFM force measurements, as well as AFM images have shown evidence of nanobubbles [145]. The 2003 review of Attard [146] gives a good overview of these. More recent work by Zhang *et al* [147] shows a systematic investigation of nanobubble properties under different circumstances, and Agrawal *et al* [148] have demonstrated control over the size and position of bubbles by micropatterning of polymers. Smeets *et al* [149] find these bubbles inside solid-state nanopores. Although the evidence for their existence by now is overwhelming, the origin of the stability of nanobubbles is still unclear. From the point of view of thermodynamics, the high Laplace pressure inside the bubbles should drive them to dissolve into the liquid within milliseconds. In AFM measurements, they are seen to be stationary over minutes or even hours by many of the aforementioned authors. Meyer *et al* [11] report that the formation of bubbles is triggered by capillary cavitation after contact in their SFA experiment, and that they disappear in a few seconds when the surfaces are separated. All these studies of nanobubbles involve inherently invasive techniques, since they bring two surfaces close together. Often, it is difficult to determine whether the bubbles pre-existed on the surface or were generated by the proximity of the second surface, either by cavitation upon separation or spontaneously by spinodal dewetting. Zhang and co-workers [150] conclude from a combination of AFM measurements and infrared spectroscopy that CO₂ nanobubbles can preexist on hydrophobic surfaces if these were covered with ethanol before being exposed to

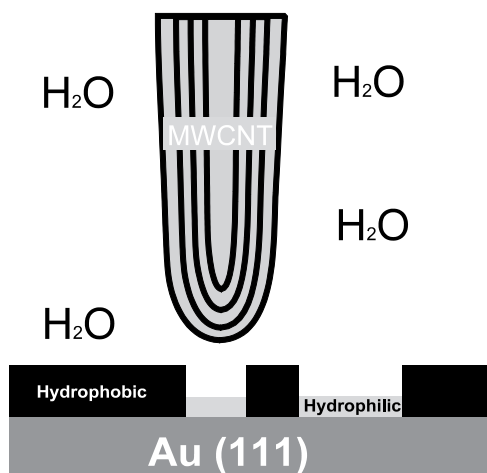


Figure 7.1 Schematic side view of the sample

Hydrophilic domains, in light grey, and hydrophobic domains, in black, of monolayers are grafted to a gold (111) surface, depicted in dark grey. The nanotube tip and the sample are immersed in water.

water. These bubbles have a thickness less than 80 nm but radii of curvature of at least 2 μm . Recent experiments using x-ray [151] and neutron [152] reflectivity measurements on single surfaces provide strong evidence against the pre-existence of nanobubbles at the interface between water and methyl-terminated SAMs on quartz and silicon substrates. Instead, the authors of these papers propose the existence of a homogeneous depletion layer at the SAM/water interface, with a thickness comparable to one molecular diameter. Using smooth surfaces covered by defect-free SAMs that have no pinning sites for bubbles, and a non-invasive measurement technique are mentioned as important prerequisites for attaining this result. But to do a measurement of the forces between two surfaces, invasive methods are inevitable. Studying the effects of nanoscale heterogeneity on surface forces therefore requires a technique that either does not generate nanobubbles, or circumvents them.

In this study, we present a surface with nanoscale hydrophilic and hydrophobic patches. With the proper method of preparation, the surface shows only a sparse coverage of nanobubbles even in water that has not been degassed. We then use high-frequency dynamic AFM force-volume imaging with high aspect-ratio hydrophobic carbon nanotube tips to measure simultaneously both surface topography and force-distance behavior with nanometer resolution in all three spatial dimensions. In this way, we can directly distinguish force profiles that are influenced by nanobubbles, and exclude them from our analysis. These techniques allow us to present the first spatially resolved measurements of hydration forces on nanoscale heterogeneous samples.

7.3 Experimental methods

7.3.1 Self-assembled monolayers (SAMs)

Ternary self-assembled monolayers were fabricated following the method of Phong *et al* [153], on substrates of gold (111). This substrate was made by sputter deposition of gold onto freshly cleaved 2 mm diameter mica disks (SPI supplies, V4 grade) in a procedure similar to that published by Kawasaki *et al* [154]. This leads to atomically flat terraces of 100 to 500 nm in size. Immediately after deposition, the substrates were immersed in 400 μ l of alkanethiol solution. This solution was prepared by dissolving 0.25 mM of 2-aminoethanethiol (AET) (cysteamine hydrochloride, Fluka), 0.25 mM of sodium 2-mercaptoethanesulfonate (MES)(Fluka) and 0.5 mM of dodecanethiol (Aldrich) in pure ethanol (BioSolve). Incubation time for self-assembly was between 16 and 36 hours at room temperature. To remove any physisorbed alkanethiols after incubation, the samples were soaked in pure ethanol for 20 minutes, rinsed with ethanol and propanol, and dried in a dry nitrogen flow. Electrochemical characterization (not shown) of these surfaces showed two distinct reductive desorption peaks, at -0.7 and -1.1V (vs. Ag/AgCl). The sharpness of these peaks indicates phase separation between hydrophilic and hydrophobic monolayers [153].

7.3.2 Atomic Force Microscopy

Cantilevers and carbon nanotube tips

For characterizing the surfaces, Olympus AC 240 TS (nominally 2 N/m, silicon tip) cantilevers were used. For part of the imaging, and all of the force measurements in liquid, custom made miniature cantilevers were used. Focused Ion Beam (FIB) milling was used to cut miniature

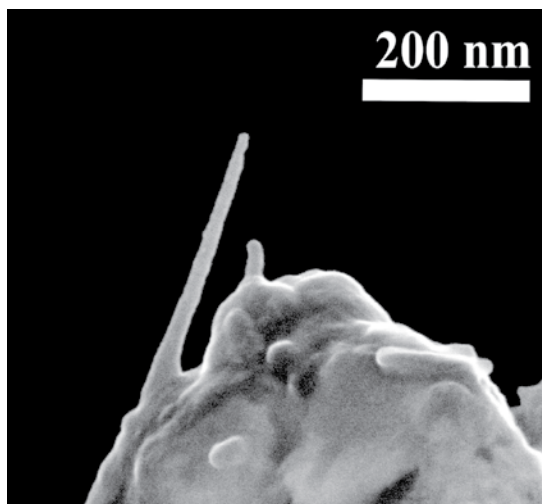


Figure 7.2 Nanotube tip used in the measurement

The image was made at a tilt angle of 45°, with the tilt axis horizontal in this picture. The tip radius was estimated to be 8.5 +/- 1.0 nm.

AFM cantilevers out of commercially available cantilever chips. The cantilever used in the force measurements described here was 17.3 μm in length and 1.4 μm in width. It had a resonance frequency of 1.6 Mhz in air, and 1.16 MHz in water. The spring constant, as determined with the Sader plan view method [155] was 2.1 ± 0.2 N/m. At the end of the cantilever, ion beam assisted deposition of platinum was used to deposit a pedestal for mounting a multiwall carbon nanotube (Ros1, Rosseter Holdings Ltd.) as a tip. This mounting was done inside a scanning electron microscope (SEM), equipped with a nanomanipulator, similar to the method used by Jarvis *et al* [37]. This allows control over the mounting angle, but since the SEM only gives a two-dimensional image, it is difficult to make sure the nanotube is perpendicular to the surface in all directions. The length of the nanotube can be adjusted by shortening it with voltage pulses inside the SEM vacuum of 10^{-6} mbar. Previous work in our group [156], by force distance measurements of the tips on a hydrophilic self assembled monolayer on a monocrystalline gold substrate, has established that multiwall nanotubes shortened in this way have either (hydrophobic) amorphous carbon or a closed (hydrophobic) graphitic cap at the end. A hydrophilic carboxylic acid group will form at the end only when the nanotube is shortened in ambient conditions. An image of the tip, taken after the measurements, is shown in figure 7.2. The nanotube makes an angle of 20 degrees with the surface normal. The resulting spring constant of the nanotube in the normal direction is estimated to be 10-100 N/m. This introduces a systematic error in the effective spring constant of the tip that is within the uncertainty of ± 0.2 N/m already present in the thermal calibration method.

Microscope

A home-built atomic force microscope, suitable for using small cantilevers, was used for all AFM measurements. Details of the instrument are described in chapters 3 and 4. The most important feature of this microscope is the optical lever deflection detection system. It has a 1 μm wide laser spot size, 7 Mhz bandwidth and a detection noise of 15 fm/ $\sqrt{\text{Hz}}$. This allows the use of smaller cantilevers than those used in commercial instruments, while still being thermal noise limited in the detection. The AFM is of the sample-scanning type. The sample is mounted on the piezo scanning element via a sample holder made of PEEK (an inert plastic), that sticks into the fluid cell in which the experiments are performed. This fluid cell (depicted in figure 4.2) exposes only inert materials to the fluid and is thoroughly cleaned before and after each experiment. The tip is electrically grounded. Control of the microscope is done with CAMERA electronics and software (Leiden Probe Microscopy B.V.).

Force-distance measurements

To probe the interaction between the carbon nanotube tip and the inhomogeneous monolayer surface, force-distance measurements were made on a regularly spaced grid of 100 x 100 nm area, with a pixel size of 0.4 nm. The force curves were acquired at a rate of 25 curves/second.

The 3D feedback system described in chapter 4 made sure the surface stayed within the range of the tip without exerting forces that were higher than desired. Oscillation amplitudes used for the measurements were varied between 1-3 nm, while the sizes of the force-distance cycles were varied in a range between 20 nm to 2 nm.

To avoid snap-in and to increase force sensitivity, a dynamic force-distance measurement technique was used. The cantilever is driven at a constant frequency - close to its resonance frequency- and with a constant driving amplitude. The response amplitude and phase shift of the cantilever oscillation are recorded while the tip is approached to and retracted from the surface. This dynamic technique was used because of the importance of a high signal-to-noise ratio in the detection of the motion of the stiff cantilevers. Because of drift, 1/f noise in the photodiode amplifiers, and acoustic vibrations the noise around zero frequency is larger than around the cantilever resonance. The quality factor of the stiffer cantilevers is significantly larger than 1, so the sensitivity to forces around resonance is higher. Furthermore, dynamic measurements can give access to information that is not available in static measurements, such as the dissipative force. Until recently, quantitative evaluation of forces measured in amplitude modulation dynamic mode was not possible. A newly developed method, based on the Sader-Jarvis formula for frequency modulation AFM [105], was used to quantify the measured forces. Details of this method are described in chapters 5 and 6, but the principle is explained in the following paragraph.

We measure the amplitude a and phase angle φ of the cantilever motion, as a function of the tip-sample closest approach distance d . Based on the transfer function of a driven, damped harmonic oscillator, we can calculate the resonance frequency ω_0 and quality factor Q_c of the cantilever in the presence of a tip-sample interaction using $\omega_0 = \omega_d (1 + \cos(\varphi) * a_d/a)^{1/2}$ and $Q = -a(1 + \cos(\varphi) * a_d/a)^{1/2} / (\sin(\varphi) * a_d)$. Here ω_d and a_d are the frequency and amplitude with which the cantilever base is excited. We can then calculate the relative frequency shift $\Omega(d) = (\omega_0(d) - \omega_c) / \omega_c$ and the (oscillation averaged) sample-induced damping coefficient $\gamma_s = \omega_0(d) * Q_c / (\omega_c * Q(d))$, if the free resonance frequency ω_c and quality factor Q_c of the cantilever are known. With the relative frequency shift, we can use formula 16a from ref. [105] to find the conservative tip-sample force F_{tc} :

$$F_{tc}(d) = 2k_c \int_d^{\infty} \left(\left(1 + \frac{a(u)^{1/2}}{8\sqrt{\pi(u-d)}} \right) \Omega_{AM}(u) - \frac{a(u)^{1/2}}{\sqrt{2(u-d)}} \frac{d\Omega_{AM}(u)}{du} \right) du$$

7.4 Results

7.4.1 Bubbles and domain sizes

To verify the sample preparation, and inspect domain sizes, dynamic mode imaging was performed in air and in pure water. Two different sets of SAM samples can be distinguished. A number of samples incubated for 16-24 hours showed an even coverage with SAM domains of 30-80 nm in diameter (figure 7.3A). When these samples were immersed in water, a large number of nanobubbles could be seen on the surface (figure 7.3B). These bubbles were very stable and could not be moved by imaging with a large interaction force. In some cases, it was possible to either deform or punch through the bubble at its highest point when the amplitude setpoint was decreased (larger interaction force). This deformation was completely reversible. Another set of samples was incubated for a longer time (approximately 40 hours). This resulted in a distribution of molecules in smaller domains, 10-50 nm, and a higher relative surface coverage of dodecane-thiol. Topographs of such a sample can be seen in figure 7.4.

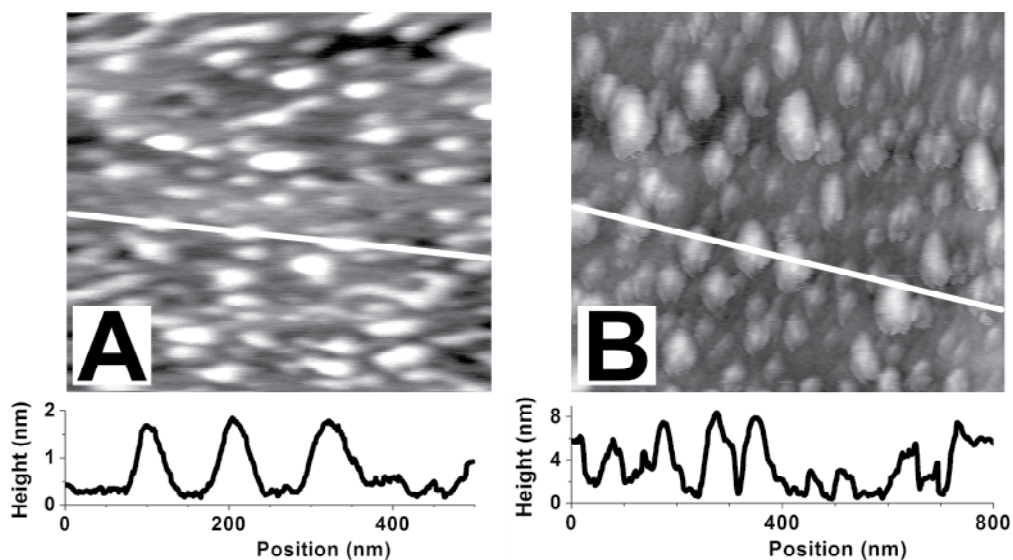


Figure 7.3 Nanobubbles on a mixed SAM with large domains

A: AFM topograph and cross-section of a SAM sample that was immersed for 16 hours, 500 nm image width. The image was acquired by using intermittent-contact mode in air with a standard silicon tip. The domain sizes are 30-80 nm. The image is slightly compressed in the vertical direction because of drift and piezo creep. **B:** AFM intermittent contact mode topograph and cross section of a similar sample in pure water, 800 nm image width. This image was made with a miniature cantilever and nanotube tip. Nanobubbles completely cover the surface. Note the 4 times larger height scale in the cross section and image as compared to A)

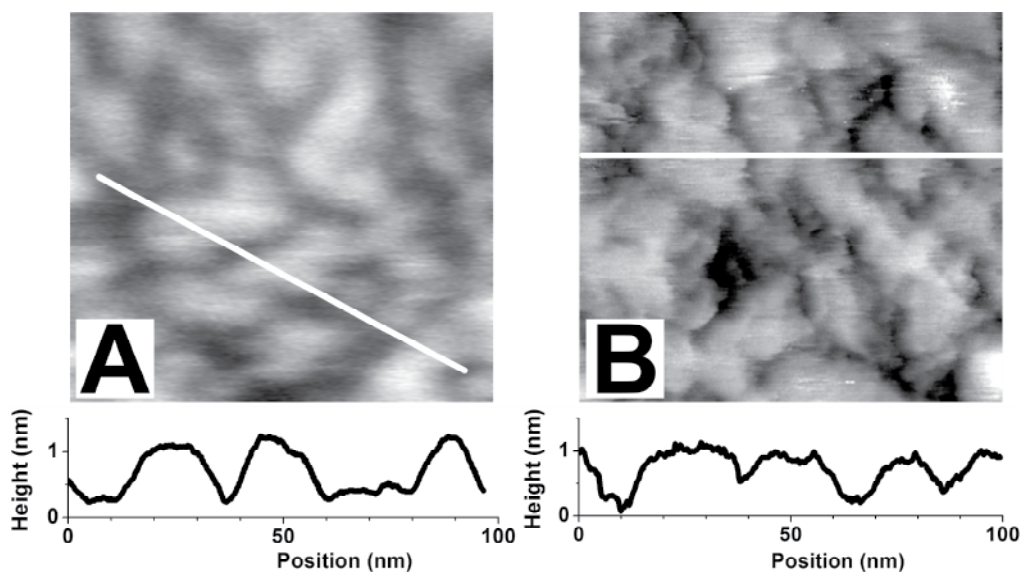


Figure 7.4 Topography of a SAM sample with small domains in air and water

A: AFM topography and cross section of a SAM sample that was immersed for 40 hours, 100 nm image width. The image was acquired by using intermittent-contact mode in air with a standard silicon tip. The domain sizes are 10-50 nm. This image was smoothed to remove the influence of an external noise source **B:** Topography and cross-section of the same surface as in A), under pure water, 100 nm image width. This image was measured with a miniature cantilever and nanotube tip. A 2nm high nanobubble is visible in the bottom right corner of the image, and two smaller 'bubbles' can also be distinguished. The smallest hydrophilic gaps between hydrophobic domains seem less deep because of tip convolution.

The effect of immersion time on the surface morphology of this SAM system was investigated by Phong *et al* [157]. They saw an effect only at total solution thiol concentrations of less than $3 \cdot 10^{-4}$ M, where domain sizes grew with time, as can be expected. For concentrations of $1 \cdot 10^{-3}$ M, as used here, they find that the surface morphology is determined by absorption kinetics in the first few seconds of incubation and stable for at least 8 days. It is therefore unlikely that the immersion time was the determining factor for the difference in domain size. A possible explanation is a difference in the temperature of the thiol solution at the time of immersion. However, this temperature was not recorded. No noticeable difference was found in the morphology of the gold films used as substrates, and all other procedures followed in making the samples were the same. The samples with smaller domains showed almost no nanobubble formation. A few bubble-like features were seen, but they were significantly smaller and could be removed with repetitive scanning at low amplitude setpoint values. This type of sample was used for force-volume measurements.

7.4.2 Force curves

An example of typical amplitude and phase versus distance curves, measured on top of a hydrophobic domain can be seen in figure 7.5, together with corresponding force and dissipation curves, obtained as described in the Experimental section and chapter 5. To confirm that a force profile such as measured here does not lead to large deviations from a harmonic trajectory, force and dissipation profiles were fitted to the reconstructed data, and a simulation such as described in chapter 6 was done using these profiles and the experimental parameters. The amplitude and phase calculated with this simulation were equal to the measured amplitude and phase to well within the experimental error.

Throughout this chapter we will show only the approach part of the force-distance cycles. Retract curves were recorded as well, and showed very similar features. Amplitude and phase are plotted versus sample displacement, while the force and dissipation are plotted versus the tip-sample closest approach distance, which differs from the sample displacement by an offset (one single value for the entire curve) plus the oscillation amplitude plus the cantilever static deflection (both variable during a curve). The static deflection was measured to be smaller than 0.1 nm in this experiment, but with a poor signal-to-noise ratio. Therefore it is not used in any calculation and assumed to be zero. The offset is chosen such that the onset of repulsive force occurs at zero.

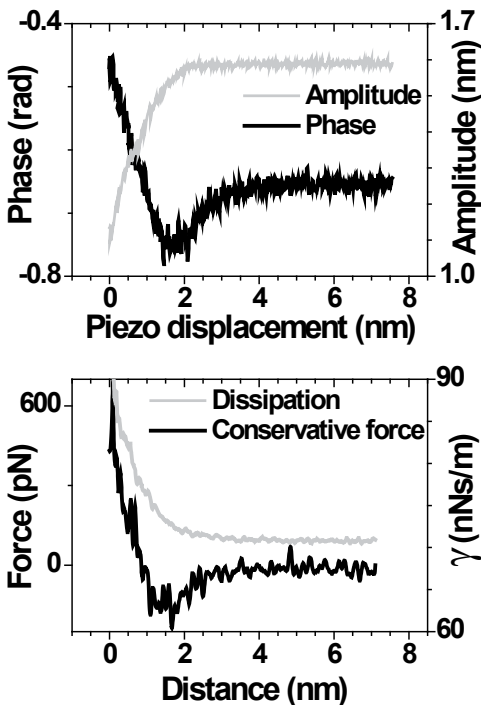


Figure 7.5 Single measurement of amplitude and phase with calculated force and dissipation

Example of a single amplitude and phase measurement and corresponding force and dissipation versus distance curves. The origins of the distance and displacement axes are arbitrary here.

distance. The maximum force in this measurement is around 600 pN, at an amplitude reduction of around 30%. Higher forces could be applied during force measurements or imaging without instabilities, but the force reconstruction was not reliable, since the surface effectively acts as a hard wall. This makes the necessary differentiation with respect to closest approach distance impossible.

The dissipation is expressed as a (generalized) viscous damping coefficient. Although the physical origin of the energy dissipation may not be viscous in nature, we can always define an effective damping coefficient $\gamma_{eff}(d) = \gamma_c + \gamma_s(d)$, with γ_c the damping coefficient of the free cantilever, to account for all the energy dissipated during the oscillation [105,127]. Other authors [118,129] have used the energy lost per oscillation cycle as a measure for the dissipation. These two quantities can be related to each other via $\Delta E = \pi \omega_d a_d \gamma_{eff}$. The effective damping coefficient is independent of experimental parameters like the driving frequency or free amplitude, which allows an easier comparison between experiments. The damping coefficient in the absence of any tip-sample interaction has a value of $\gamma_c = k_c / \omega_c Q_c = 71$ nNs/m for the miniature cantilever. This is much smaller than for standard AFM cantilevers, that have drag coefficients of $1 \mu\text{Ns/m}$ or higher. Usually, the squeeze damping that occurs due to the fluid between the cantilever and the sample increases this drag coefficient further. This effect becomes significant as the cantilever-sample distance becomes similar to the cantilever width [107]. Because of the high-aspect ratio nanotube tip and the narrow width of the cantilever no significant cantilever squeeze damping is observed in our experiments.

The noise in the amplitude measurement is 5.6 pm RMS, which is only 40% above the expected magnitude of the Brownian motion of the cantilever in the measurement bandwidth (lock-in time constant 50 μs). The RMS phase noise is 0.42 degrees, a factor three higher than the Brownian motion limit. Noise in the force calculated from this data is much higher than the thermal limit. This noise amplification is a general feature of the force inversion equation, and is caused by the use of a derivative and the non-linear dependence on the amplitude, see also chapter 6. The addition of an 11-point smoothing in the calculation reduces the noise to 16 pN RMS, still a factor 9 above the thermal limit. This smoothing is applied in all force calculations, and does not significantly lower the distance resolution of the measurement, since the data is acquired at 50 kS/s, and therefore oversamples the lock-in output.

Using the amplitude-distance curves, we can reconstruct the topography of the sample. In tapping mode AFM, topography is measured by adjusting the sample position with a feedback system to keep the amplitude constant. By selecting the points in each dynamic force-distance curve with relative amplitude $a = 0.95 * a_0$, we can reconstruct a topographic image as would

have been measured with normal tapping mode with a setpoint of 5% amplitude reduction. Such an image is displayed in figure 7.6. This topography has features similar to the topography measured in normal tapping mode (figure 7.4B). The height difference between hydrophilic and hydrophobic domains is 1.2 ± 0.2 nm. The height difference expected from the chain length of the thiols, assuming all molecules have the same tilt angle, is 0.99 nm. A number of brighter white spots, presumably nanobubbles, appear on the surface. On these spots, force curves were very irreproducible, demonstrating snap-in in some cases, and a total absence of attractive forces in others.

Curve averaging

The noise amplification prevents a detailed comparison of single force curves on adjacent locations, since the differences are often drowned in the noise. Because the spacing of the force curves (0.4 nm) is much smaller than the tip radius (8.5 nm), it is very well possible to align and average a small number of adjacent curves without introducing artifacts. An attempt was made to automate the averaging procedure for a large amount of force curves, but this was not successful. Small variations in the distance, caused by noise, drift and feedback error, led to misalignment of the curves and an underestimate of both attractive and repulsive forces. Therefore, one hydrophilic and one hydrophobic domain were selected, and for each of these 14 curves were taken from a 1.5×2.5 nm area in the center of the domain and were averaged. In the averaging procedure, aligning the curves was done by the same criterion as the reconstruction of the topography, i.e. by assuming that the 5% percent amplitude reduction points of the curves occurred at the same distance from the surface. These averaged curves are presented in figure 7.7.

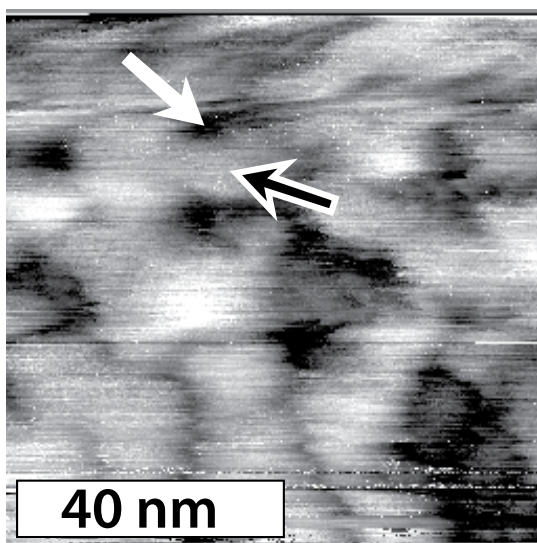


Figure 7.6 Topograph reconstructed from amplitude-distance measurements

Topography reconstructed from 256×256 dissipation-distance profiles, 100×100 nm image size, 2 nm color scale. Vertical piezo cycle distance was varied between 20 nm (topmost part of the image) and 2 nm (entire bottom half). Brightest white spots are approximately 2 nm higher than the surrounding hydrophobic domains, and are designated to be 'nanobubbles'. The white and red arrows indicate respectively the hydrophilic and hydrophobic regions where the averaged force curves of figure 7.7, figure 7.8, and figure 7.10 were taken.

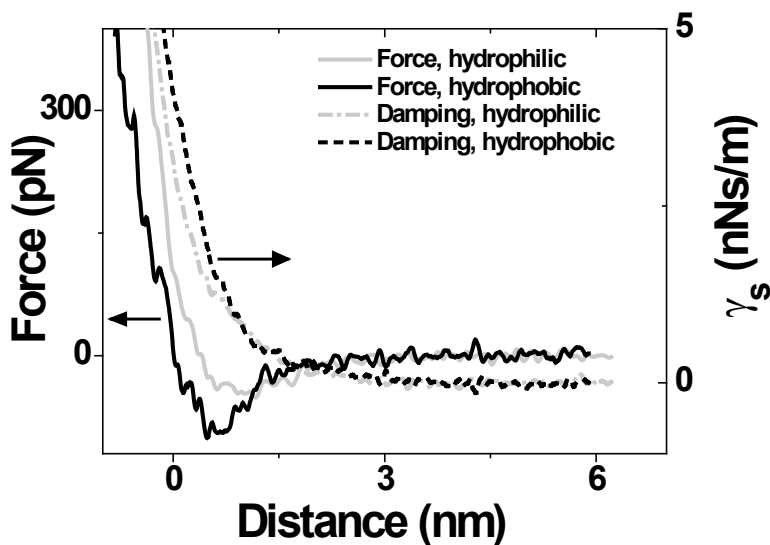


Figure 7.7 Averaged forces and damping coefficients

Force and damping versus distance on two neighboring patches with different hydrophobicity. Each curve is an average of 14 curves measured on different locations on the same patch. Curves were aligned such that the zero of distance corresponds to the point where the amplitude reduction is 5% of the free amplitude.

The first result visible in figure 7.7 is that the damping coefficients are very similar on the hydrophilic and hydrophobic regions. The damping coefficient remains constant from macroscopic separation distances until the tip is approximately 1 nm from the surface. Below this distance it increases sharply. It is important to notice that the damping (averaged over one period of oscillation) increases already before the closest approach distance comes into the repulsive force region. In the repulsive region, we start to see a different damping behavior on the two patches: the damping increases more steeply on the hydrophilic domain. The classical Raleigh equation predicts that the viscous drag on a spherical tip with radius R_{tip} moving perpendicular to a wall in a fluid of viscosity η increases as $6\pi\eta R_{tip}^2/d$ due to tip squeeze damping. Numerical simulations of the cantilever dynamics (not shown) point out that such a damping profile would not raise the oscillation-averaged damping above $5 \cdot 10^{-10}$ until a closest-approach distance of 0.2 nm. It is of course questionable whether this continuum theory holds down to a spacing of less than 10 molecular diameters. Furthermore, the question under which circumstances it is possible to use the bulk viscosity for confined water is a subject that is still under debate [158-161].

Repulsive force

Both on the hydrophilic and hydrophobic regions we measure an attractive force at larger separations that makes a smooth transition to a repulsive force as the tip comes closer to the surface. When the two amplitude curves are aligned in the way it has been done here, both repulsive and attractive forces over the hydrophilic domain seem to be shifted 0.4 nm away from the surface with respect to forces over the hydrophobic domain. A common problem in all AFM force measurements, is that there is often no way to determine the zero of distance except through features in the force profile itself. The forces at the dodecanethiol domain nearly reach their asymptote (vertical force-displacement curve) at a relatively low force of 600 pN, as can be seen in figure 7.5. It is very unlikely that at this force there is significant deformation of the alkane monolayer. Engelkes and Frisbie [162] determined that it takes tens of nanonewtons to plastically deform an alkanethiol monolayer on gold by more than 0.1 nm with an AFM tip of 20 nm radius. For elastic deformation, they found that the reduced Young's modulus of alkanethiol monolayers decreases with carbon chain length is from 54 to 48 GPa for chain lengths of 6 to 10 carbon atoms, and increases to 75 GPa for 12 carbon atoms due to increased crystalline order of the monolayer. In our sample, this crystalline order may not occur due to the small size of the SAM domains. Even if we assume a very conservative reduced Young's modulus of 30 GPa, the elastic deformation of the film at 600 pN of load with a 8.5 nm radius tip is estimated to be less than 0.03 nm for Hertzian contact mechanics or 0.06 nm for Johnson-Kendall-Roberts [163] contact mechanics (150 pN adhesive force). We therefore assume the position of this asymptote corresponds to the surface of the monolayer. Using this assumption, and considering the known film thicknesses of the monolayers that are grafted onto the same atomically smooth surface of gold, we can plot the force-distance curves with the separation axis referred to the gold surface. This is displayed in figure 7.8. Using these separations, we can start to give an interpretation to the measured forces.

Attractive force

The second thing to consider is the attractive part of the force profiles. Three possible explanations should be considered here: electrostatic forces, Van der Waals (dispersion) forces and hydration forces. Electrostatic interactions are not expected to play a role here, since neither the tip nor the surfaces carry a net charge, and the medium is pure water. The expected value for the Van der Waals interactions is less easily determined. To our knowledge, there is neither theoretical nor experimental work that gives a value for the Hamaker constant to be used in alkane monolayer-multiwall carbon nanotube interactions in water. Ederth [164] did extensive calculations for symmetric alkanethiol monolayer systems on gold, supported by experimental data. He concluded that the gold substrate dominates the Hamaker function at large separations, but at distances closer than 100 nm it starts to deviate, and at 1 nm separation the Hamaker function has values of 2 to $8 \cdot 10^{-20}$ J for SAM thicknesses of 3 to 0.5 nm respectively. This is less than the $31 \cdot 10^{-20}$ J expected for gold, but still much larger than the $0.6 \cdot 10^{-20}$ J expected for

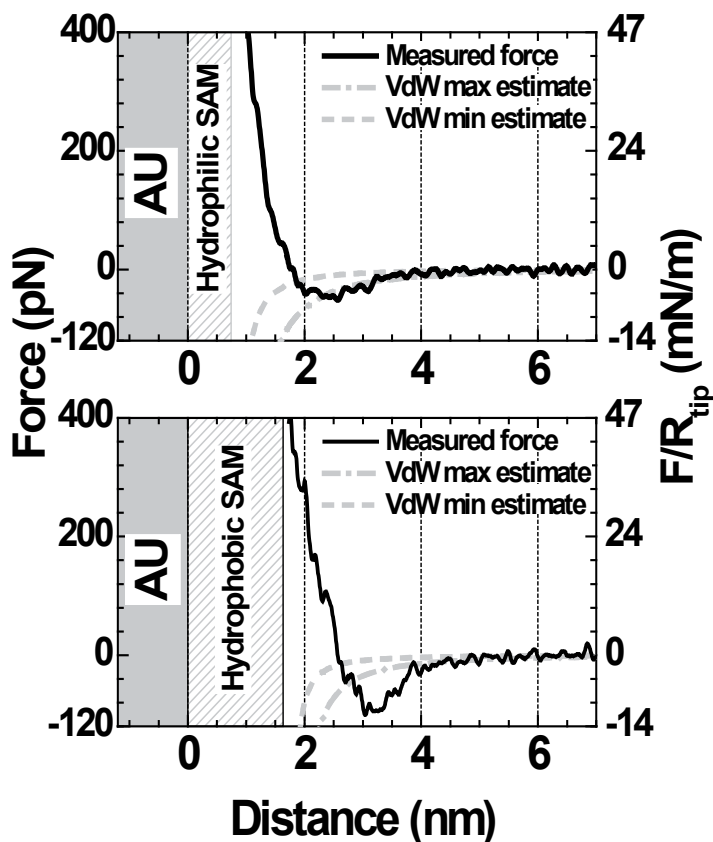


Figure 7.8 Forces in the context of the tip-sample distance

Averaged forces plotted in the context of surface topography. Top: Force above the hydrophilic domain (top) and hydrophobic domain (bottom) and calculated Van der Waals forces if the tip Hamaker constant is considered equal to that of graphite (grey dash-dotted line) or a single wall nanotube (grey dashed line). Clearly, the measured forces over the hydrophobic domain cannot be explained by Van der Waals forces alone.

the monolayers alone. In our situation, the second surface is not a gold-supported alkane, but a multiwall carbon nanotube. Two different approaches can be taken to estimate a Hamaker constant for multiwall carbon nanotubes. One is to use the constant determined for graphite in water by Dagastine *et al* [165], which is $11.5 \cdot 10^{-20}$ J. The other is to use the calculated value for a single-wall nanotube. Calculations for both vacuum [166] and water [167] as the medium show that for *single* wall nanotubes the Hamaker constants at close separations are one or two orders of magnitude weaker than those for graphite. According to Rajter and co-workers [167], axially interacting metallic single wall nanotubes in water have a Hamaker constant of no more than $0.8 \cdot 10^{-20}$ J, a value similar to that of hydrocarbons. Assuming that the Hamaker

constant of a multiwall nanotube is somewhere in between that of graphite and a single wall nanotube, we can give a minimum and a maximum estimate for the Van der Waals interaction in our measurements. We calculate the estimated Van der Waals force as the interaction through water (medium 3) between the nanotube (medium 4) and a half-space of alkane (medium 2) at distance d , plus the interaction with a half-space of gold (medium 1) at distance $d+d_{SAM}$, minus the interaction with a half-space of alkane at distance $d+d_{SAM}$. Here, d_{SAM} is the thickness of the self-assembled monolayer: $F_{vdW} = F_{vdW}(H_{432}, d) + F_{vdW}(H_{431}, d+d_{SAM}) - F_{vdW}(H_{432}, d+d_{SAM})$. This formula implicitly assumes the Hamaker constant between gold and nanotube is the same through water or alkane. For gold-gold interactions the error associated with this assumption is only 10% [164]. Asymmetric Hamaker constants are calculated with the approximation formula $H_{abc} = (H_{aba}H_{abc})^{1/2}$ [1]. The geometry we use for the force calculation is that of an infinite half-space interacting with a cylinder that has a spherical cap, a simple limiting case of the parametric model developed by Argento and French [168]: $F_{vdW}(H, d) = -2HR_{tip}^3 / (3d^2(d+2R_{tip})^2)$. The minimum and maximum estimates, which are calculated with this model, and the Hamaker constants for single-wall nanotubes and graphite respectively are displayed along with the measured forces in figure 7.8. The forces measured over the hydrophilic domain are still at the edge of what can be explained by Van der Waals interactions, but the attractive forces over the hydrophobic domain are clearly stronger. If we take the tip shape and surface topography into account, it is certainly not unlikely that the attractive interactions we see on the hydrophilic part are not Van der Waals interactions, but dominated by cross-talk from the neighboring hydrophobic parts. Figure 7.9 shows that a tip with the radius as was estimated from SEM measurements barely fits into the cavity above the hydrophilic domain. This means that as the tip gets closer to the hydrophilic surface, the hydrophobic interactions between the higher parts of the tip and the dodecanethiol domains get stronger as well. We would like to stress that this effect does not play a role on the -higher- hydrophobic domains.

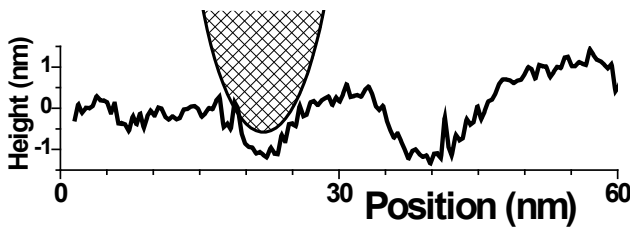


Figure 7.9 Cross section of the topography related to tip radius

A vertical cross-section through the reconstructed topography of figure 7.6, with a circle of 8.5 nm radius drawn in the same elongated height scale, and positioned at the location where forces on the hydrophilic domain were measured. From this geometry, it is clear that cross-talk from the neighboring hydrophobic domains may account for a large part of the attractive force measured.

Although it is not clear what physical model underlies the hydrophobic attraction, it is common practice to characterize it by fitting a single or double exponential function to the measurements. Exponential decay lengths varying between 1 nm and 30 nm are reported. An exponential fit of our measurement of the hydrophobic force is shown in figure 7.10. Correspondence between the fit and the data is excellent at all separations larger than the attractive minimum at 3 nm from the gold surface.

The exponential decay length that we find from a fit to the hydrophobic data is 0.6 nm. This is slightly lower, but of the same order of magnitude as what was found for surfactant-coated mica surfaces by Israelachvili and Pashley [169] and later by others, as reviewed by Christenson and Claesson [10]. Some authors have used a biexponential function for the fit, with one of the decay lengths in the range 10-30 nm. We performed measurements with an approach-retract cycle distance up to 20 nm, but forces measured at separations of more than 7 nm were smaller than the noise level.

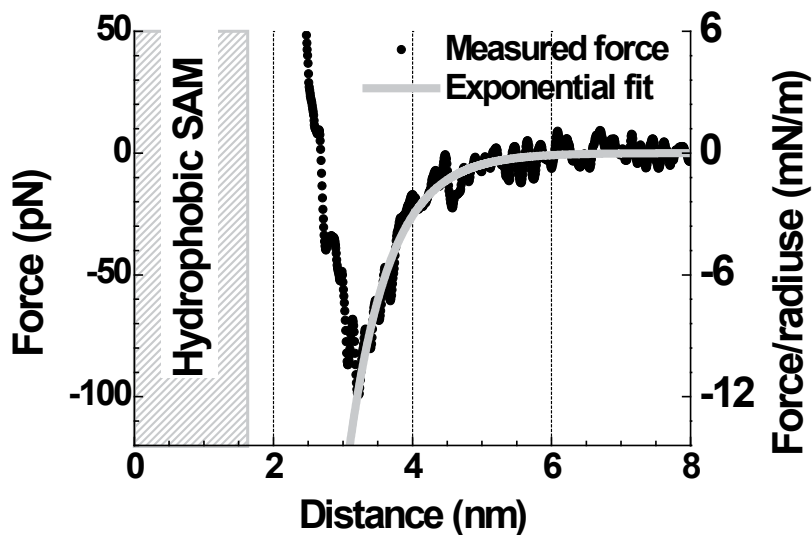


Figure 7.10 Exponential fit to the force measured on a hydrophobic domain

Exponential fit of the form $F(d) = F_0 \exp(-(d - d_{SAM})/\lambda_d)$ applied to the attractive part of the force measured on the hydrophobic domain. Best fits for the zero separation force F_0 and decay length λ_d are 1.46 ± 0.07 nN, (corresponding to 172 ± 9 mN/m) and 0.58 ± 0.01 nm. Monolayer thickness d_{SAM} was not a fit parameter.

7.5 Discussion

The measurements presented in this chapter are novel in a number of respects. 1) To our knowledge, no experimental results of spatially resolved force measurements adjacent to surfaces with nanoscale inhomogeneous hydrophobicity have been reported in the literature before. 2) Our measurements were carried out with a dynamic force measurement technique at a frequency over 1.16 MHz. This is two to four orders of magnitude faster than previous AFM measurements [68,158,170], and even more when compared to SFA measurements. 3) Multiwall carbon nanotube tips have been applied before in force measurements in aqueous solutions [37,68], but these probes have, to our knowledge, not been used successfully to investigate forces on hydrophobic surfaces.

It is therefore not surprising that our findings are quite different from what has been found before. The most prominent differences are: 1) A lack of attractive hydrophobic forces beyond 5 nm distance between hydrophobic surfaces. 2) A repulsive, rather than attractive interaction at zero distance between hydrophobic surfaces. 3) No oscillatory behavior of the hydration force between a carbon nanotube and a hydrophilic surface.

A recent molecular dynamics study by Giovambattista and coworkers [14] indicates that closely spaced hydrophilic and hydrophobic patches can have quite different properties from their homogeneous counterparts. One of their findings is that the spontaneous collapse of two homogeneous hydrophobic plates spaced 0.6 nm apart no longer occurs when the sites at the perimeter are replaced by hydrophilic entities. The patches in their simulations were a factor 10 smaller than those we studied, and the chemical nature of the sites ($-O$ and $-OH$ terminated silica) was different. Although the mechanism may be quite different, this finding is similar to our observation of a repulsive force between a hydrophobic tip and a hydrophobic patch. Whether this inhomogeneity has any influence on the oscillatory forces associated with hydrophilic hydration was not reported by Giovambattista, but it seems very likely. Other reasons why these oscillatory forces over a hydrophilic surface were not present in our experiment have to be considered as well. In contrast to other hydrophilic surfaces where these forces were measured (COOH terminated self-assembled monolayers or mica), the MES/AET surface presents both positive and negative ions to the aqueous interface. This may frustrate the layering of water perpendicular to the surface. An argument against this is that layering is observed above zwitterionic headgroups of lipids [39]. Finally, the surface roughness of the sample on the size scale of the probe might destroy measurable layering as well.

The surface inhomogeneity can also be an important factor when it comes to the long-range forces. At distances larger than the domain diameter, the tip will see an average of the forces

from the different domains. However, it has become more and more clear that the extremely long ranges that were reported for forces between hydrophobic surfaces are mostly based on artifacts such as nanobubbles or the rearrangement of surfactant layers [171], and it is estimated in a recent paper by Meyer and coworkers [11] that the true range of the hydrophobic attraction is no more than 10 nm. In the separation range between 1.5 and 7 nm, the forces we measure are equal to theirs within experimental error. The only point below 1 nm in the measurements of Meyer *et al.* is the pull-off adhesion force of order 500-1000 N/m. This is very different in our measurements, since we see a clear transition to repulsive forces in this distance regime. One possible cause for this might be the seven orders of magnitude difference in contact time. In our measurements, the tip is in a repulsive force regime only for a fraction of the oscillation period, which amounts to around 200 ns. Real contact time with the sample is estimated to be even an order of magnitude less, since the repulsive force is felt already at finite tip-sample separation.

The contact time in our experiments, however, is still long on the timescale of the dynamics of water molecules, making it unlikely that the timescale of reorientation of water molecules influences the contact adhesion or repulsion in our measurements. Studies by Dokter and coworkers [172] on the rotational correlation time of water molecules in inverted micelles show that near an interface this time increases by an order of magnitude. But the correlation time is then still around 15 ps.

Another timescale to be considered is that involved in translation. The viscous, or viscoelastic, properties of confined water are still the subject of debate, as was noted before. Some authors have suggested ice formation on graphite in ambient conditions [161], or a transition of liquid to solid behavior for confined fluids when the approach speed was increased [160], but it is argued that the latter will not occur for water [159]. To our knowledge, the sub-microsecond dynamics of water adjacent to a hydrophobic surface has not yet been investigated experimentally. Although the results of this study do hint towards a visco-elastic behavior of confined water, more research is needed to support such a claim.

If indeed the short contact time is the cause for the repulsive nature of the contact force, this would be a very interesting finding. When static force measurements and off-resonance excitation are combined with our small-cantilever technique, it should in principle be possible to investigate the frequency-dependence of forces over 7 orders of magnitude, making this a promising direction for future research.

7.6 Conclusion

We studied the forces adjacent to a surface with nanoscale hydrophilic and hydrophobic domains in pure water. Nanobubble formation can be identified on these samples by AFM imaging, and occurs only sparsely on samples with domain sizes of 10-50 nm. We performed the first spatially resolved measurement of interfacial forces on such a sample, acquiring AFM dynamic force curves at $256 \times 256 \sim 65000$ locations with a spacing of 0.4 nm, with a hydrophobic multiwall carbon nanotube tip, and an oscillation frequency of 1.1 MHz for the dynamic force profile measurements. Forces over a hydrophobic domain are attractive with a magnitude larger than can be expected from Van der Waals interaction. The distance dependence of this attractive hydrophobic force is well described by an exponential function with a decay length of 0.6 nm, which is similar to hydrophobic forces measured on homogeneous surfaces. The maximum of the attractive force occurs at 1.5 nm from the surface, and has a value of 12 mN/m. At closer separations the force becomes repulsive, which is a characteristic that is not seen in static measurement on homogeneous samples. It is not yet clear whether the surface chemical heterogeneity or the short timescales of the force measurement cause the repulsive force at short separations. We believe this study is an important step up from simplified homogeneous model systems, although there is still a long way to go towards the measurement and understanding of the forces that play a role in the complex and inhomogeneous situations found in nature.

References

1. J. N. Israelachvili, *Intermolecular and surface forces* (Academic Press, London, 1991).
2. C. Tanford: *Hydrophobic Effect and Organization of Living Matter*. *SCIENCE* **200**, 1012 (1978).
3. W. Kauzmann: *Some Factors in the Interpretation of Protein Denaturation*. *ADVANCES IN PROTEIN CHEMISTRY* **14**, 1 (1959).
4. K. Lum, D. Chandler, and J. D. Weeks: *Hydrophobicity at small and large length scales*. *J. PHYS. CHEM. B* **103**, 4570 (1999).
5. H. J. Butt, B. Cappella, and M. Kappl: *Force measurements with the atomic force microscope: Technique, interpretation and applications*. *SURFACE SCIENCE REPORTS* **59**, 1 (2005).
6. J. Israelachvili and H. Wennerstrom: *Role of hydration and water structure in biological and colloidal interactions*. *NATURE* **379**, 219 (1996).
7. H. K. Christenson and P. M. Claesson: *Cavitation and the Interaction Between Macroscopic Hydrophobic Surfaces*. *SCIENCE* **239**, 390 (1988).
8. J. Israelachvili and R. Pashley: *The Hydrophobic Interaction Is Long-Range, Decaying Exponentially with Distance*. *NATURE* **300**, 341 (1982).
9. J. Wood and R. Sharma: *Interaction Forces Between Hydrophobic Mica Surfaces*. *JOURNAL OF ADHESION SCIENCE AND TECHNOLOGY* **9**, 1075 (1995).
10. H. K. Christenson and P. M. Claesson: *Direct measurements of the force between hydrophobic surfaces in water*. *ADVANCES IN COLLOID AND INTERFACE SCIENCE* **91**, 391 (2001).
11. E. E. Meyer, K. J. Rosenberg, and J. Israelachvili: *Recent progress in understanding hydrophobic interactions*. *PROCEEDINGS OF THE NATIONAL ACADEMY OF SCIENCES OF THE UNITED STATES OF AMERICA* **103**, 15739 (2006).
12. L. Maibaum, A. R. Dinner, and D. Chandler: *Micelle formation and the hydrophobic effect*. *J. PHYS. CHEM. B* **108**, 6778 (2004).
13. D. Chandler: *Interfaces and the driving force of hydrophobic assembly*. *NATURE* **437**, 640 (2005).
14. N. Giovambattista, P. G. Debenedetti, and P. J. Rossky: *Hydration behavior under confinement by nanoscale surfaces with patterned hydrophobicity and hydrophilicity*. *JOURNAL OF PHYSICAL CHEMISTRY C* **111**, 1323 (2007).
15. G. Binnig, C. F. Quate, and C. Gerber: *Atomic Force Microscope*. *PHYSICAL REVIEW LETTERS* **56**, 930 (1986).

16. F. J. Giessibl: *Advances in atomic force microscopy*. REVIEWS OF MODERN PHYSICS **75**, 949 (2003).
17. Y. F. Dufrene: *Recent progress in the application of atomic force microscopy imaging and force spectroscopy to microbiology*. CURRENT OPINION IN MICROBIOLOGY **6**, 317 (2003).
18. R. S. Khan and D. Rousseau: *Hazelnut oil migration in dark chocolate - kinetic, thermodynamic and structural considerations*. EUROPEAN JOURNAL OF LIPID SCIENCE AND TECHNOLOGY **108**, 434 (2006).
19. N. V. Joshi, H. Medina, C. Colasante, and A. Osuna: *Ultrastructural investigation of human sperm using atomic force microscopy*. ARCHIVES OF ANDROLOGY **44**, 51 (2000).
20. E. L. Florin, V. T. Moy, and H. E. Gaub: *Adhesion Forces Between Individual Ligand-Receptor Pairs*. SCIENCE **264**, 415 (1994).
21. M. Rief, M. Gautel, F. Oesterhelt, J. M. Fernandez, and H. E. Gaub: *Reversible unfolding of individual titin immunoglobulin domains by AFM*. SCIENCE **276**, 1109 (1997).
22. R. Merkel, P. Nassoy, A. Leung, K. Ritchie, and E. Evans: *Energy landscapes of receptor-ligand bonds explored with dynamic force spectroscopy*. NATURE **397**, 50 (1999).
23. D. Tabor and R. H. S. Winterton: *Surface Forces - Direct Measurement of Normal and Retarded Van der Waals Forces*. NATURE **219**, 1120-& (1968).
24. A. Ashkin, J. M. Dziedzic, and T. Yamane: *Optical Trapping and Manipulation of Single Cells Using Infrared-Laser Beams*. NATURE **330**, 769 (1987).
25. K. C. Neuman and S. M. Block: *Optical trapping*. REVIEW OF SCIENTIFIC INSTRUMENTS **75**, 2787 (2004).
26. W. A. Ducker, T. J. Senden, and R. M. Pashley: *Direct Measurement of Colloidal Forces Using An Atomic Force Microscope*. NATURE **353**, 239 (1991).
27. R. P. Goncalves and S. Scheuring: *Manipulating and imaging individual membrane proteins by AFM*. SURFACE AND INTERFACE ANALYSIS **38**, 1413 (2006).
28. Y. Sugimoto, P. Pou, M. Abe *et al.*: *Chemical identification of individual surface atoms by atomic force microscopy*. NATURE **446**, 64 (2007).
29. G. Meyer and N. M. Amer: *Novel Optical Approach to Atomic Force Microscopy*. APPLIED PHYSICS LETTERS **53**, 1045 (1988).
30. S. Alexander, L. Hellemans, O. Marti *et al.*: *An Atomic-Resolution Atomic-Force Microscope Implemented Using An Optical-Lever*. JOURNAL OF APPLIED PHYSICS **65**, 164 (1989).
31. O. Marti, B. Drake, and P. K. Hansma: *Atomic Force Microscopy of Liquid-Covered Surfaces - Atomic Resolution Images*. APPLIED PHYSICS LETTERS **51**, 484 (1987).
32. W. Haberle, J. K. H. Hoerber, and G. Binnig: *Force Microscopy on Living Cells*. JOURNAL OF VACUUM SCIENCE & TECHNOLOGY B **9**, 1210 (1991).
33. Q. Zhong, D. Inniss, K. Kjoller, and V. B. Elings: *Fractured Polymer Silica Fiber Surface Studied by Tapping Mode Atomic-Force Microscopy*. SURFACE SCIENCE **290**, L688-L692 (1993).

34. H. G. Hansma, R. L. Sinsheimer, J. Groppe *et al.*: *Recent Advances in Atomic-Force Microscopy of Dna*. SCANNING **15**, 296 (1993).
35. P. K. Hansma, J. P. Cleveland, M. Radmacher *et al.*: *Tapping Mode Atomic-Force Microscopy in Liquids*. APPLIED PHYSICS LETTERS **64**, 1738 (1994).
36. T. R. Albrecht, P. Grutter, D. Horne, and D. Rugar: *Frequency-Modulation Detection Using High-Q Cantilevers for Enhanced Force Microscope Sensitivity*. JOURNAL OF APPLIED PHYSICS **69**, 668 (1991).
37. S. P. Jarvis, T. Uchihashi, T. Ishida, H. Tokumoto, and Y. Nakayama: *Local solvation shell measurement in water using a carbon nanotube probe*. J. PHYS. CHEM. B **104**, 6091 (2000).
38. T. Fukuma, K. Kobayashi, K. Matsushige, and H. Yamada: *True atomic resolution in liquid by frequency-modulation atomic force microscopy*. APPLIED PHYSICS LETTERS **87**, (2005).
39. T. Fukuma, M. J. Higgins, and S. P. Jarvis: *Direct imaging of lipid-ion network formation under physiological conditions by frequency modulation atomic force microscopy*. PHYSICAL REVIEW LETTERS **98**, (2007).
40. T. R. Albrecht and C. F. Quate: *Atomic Resolution Imaging of A Nonconductor by Atomic Force Microscopy*. JOURNAL OF APPLIED PHYSICS **62**, 2599 (1987).
41. T. R. Albrecht, S. Akamine, T. E. Carver, and C. F. Quate: *Microfabrication of Cantilever Styli for the Atomic Force Microscope*. JOURNAL OF VACUUM SCIENCE & TECHNOLOGY A-VACUUM SURFACES AND FILMS **8**, 3386 (1990).
42. D. A. Walters, J. P. Cleveland, N. H. Thomson *et al.*: *Short cantilevers for atomic force microscopy*. REVIEW OF SCIENTIFIC INSTRUMENTS **67**, 3583 (1996).
43. G. T. Palocz, B. L. Smith, P. K. Hansma, D. A. Walters, and M. A. Wendman: *Rapid imaging of calcite crystal growth using atomic force microscopy with small cantilevers*. APPLIED PHYSICS LETTERS **73**, 1658 (1998).
44. M. B. Viani, L. I. Pietrasanta, J. B. Thompson *et al.*: *Probing protein-protein interactions in real time*. NATURE STRUCTURAL BIOLOGY **7**, 644 (2000).
45. A. Chand, M. B. Viani, T. E. Schaffer, and P. K. Hansma: *Microfabricated small metal cantilevers with silicon tip for atomic force microscopy*. JOURNAL OF MICROELECTROMECHANICAL SYSTEMS **9**, 112 (2000).
46. T. Ando, N. Kodera, E. Takai, D. Maruyama, K. Saito, and A. Toda: *A high-speed atomic force microscope for studying biological macromolecules*. PROCEEDINGS OF THE NATIONAL ACADEMY OF SCIENCES OF THE UNITED STATES OF AMERICA **98**, 12468 (2001).
47. T. Ando, T. Uchihashi, N. Kodera *et al.*: *High-speed atomic force microscopy for studying the dynamic behavior of protein molecules at work*. JAPANESE JOURNAL OF APPLIED PHYSICS PART 1-REGULAR PAPERS BRIEF COMMUNICATIONS & REVIEW PAPERS **45**, 1897 (2006).
48. G. E. Fantner, G. Schitter, J. H. Kindt *et al.*: *Components for high speed atomic force microscopy*. ULTRAMICROSCOPY **106**, 881 (2006).

49. P. K. Hansma, G. Schitter, G. E. Fantner, and C. Prater: *Applied physics - High-speed atomic force microscopy*. SCIENCE **314**, 601 (2006).
50. J. H. Kindt, G. E. Fantner, J. A. Cutroni, and P. K. Hansma: *Rigid design of fast scanning probe microscopes using finite element analysis*. ULTRAMICROSCOPY **100**, 259 (2004).
51. N. Kodera, H. Yamashita, and T. Ando: *Active damping of the scanner for high-speed atomic force microscopy*. REVIEW OF SCIENTIFIC INSTRUMENTS **76**, (2005).
52. N. Kodera, M. Sakashita, and T. Ando: *Dynamic proportional-integral-differential controller for high-speed atomic force microscopy*. REVIEW OF SCIENTIFIC INSTRUMENTS **77**, (2006).
53. N. Kodera, Y. Naito, T. Ito, and T. Ando: *Improvements on a high-speed atomic force microscope*. BIOPHYS. J. **84**, 467A (2003).
54. T. Uchihashi, T. Ando, and H. Yamashita: *Fast phase imaging in liquids using a rapid scan atomic force microscope*. APPLIED PHYSICS LETTERS **89**, (2006).
55. T. Uchihashi, N. Kodera, H. Itoh, H. Yamashita, and T. Ando: *Feed-forward compensation for high-speed atomic force microscopy imaging of biomolecules*. JAPANESE JOURNAL OF APPLIED PHYSICS PART 1-REGULAR PAPERS BRIEF COMMUNICATIONS & REVIEW PAPERS **45**, 1904 (2006).
56. T. Gutschmann, G. E. Fantner, J. H. Kindt, M. Venturoni, S. Danielsen, and P. K. Hansma: *Force spectroscopy of collagen fibers to investigate their mechanical properties and structural organization*. BIOPHYS. J. **86**, 3186 (2004).
57. M. B. Viani, T. E. Schaffer, A. Chand, M. Rief, H. E. Gaub, and P. K. Hansma: *Small cantilevers for force spectroscopy of single molecules*. JOURNAL OF APPLIED PHYSICS **86**, 2258 (1999).
58. H. B. Callen and T. A. Welton: *Irreversibility and Generalized Noise*. PHYSICAL REVIEW **83**, 34 (1951).
59. S. Hembacher, F. J. Giessibl, and J. Mannhart: *Force microscopy with light-atom probes*. SCIENCE **305**, 380 (2004).
60. S. Hembacher, F. J. Giessibl, J. Mannhart, and C. F. Quate: *Local spectroscopy and atomic imaging of tunneling current, forces, and dissipation on graphite*. PHYSICAL REVIEW LETTERS **94**, (2005).
61. F. Gittes and C. F. Schmidt: *Thermal noise limitations on micromechanical experiments*. EUROPEAN BIOPHYSICS JOURNAL WITH BIOPHYSICS LETTERS **27**, 75 (1998).
62. J. E. Sader: *Frequency response of cantilever beams immersed in viscous fluids with applications to the atomic force microscope*. JOURNAL OF APPLIED PHYSICS **84**, 64 (1998).
63. J. W. M. Chon, P. Mulvaney, and J. E. Sader: *Experimental validation of theoretical models for the frequency response of atomic force microscope cantilever beams immersed in fluids*. JOURNAL OF APPLIED PHYSICS **87**, 3978 (2000).

64. J. E. Sader, J. Pacifico, C. P. Green, and P. Mulvaney: *General scaling law for stiffness measurement of small bodies with applications to the atomic force microscope*. JOURNAL OF APPLIED PHYSICS **97**, (2005).
65. M. R. Paul, M. T. Clark, and M. C. Cross: *The stochastic dynamics of micron and nanoscale elastic cantilevers in fluid: fluctuations from dissipation*. NANOTECHNOLOGY **17**, 4502 (2006).
66. P. Hinterdorfer and Y. F. Dufrene: *Detection and localization of single molecular recognition events using atomic force microscopy*. NATURE METHODS **3**, 347 (2006).
67. S. J. O'Shea and M. E. Welland: *Atomic force microscopy at solid-liquid interfaces*. LANGMUIR **14**, 4186 (1998).
68. T. Uchihashi, M. Higgins, Y. Nakayama, J. E. Sader, and S. P. Jarvis: *Quantitative measurement of solvation shells using frequency modulated atomic force microscopy*. NANOTECHNOLOGY **16**, S49-S53 (2005).
69. J. P. Cleveland, T. E. Schaffer, and P. K. Hansma: *Probing Oscillatory Hydration Potentials Using Thermal-Mechanical Noise in An Atomic-Force Microscope*. PHYSICAL REVIEW B **52**, R8692-R8695 (1995).
70. W. F. Heinz, M. D. Antonik, and J. H. Hoh: *Reconstructing local interaction potentials from perturbations to the thermally driven motion of an atomic force microscope cantilever*. J. PHYS. CHEM. B **104**, 622 (2000).
71. O. H. Willemsen, L. Kuipers, K. O. van der Werf, B. G. de Grooth, and J. Greve: *Reconstruction of the tip-surface interaction potential by analysis of the Brownian motion of an atomic force microscope tip*. LANGMUIR **16**, 4339 (2000).
72. P. D. Ashby and C. M. Lieber: *Brownian force profile reconstruction of interfacial 1-nonanol solvent structure*. JOURNAL OF THE AMERICAN CHEMICAL SOCIETY **126**, 16973 (2004).
73. M. Nguyen-Duong, K. W. Koch, and R. Merkel: *Surface anchoring reduces the lifetime of single specific bonds*. EUROPHYSICS LETTERS **61**, 845 (2003).
74. M. Kitazawa, K. Shiotani, and A. Toda: *Batch fabrication of sharpened silicon nitride tips*. JAPANESE JOURNAL OF APPLIED PHYSICS PART 1-REGULAR PAPERS SHORT NOTES & REVIEW PAPERS **42**, 4844 (2003).
75. J. H. Kindt, G. E. Fantner, J. B. Thompson, and P. K. Hansma: *Automated wafer-scale fabrication of electron beam deposited tips for atomic force microscopes using pattern recognition*. NANOTECHNOLOGY **15**, 1131 (2004).
76. J. L. Yang, M. Despont, U. Drechsler *et al.*: *Miniaturized single-crystal silicon cantilevers for scanning force microscopy*. APPLIED PHYSICS LETTERS **86**, (2005).
77. SCL sensor tech GesmbH, www.sclsensortech.com, 2007
78. D. Karabacak, T. Kouh, and K. L. Ekinici: *Analysis of optical interferometric displacement detection in nanoelectromechanical systems*. JOURNAL OF APPLIED PHYSICS **98**, (2005).
79. D. Rugar, H. J. Mamin, and P. Guethner: *Improved Fiber-Optic Interferometer for Atomic Force Microscopy*. APPLIED PHYSICS LETTERS **55**, 2588 (1989).

80. B. W. Hoogenboom, P. L. T. M. Frederix, J. L. Yang *et al.*: *A Fabry-Perot interferometer for micrometer-sized cantilevers*. APPLIED PHYSICS LETTERS **86**, (2005).
81. B. Rogers, L. Manning, T. Sulchek, and J. D. Adams: *Improving tapping mode atomic force microscopy with piezoelectric cantilevers*. ULTRAMICROSCOPY **100**, 267 (2004).
82. M. Li, H. X. Tang, and M. L. Roukes: *Ultra-sensitive NEMS-based cantilevers for sensing, scanned probe and very high-frequency applications*. NATURE NANOTECHNOLOGY **2**, 114 (2007).
83. M. G. L. Gustafsson and J. Clarke: *Scanning Force Microscope Springs Optimized for Optical-Beam Deflection and with Tips Made by Controlled Fracture*. JOURNAL OF APPLIED PHYSICS **76**, 172 (1994).
84. C. A. J. Putman, B. G. Degrooth, N. F. Vanhulst, and J. Greve: *A Detailed Analysis of the Optical Beam Deflection Technique for Use in Atomic Force Microscopy*. JOURNAL OF APPLIED PHYSICS **72**, 6 (1992).
85. T. E. Schaffer and P. K. Hansma: *Characterization and optimization of the detection sensitivity of an atomic force microscope for small cantilevers*. JOURNAL OF APPLIED PHYSICS **84**, 4661 (1998).
86. T. Fukuma, M. Kimura, K. Kobayashi, K. Matsushige, and H. Yamada: *Development of low noise cantilever deflection sensor for multienvironment frequency-modulation atomic force microscopy*. REVIEW OF SCIENTIFIC INSTRUMENTS **76**, (2005).
87. T. E. Schaffer and H. Fuchs: *Optimized detection of normal vibration modes of atomic force microscope cantilevers with the optical beam deflection method*. JOURNAL OF APPLIED PHYSICS **97**, (2005).
88. T. E. Schaffer, M. Richter, and M. B. Viani: *Array detector for the atomic force microscope*. APPLIED PHYSICS LETTERS **76**, 3644 (2000).
89. T. E. Schaffer: *Force spectroscopy with a large dynamic range using small cantilevers and an array detector*. JOURNAL OF APPLIED PHYSICS **91**, 4739 (2002).
90. M. J. Higgins, R. Proksch, J. E. Sader *et al.*: *Noninvasive determination of optical lever sensitivity in atomic force microscopy*. REVIEW OF SCIENTIFIC INSTRUMENTS **77**, (2006).
91. M. J. Rost, L. Crama, P. Schakel *et al.*: *Scanning probe microscopes go video rate and beyond*. REVIEW OF SCIENTIFIC INSTRUMENTS **76**, (2005).
92. C. M. Stroh, A. Ebner, M. Geretschlager *et al.*: *Simultaneous topography and recognition Imaging using force microscopy*. BIOPHYS. J. **87**, 1981 (2004).
93. M. Radmacher, M. Fritz, J. P. Cleveland, D. A. Walters, and P. K. Hansma: *Imaging adhesion forces and elasticity of lysozyme adsorbed on mica with the atomic force microscope*. LANGMUIR **10**, 3809 (1994).
94. W. F. Heinz and J. H. Hoh: *Spatially resolved force spectroscopy of biological surfaces using the atomic force microscope*. TRENDS IN BIOTECHNOLOGY **17**, 143 (1999).

95. K. O. Vanderwerf, C. A. J. Putman, B. G. Degrooth, and J. Greve: *Adhesion Force Imaging in Air and Liquid by Adhesion Mode Atomic-Force Microscopy*. APPLIED PHYSICS LETTERS **65**, 1195 (1994).
96. A. Rosa-Zeiser, E. Weilandt, S. Hild, and O. Marti: *The simultaneous measurement of elastic, electrostatic and adhesive properties by scanning force microscopy: pulsed-force mode operation*. MEASUREMENT SCIENCE & TECHNOLOGY **8**, 1333 (1997).
97. P. J. de Pablo, J. Colchero, J. Gomez-Herrero, and A. M. Baro: *Jumping mode scanning force microscopy*. APPLIED PHYSICS LETTERS **73**, 3300 (1998).
98. H. U. Krottil, T. Stifter, and O. Marti: *Concurrent measurement of adhesive and elastic surface properties with a new modulation technique for scanning force microscopy*. REVIEW OF SCIENTIFIC INSTRUMENTS **71**, 2765 (2000).
99. J. Kokavecz, O. Marti, P. Heszler, and A. Mechler: *Imaging bandwidth of the tapping mode atomic force microscope probe*. PHYSICAL REVIEW B **73**, (2006).
100. J. B. Pethica and W. C. Oliver: *Tip Surface Interactions in Stm and Afm*. PHYSICA SCRIPTA **T19A**, 61 (1987).
101. U. Durig: *Extracting interaction forces and complementary observables in dynamic probe microscopy*. APPLIED PHYSICS LETTERS **76**, 1203 (2000).
102. F. J. Giessibl: *Forces and frequency shifts in atomic-resolution dynamic-force microscopy*. PHYSICAL REVIEW B **56**, 16010 (1997).
103. J. E. Sader and S. P. Jarvis: *Interpretation of frequency modulation atomic force microscopy in terms of fractional calculus*. PHYSICAL REVIEW B **70**, (2004).
104. J. E. Sader and S. P. Jarvis: *Accurate formulas for interaction force and energy in frequency modulation force spectroscopy*. APPLIED PHYSICS LETTERS **84**, 1801 (2004).
105. J. E. Sader, T. Uchihashi, M. J. Higgins, A. Farrell, Y. Nakayama, and S. P. Jarvis: *Quantitative force measurements using frequency modulation atomic force microscopy - theoretical foundations*. NANOTECHNOLOGY **16**, S94-S101 (2005).
106. S. Basak, A. Raman, and S. V. Garimella: *Hydrodynamic loading of microcantilevers vibrating in viscous fluids*. JOURNAL OF APPLIED PHYSICS **99**, (2006).
107. C. P. Green and J. E. Sader: *Frequency response of cantilever beams immersed in viscous fluids near a solid surface with applications to the atomic force microscope*. JOURNAL OF APPLIED PHYSICS **98**, (2005).
108. G. C. Ratcliff, D. A. Erie, and R. Superfine: *Photothermal modulation for oscillating mode atomic force microscopy in solution*. APPLIED PHYSICS LETTERS **72**, 1911 (1998).
109. N. Umeda, S. Ishizaki, and H. Uwai: *Scanning Attractive Force Microscope Using Photothermal Vibration*. JOURNAL OF VACUUM SCIENCE & TECHNOLOGY B **9**, 1318 (1991).
110. W. H. Han, S. M. Lindsay, and T. W. Jing: *A magnetically driven oscillating probe microscope for operation in liquids*. APPLIED PHYSICS LETTERS **69**, 4111 (1996).

111. S. P. Jarvis, H. Yamada, S. I. Yamamoto, and H. Tokumoto: *A new force controlled atomic force microscope for use in ultrahigh vacuum*. REVIEW OF SCIENTIFIC INSTRUMENTS **67**, 2281 (1996).
112. O. Enders, F. Korte, and H. A. Kolb: *Lorentz-force-induced excitation of cantilevers for oscillation-mode scanning probe microscopy*. SURFACE AND INTERFACE ANALYSIS **36**, 119 (2004).
113. A. C. Hillier and A. J. Bard: *ac-mode atomic force microscope imaging in air and solutions with a thermally driven bimetallic cantilever probe*. REVIEW OF SCIENTIFIC INSTRUMENTS **68**, 2082 (1997).
114. H. Ueyama, Y. Sugawara, and S. Morita: *Stable operation mode for dynamic noncontact atomic force microscopy*. APPLIED PHYSICS A-MATERIALS SCIENCE & PROCESSING **66**, S295-S297 (1998).
115. S. Kitamura and M. Iwatsuki: *Observation of 7X7 Reconstructed Structure on the Silicon (111) Surface Using Ultrahigh-Vacuum Noncontact Atomic-Force Microscopy*. JAPANESE JOURNAL OF APPLIED PHYSICS PART 2-LETTERS **34**, L145-L148 (1995).
116. T. Fukuma, J. I. Kilpatrick, and S. P. Jarvis: *Phase modulation atomic force microscope with true atomic resolution*. REVIEW OF SCIENTIFIC INSTRUMENTS **77**, (2006).
117. Y. Sugawara, N. Kobayashi, M. Kawakami, Y. J. Li, Y. Naitoh, and M. Kageshima: *Elimination of instabilities in phase shift curves in phase-modulation atomic force microscopy in constant-amplitude mode*. APPLIED PHYSICS LETTERS **90**, (2007).
118. P. D. Ashby and C. M. Lieber: *Ultra-sensitive imaging and interfacial analysis of patterned hydrophilic SAM surfaces using energy dissipation chemical force microscopy*. JOURNAL OF THE AMERICAN CHEMICAL SOCIETY **127**, 6814 (2005).
119. M. Stark, R. W. Stark, W. M. Heckl, and R. Guckenberger: *Inverting dynamic force microscopy: From signals to time-resolved interaction forces*. PROCEEDINGS OF THE NATIONAL ACADEMY OF SCIENCES OF THE UNITED STATES OF AMERICA **99**, 8473 (2002).
120. R. W. Stark and W. M. Heckl: *Fourier transformed atomic force microscopy: tapping mode atomic force microscopy beyond the Hookian approximation*. SURFACE SCIENCE **457**, 219 (2000).
121. H. Holscher: *Quantitative measurement of tip-sample interactions in amplitude modulation atomic force microscopy*. APPLIED PHYSICS LETTERS **89**, (2006).
122. L. Nony, R. Boisgard, and J. P. Aime: *Nonlinear dynamical properties of an oscillating tip-cantilever system in the tapping mode*. JOURNAL OF CHEMICAL PHYSICS **111**, 1615 (1999).
123. M. H. Whangbo, G. Bar, and R. Brandsch: *Description of phase imaging in tapping mode atomic force microscopy by harmonic approximation*. SURFACE SCIENCE **411**, L794-L801 (1998).
124. A. S. Paulo and R. Garcia: *Unifying theory of tapping-mode atomic-force microscopy*. PHYSICAL REVIEW B **66**, (2002).

125. U. Durig: *Relations between interaction force and frequency shift in large-amplitude dynamic force microscopy*. APPLIED PHYSICS LETTERS **75**, 433 (1999).
126. B. Anczykowski, B. Gotsmann, H. Fuchs, J. P. Cleveland, and V. B. Elings: *How to measure energy dissipation in dynamic mode atomic force microscopy*. APPLIED SURFACE SCIENCE **140**, 376 (1999).
127. U. Durig: *Interaction sensing in dynamic force microscopy*. NEW JOURNAL OF PHYSICS **2**, 1 (2000).
128. J. E. Sader and S. P. Jarvis: *Coupling of conservative and dissipative forces in frequency-modulation atomic force microscopy*. PHYSICAL REVIEW B **74**, (2006).
129. J. P. Cleveland, B. Anczykowski, A. E. Schmid, and V. B. Elings: *Energy dissipation in tapping-mode atomic force microscopy*. APPLIED PHYSICS LETTERS **72**, 2613 (1998).
130. R. W. Stark, G. Schitter, and A. Stemmer: *Tuning the interaction forces in tapping mode atomic force microscopy*. PHYSICAL REVIEW B **68**, (2003).
131. A. San Paulo and R. Garcia: *Tip-surface forces, amplitude, and energy dissipation in amplitude-modulation (tapping mode) force microscopy*. PHYSICAL REVIEW B **64**, art-193411 (2001).
132. L. Wang: *Analytical descriptions of the tapping-mode atomic force microscopy response*. APPLIED PHYSICS LETTERS **73**, 3781 (1998).
133. J. Tamayo and R. Garcia: *Effects of elastic and inelastic interactions on phase contrast images in tapping-mode scanning force microscopy*. APPLIED PHYSICS LETTERS **71**, 2394 (1997).
134. B. Gotsmann, B. Anczykowski, C. Seidel, and H. Fuchs: *Determination of tip-sample interaction forces from measured dynamic force spectroscopy curves*. APPLIED SURFACE SCIENCE **140**, 314 (1999).
135. R. Garcia and A. San Paulo: *Dynamics of a vibrating tip near or in intermittent contact with a surface*. PHYSICAL REVIEW B **61**, R13381-R13384 (2000).
136. J. P. Aime, G. Couturier, R. Boisgard, and L. Nony: *Relationship between the non linear dynamic behaviour of an oscillating tip-microlever system and the contrast at the atomic scale*. APPLIED SURFACE SCIENCE **140**, 333 (1999).
137. B. Gotsmann and H. Fuchs: *Dynamic AFM using the FM technique with constant excitation amplitude*. APPLIED SURFACE SCIENCE **188**, 355 (2002).
138. S. I. Lee, S. W. Howell, A. Raman, and R. Reifenberger: *Nonlinear dynamics of microcantilevers in tapping mode atomic force microscopy: A comparison between theory and experiment*. PHYSICAL REVIEW B **66**, (2002).
139. M. H. Lee and W. H. Jhe: *General theory of amplitude-modulation atomic force microscopy*. PHYSICAL REVIEW LETTERS **97**, (2006).
140. P. Martin, S. Marsaudon, J. P. Aime, and B. Bennetau: *Experimental determination of conservative and dissipative parts in the tapping mode on a grafted layer: comparison with frequency modulation data*. NANOTECHNOLOGY **16**, 901 (2005).

141. B. V. Derjaguin, V. M. Muller, and Y. P. Toporov: *Effect of Contact Deformations on Adhesion of Particles*. JOURNAL OF COLLOID AND INTERFACE SCIENCE **53**, 314 (1975).
142. D. Maugis: *Adhesion of Spheres - the Jkr-Dmt Transition Using A Dugdale Model*. JOURNAL OF COLLOID AND INTERFACE SCIENCE **150**, 243 (1992).
143. R. Garcia and R. Perez: *Dynamic atomic force microscopy methods*. SURFACE SCIENCE REPORTS **47**, 197 (2002).
144. J. L. Parker, P. M. Claesson, and P. Attard: *Bubbles, Cavities, and the Long-Ranged Attraction Between Hydrophobic Surfaces*. JOURNAL OF PHYSICAL CHEMISTRY **98**, 8468 (1994).
145. J. W. G. Tyrrell and P. Attard: *Images of nanobubbles on hydrophobic surfaces and their interactions*. PHYSICAL REVIEW LETTERS **87**, 17 (2001).
146. P. Attard: *Nanobubbles and the hydrophobic attraction*. ADVANCES IN COLLOID AND INTERFACE SCIENCE **104**, 75 (2003).
147. X. H. Zhang, N. Maeda, and V. S. J. Craig: *Physical properties of nanobubbles on hydrophobic surfaces in water and aqueous solutions*. LANGMUIR **22**, 5025 (2006).
148. A. Agrawal, J. Park, D. Y. Ryu, P. T. Hammond, T. P. Russell, and G. H. McKinley: *Controlling the location and spatial extent of nanobubbles using hydrophobically nanopatterned surfaces*. NANO LETTERS **5**, 1751 (2005).
149. R. M. M. Smeets, U. F. Keyser, M. Y. Wu, N. H. Dekker, and C. Dekker: *Nanobubbles in solid-state nanopores*. PHYSICAL REVIEW LETTERS **97**, (2006).
150. X. H. Zhang, A. Khan, and W. A. Ducker: *A nanoscale gas state*. PHYSICAL REVIEW LETTERS **98**, (2007).
151. A. Poynor, L. Hong, I. K. Robinson, S. Granick, Z. Zhang, and P. A. Fenter: *How water meets a hydrophobic surface*. PHYSICAL REVIEW LETTERS **97**, (2006).
152. D. A. Doshi, E. B. Watkins, J. N. Israelachvili, and J. Majewski: *Reduced water density at hydrophobic surfaces: Effect of dissolved gases*. PROCEEDINGS OF THE NATIONAL ACADEMY OF SCIENCES OF THE UNITED STATES OF AMERICA **102**, 9458 (2005).
153. P. H. Phong, Y. Ooi, D. Hobar, N. Nishi, M. Yamamoto, and T. Kakiuchi: *Phase separation of ternary self-assembled monolayers into hydrophobic 1-dodecanethiol domains and electrostatically stabilized hydrophilic domains composed of 2-aminoethanethiol and 2-mercaptoethanesulfonic acid on Au(111)*. LANGMUIR **21**, 10581 (2005).
154. M. Kawasaki and H. Uchiki: *Sputter deposition of atomically flat Au(111) and Ag(111) films*. SURFACE SCIENCE **388**, L1121-L1125 (1997).
155. J. E. Sader, J. W. M. Chon, and P. Mulvaney: *Calibration of rectangular atomic force microscope cantilevers*. REVIEW OF SCIENTIFIC INSTRUMENTS **70**, 3967 (1999).
156. D. C. G. Klein, PH. D. THESIS, Universiteit Leiden, 2004. Available online at: <http://www.physics.leidenuniv.nl/sections/cm/ip/group/publications.htm>

157. P. H. Phong, V. V. Sokolov, N. Nishi, M. Yamamoto, and T. Kakiuchi: *Concentration-dependent switching of the mode of phase separation in ternary self-assembled monolayers of 2-mercaptoethane sulfonic acid, 2-aminoethanethiol and 1-dodecanethiol on Au(111)*. JOURNAL OF ELECTROANALYTICAL CHEMISTRY **600**, 35 (2007).
158. S. Jeffery, P. M. Hoffmann, J. B. Pethica, C. Ramanujan, H. O. Ozer, and A. Oral: *Direct measurement of molecular stiffness and damping in confined water layers*. PHYSICAL REVIEW B **70**, (2004).
159. U. Raviv, S. Perkin, P. Laurat, and J. Klein: *Fluidity of water confined down to subnanometer films*. LANGMUIR **20**, 5322 (2004).
160. S. Patil, G. Matei, A. Oral, and P. M. Hoffmann: *Solid or liquid? Solidification of a nanoconfined liquid under nonequilibrium conditions*. LANGMUIR **22**, 6485 (2006).
161. K. B. Jinesh and J. W. M. Frenken: *Capillary condensation in atomic scale friction: How water acts like a glue*. PHYSICAL REVIEW LETTERS **96**, (2006).
162. V. B. Engelkes and C. D. Frisbie: *Simultaneous nanoindentation and electron tunneling through alkanethiol self-assembled monolayers*. J. PHYS. CHEM. B **110**, 10011 (2006).
163. K. L. Johnson, K. Kendall, and A. D. Roberts: *Surface Energy and Contact of Elastic Solids*. PROCEEDINGS OF THE ROYAL SOCIETY OF LONDON SERIES A-MATHEMATICAL AND PHYSICAL SCIENCES **324**, 301-& (1971).
164. T. Ederth: *Computation of Lifshitz-van der Waals forces between alkylthiol monolayers on gold films*. LANGMUIR **17**, 3329 (2001).
165. R. R. Dagastine, D. C. Prieve, and L. R. White: *Calculations of van der Waals forces in 2-dimensionally anisotropic materials and its application to carbon black*. JOURNAL OF COLLOID AND INTERFACE SCIENCE **249**, 78 (2002).
166. M. Bordag, B. Geyer, G. L. Klimchitskaya, and V. M. Mostepanenko: *Lifshitz-type formulas for graphene and single-wall carbon nanotubes: van der Waals and Casimir interactions*. PHYSICAL REVIEW B **74**, (2006).
167. R. F. Rajter, R. H. French, W. Y. Ching, W. C. Carter, and Y. M. Chiang: *Calculating van der Waals-London dispersion spectra and Hamaker coefficients of carbon nanotubes in water from ab initio optical properties*. JOURNAL OF APPLIED PHYSICS **101**, (2007).
168. C. Argento and R. H. French: *Parametric tip model and force-distance relation for Hamaker constant determination from atomic force microscopy*. JOURNAL OF APPLIED PHYSICS **80**, 6081 (1996).
169. J. N. Israelachvili and R. M. Pashley: *Measurement of the Hydrophobic Interaction Between 2 Hydrophobic Surfaces in Aqueous-Electrolyte Solutions*. JOURNAL OF COLLOID AND INTERFACE SCIENCE **98**, 500 (1984).
170. I. Nnebe and J. W. Schneider: *Characterization of distance-dependent damping in tapping-mode atomic force microscopy force measurements in liquid*. LANGMUIR **20**, 3195 (2004).

171. E. E. Meyer, Q. Lin, T. Hassenkam, E. Oroudjev, and J. N. Israelachvili: *Origin of the long-range attraction between surfactant-coated surfaces*. PROCEEDINGS OF THE NATIONAL ACADEMY OF SCIENCES OF THE UNITED STATES OF AMERICA **102**, 6839 (2005).
172. A. M. Dokter, S. Woutersen, and H. J. Bakker: *Anomalous slowing down of the vibrational relaxation of liquid water upon nanoscale confinement*. PHYSICAL REVIEW LETTERS **94**, (2005).

Samenvatting voor de leek

De processen die zich afspelen binnen levende cellen – en dus ook in ons eigen lichaam – kunnen op veel manieren bekeken worden. Een bioloog ziet membranen en eiwitten die bepaalde functies uitvoeren. Een chemicus ziet stoffen die met elkaar reageren. Wij fysici zien moleculen die krachten op elkaar uitoefenen. Hoe je er ook naar kijkt, in de meeste van deze processen speelt water, waar cellen voor het grootste gedeelte uit bestaan, een belangrijke rol.

Behalve vanuit verschillende gezichtspunten, kunnen cellen ook met veel verschillende technieken worden bekeken. De lichtmicroscop en electronenmicroscop worden al sinds jaar en dag gebruikt om naar levensprocessen te kijken. Een relatief jong type microscoop is de *Atomic Force Microscope* of AFM. Deze microscoop, in het Nederlands ook wel tastmicroscop genoemd, werkt op basis van mechanische principes. Door met het puntje van een extreem scherpe naald een oppervlak af te tasten, kan een beeld worden gevormd met een resolutie die veel hoger is dan die van de traditionele lichtmicroscop. De naald zit gemonteerd op een *cantilever* (eigenlijk een bladveer, maar meestal vertaald als hefboom). Door de verbuiging van deze veer te meten wordt bepaald hoe groot de kracht op de *tip* (het puntje van de naald) is. Een tastmicroscop kan niet alleen afbeeldingen maken, maar ook krachten direct meten binnen een zeer gelokaliseerd gebied op een oppervlak. Dit kan zelfs als dit oppervlak zich in water bevindt. Daarom is deze microscoop bij uitstek geschikt om de mechanica die aan levensprocessen ten grondslag ligt te bestuderen. Dat deze uitsluitend aan oppervlakken kan worden gedaan is een beperking die we hierbij voor lief nemen.

Dit proefschrift beschrijft een aantal uitbreidingen en verbeteringen op het gebied van de AFM. Deze worden vervolgens toegepast in een hoge resolutie meting van hydrofobe krachten.

Hoofdstuk 2 beschrijft kwantitatief de fundamentele limieten voor het meten van krachten met een AFM in een vloeistof. Behalve door de krachten op de tip, beweegt de cantilever ook altijd een beetje uit zichzelf. Deze *thermische ruis* is inherent gekoppeld aan wrijvingsprocessen. Daardoor is deze vorm van ruis ook ernstiger als de cantilever in vloeistof is. Door de afmetingen van de cantilever zo klein mogelijk te maken, kan deze fundamentele vorm van ruis geminimaliseerd worden. Door ook de stijfheid van de bladveer op de juiste manier af te stemmen op die van het te onderzoeken object, wordt de signaal-ruis verhouding geoptimaliseerd. Een ander groot voordeel van kleine cantilevers is dat ze veel sneller reageren op een aangebrachte kracht en dus gebruikt kunnen worden om sneller te meten.

Om krachtmetingen te kunnen doen met optimale signaal-ruis verhouding is een instrument nodig dat kan werken met extreem kleine cantilevers en bovendien geen ruis toevoegt aan de fundamentele ruis. Momenteel verkrijgbare cantilevers zijn veel groter dan strikt noodzakelijk. In *hoofdstuk 3* wordt dan ook beschreven hoe wij cantilevers hebben gemaakt die een factor 10 kleiner zijn dan bestaande types. Dit hebben wij gedaan door bestaande cantilevers kleiner te snijden met behulp van een gefocuseerde ionenbundel, en ook door ze met lithografietechniek uit membranen te maken. Verder wordt in dit hoofdstuk afgeleid hoe goed de gevoeligheid kan zijn van een veelgebruikte methode om de verbuiging van een cantilever te meten. Door een systeem te bouwen dat deze methode implementeert met zorgvuldig gekozen componenten, kan zelfs de zeer geringe thermische beweging van miniatuurcantilevers nog worden gedetecteerd.

Hoofdstuk 4 beschrijft het ontwerp en de implementatie van een aantal andere onderdelen die nodig zijn om metingen te kunnen doen met de miniatuurcantilevers. De scanner is licht en compact en zou hierdoor geschikt moeten zijn voor hoge-snelheidsmetingen. Tiphouder en scanner zijn zodanig geconstrueerd dat er bij metingen in vloeistof zo min mogelijk vervuiling optreedt. In dit hoofdstuk worden verder een paar elektronische componenten beschreven die we hebben ontwikkeld om met hoge snelheid te meten en om plaatsopgelost krachten te meten.

In *hoofdstuk 5* wordt een heel ander soort gereedschap voor AFM metingen beschreven. In sommige gevallen, bijvoorbeeld als men dissipatieve krachten (wrijvings- of dempingskrachten) wil meten, is het nodig of gunstig om bij het uitvoeren van een krachtmeting de cantilever te laten trillen. Dit noemt men wel een dynamische meting. Uit praktische overwegingen is het vaak te verkiezen om het aandrijven van de trilling te doen met een constante amplitude en frequentie. Een probleem van deze aandrijfmethode was tot nu toe dat het niet mogelijk was om kwantitatief de krachten te berekenen uit een amplitude- en fasemeting. In dit proefschrift laten wij zien dat via een relatief eenvoudige omrekenmethode gebruik te maken is van een methode voor krachtterugrekening die is ontwikkeld voor een ander type aandrijving. Alhoewel niet wiskundig te berekenen is hoe goed deze methode de werkelijk ondervonden krachten benadert, blijkt uit simulaties dat de afwijkingen zeer gering zijn.

In *hoofdstuk 6* onderzoeken wij vervolgens de grenzen van de praktische bruikbaarheid van de in hoofdstuk 5 ontwikkelde methode. Deze is namelijk gebaseerd op de aanname dat de krachten die op de tip werken slechts een verwaarloosbare verstoring van de cantileverbeweging tot gevolg hebben. Door zo realistisch mogelijk een groot aantal experimenten te simuleren met een computerprogramma laten wij zien dat ook bij een aantal krachtprofielen die niet aan de basisaanname voldoen een correcte terugrekening valt te doen. De manier waarop de amplitude van de cantileverbeweging wordt gemeten is hierbij van invloed. Met de simulaties is ook de invloed van de krachtterugrekening op de doorwerking van (thermische) ruis in de metingen

te onderzoeken. Hieruit blijkt dat het voor de ruis in de berekende kracht gunstig is als in het experiment een kleine amplitude wordt gebruikt. De ruis in de berekende demping is nog sterker afhankelijk van de amplitude. Uit de simulaties blijkt eens te meer dat met miniatuurcantilevers aanzienlijk minder ruis in de metingen optreedt, met name bij het meten van demping.

Hoofdstuk 7 tenslotte brengt alle hierboven genoemde onderwerpen bij elkaar. Hierin wordt een meting beschreven van de afstandsafhankelijkheid van hydrofobe (watermijdende) krachten tussen twee nanoscopisch kleine oppervlakken. Hydrofobe krachten zijn de (over het algemeen aantrekkende) krachten die onder water aanwezig zijn tussen twee oppervlakken of deeltjes die moeilijk met water mengen. Een bekend voorbeeld hiervan is de kracht die maakt dat vet tot druppels samenklontert aan het oppervlak van een kop soep. Ontelbare eiwitten en membranen in ons lichaam blijven intact omdat ze bij elkaar gehouden worden door hydrofobe krachten. Er is dan ook geen twijfel aan het bestaan van deze krachten. Hoe ze precies worden veroorzaakt is tot op heden echter nog een groot raadsel. Ondanks tientallen jaren van studie aan hydrofobe effecten kunnen hedendaagse theoretische modellen niet voorspellen wat de afstandsafhankelijkheid van de hydrofobe kracht zou moeten zijn. Ook wat betreft experimentele resultaten is er op dit gebied weinig consensus. Veel resultaten leken in eerste instantie spectaculair, maar bleken bij nader inzien te berusten op artefacten.

Wat er tot nu toe experimenteel bekend is over de hydrofobe kracht berust op metingen aan oppervlakken die over een gebied van micrometers of zelfs millimeters hydrofoob zijn. In ons lichaam zijn de hydrofobe oppervlakken vaak maar één of enkele moleculen groot, en bevinden ze zich dicht bij hydrofiele (waterminnende) oppervlakken. Dit is naar alle waarschijnlijkheid van invloed op de hydrofobe kracht.

Om een eerste stap te zetten in de richting van de complexe situatie die in de natuur te vinden is, hebben wij een oppervlak geconstrueerd dat bestaat uit nanoscopische domeintjes (10-30 nm groot) van hydrofiele en hydrofobe moleculen. De tip van de AFM hebben wij voorzien van een miniscuul hydrofoob oppervlak door er een koolstof nanobuis op te monteren. Met deze tip hebben wij het oppervlak afgetast door steeds boven één plek omlaag en omhoog te gaan en daarna weer een stukje op te schuiven. Uit de metingen van amplitude en fase kon dan de kracht berekend worden boven dit punt als functie van de afstand tot het oppervlak. Bij afstanden groter dan 2 nanometer is de aantrekkende kracht erg vergelijkbaar met krachten die zijn gemeten op grote oppervlakken. Onder de 2 nm, een gebied dat voor eerdere metingen niet bereikbaar was, zien wij echter een overgang naar afstotende krachten, een zeer verrassende bevinding! De metingen in dit proefschrift lichten slechts een klein tipje op van de sluier van de krachten die de gang van zaken in de complexe situaties in onze cellen bepalen. Maar door af te stappen van geïdealiseerde omstandigheden en te kijken op een schaal die meer overeenkomt met relevante situaties geven ze wel de richting aan waarin het onderzoek naar hydrofobe krachten zich moet begeven.

List of publications

- 1 M. J. Rost, L. Crama, P. Schakel, E. van Tol, G. B. E. M. van Velzen-Williams, C. F. Overgaw, H. ter Horst, H. Dekker, B. Okhuijsen, M. Seynen, A. Vijftigschild, P. Han, A. J. Katan, K. Schoots, R. Schumm, W. van Loo, T. H. Oosterkamp, and J. W. M. Frenken: *Scanning probe microscopes go video rate and beyond*. REVIEW OF SCIENTIFIC INSTRUMENTS **76**, (2005).
- 2 A. J. Katan, and T. H. Oosterkamp: *Measuring hydrophobic interactions with three-dimensional nanometer resolution*, submitted to JOURNAL OF PHYSICAL CHEMISTRY C.

Curriculum vitae

Allard Jules Katan is geboren in Rhenen op 18 augustus 1977. In 1995 ontving hij zijn gymnasium-diploma van het Marnix College te Ede. Hierna begon hij aan de studie Technische Natuurkunde aan de Technische Universiteit te Delft. In november 2000 begon hij aan zijn afstudeerwerk in de vakgroep Quantum Transport onder supervisie van Prof. Dr. J.E. Mooij. Tijdens dit werk leerde hij cleanroom fabricagetechnieken, quantum computation met supergeleidende systemen en het uitvoeren van metingen bij extreem lage temperaturen. In mei 2002 studeerde hij af met een scriptie getiteld “Switching behavior of dc-SQUIDs with frequency-dependent damping: measurement tools for the Josephson persistent current qubit”. In oktober 2002 begon hij als OIO aan zijn promotieonderzoek in de vakgroep Interface Physics van het Kamerlingh Onnes Laboratorium aan de Universiteit van Leiden, die geleid wordt door Prof. Dr. J.W.M. Frenken. Het onderzoek dat hij hier deed werd gedaan onder directe begeleiding van dr. ir. T.H. Oosterkamp en staat beschreven in dit proefschrift. Tot april 2007 was hij in dienst van de stichting FOM. Sindsdien werkt hij binnen het kader van Nanoned aan de Universiteit Leiden aan het realiseren van een hoge-snelheids AFM.

Acknowledgements

Although this thesis bears only my name, its contents are the result of a joint effort of many. When I first came into the lab to build an AFM I hadn't actually touched one before. Amalia Stamouli, Henriette Jensenius and especially Dionne Klein showed me the ropes. None of the work in chapters 3 and 4, and 7 could have been done without the excellent technical support of the FMD and ELD. Especially Dian van der Zalm and Raymond Koehler have contributed largely to the design and implementation of our AFM from day one. In the continuing struggle to shape the CAMERA electronics and software into a usable tool for AFM I had a lot of help from Els van Tol, Peter Schakel, Bert Crama, Martin Moene, Gert-Jan van Baarle and Marcel Rost. The procedure for Focused Ion Beam modification of cantilevers described in paragraph 3.1.1 was developed in a collaboration with Paul Alkemade of the HREM group at the T.U. Delft. Marcel Hesselberth and Werner van Loo made important contributions to the FIB modified cantilevers as well. Before the arrival of the Leiden NanoSem manipulator in 2006 I could never have made nanotube tips on these levers if Prof. Suzi Jarvis at Trinity College, Dublin would not have allowed me the use of her lab's facilities. Khashayar Babeigavan of the Molecular Electronics and Devices group at the T.U. Delft did most of the work for the fabrication of the lithographically defined cantilevers described in 3.1.2. Undergraduate student Reinier Schumm was a great help in the early stages of the slow evolutionary process of the development of scanners. The DNA sample shown in figure 4.6 was one of a set that was made with the help of John van Noort and Martijn de Jager. The work in chapter 5 was greatly stimulated through a discussion with professors Suzi Jarvis and John Sader. An email discussion with Paul Ashby put me back on the right track regarding the translation of amplitude and phase to damping coefficient. Maarten van Es wrote the simulation that produced the data for all the figures of chapters 5 and 6 and helped shaping the ideas about what they meant in many discussions. Frankie Wirtz, Dirk Heering and Razvan Stan helped me with the electrochemistry for chapter 7 and were of great aid during my frantic search for the source of the blobs on my SAMs. Lastly, I think this book is the one of the best typeset theses I have ever seen. This is not my merit, but that of Bart de Vries, who gave me a crash-course in typography and lay-out while helping me to transfer this document from Word to InDesign.

